

This electronic thesis or dissertation has been downloaded from the King's Research Portal at <https://kclpure.kcl.ac.uk/portal/>



Development of Novel Algorithms for Microwave Medical Imaging Applications

Lu, Pan

Awarding institution:
King's College London

The copyright of this thesis rests with the author and no quotation from it or information derived from it may be published without proper acknowledgement.

END USER LICENCE AGREEMENT



Unless another licence is stated on the immediately following page this work is licensed

under a Creative Commons Attribution-NonCommercial-NoDerivatives 4.0 International

licence. <https://creativecommons.org/licenses/by-nc-nd/4.0/>

You are free to copy, distribute and transmit the work

Under the following conditions:

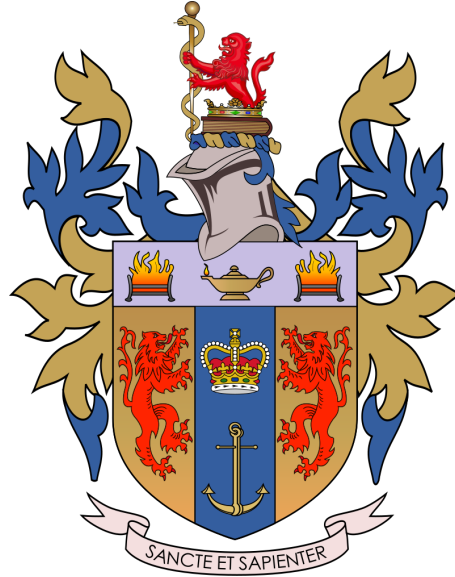
- Attribution: You must attribute the work in the manner specified by the author (but not in any way that suggests that they endorse you or your use of the work).
- Non Commercial: You may not use this work for commercial purposes.
- No Derivative Works - You may not alter, transform, or build upon this work.

Any of these conditions can be waived if you receive permission from the author. Your fair dealings and other rights are in no way affected by the above.

Take down policy

If you believe that this document breaches copyright please contact librarypure@kcl.ac.uk providing details, and we will remove access to the work immediately and investigate your claim.

Development of Novel Algorithms for Microwave Medical Imaging Applications



Pan Lu

First Supervisor: Dr Panagiotis Kosmas

Second Supervisor: Prof Zoran Cvetkovic

This dissertation is submitted for the degree of

Doctor of Philosophy

King's College London

January 31, 2023

Acknowledgements

First and foremost, I would like to show my deepest gratitude to my supervisor, Dr Panagiotis Kosmas, for his continuous support and invaluable advice during every period of my PhD study. Without his help, I would never have accomplished these research works and completed my study. Thanks for his encouragement, motivation, and knowledge to guide me in this PhD and my future life.

I would like to give special thanks to Prof Juan Córcoles for discussions about work and his support that helped me to understand electromagnetic simulations in the course of my studies, especially at the early stage.

I also owe great thanks to our group members, Syed Ahsan, Wei Guo, Ziwen Guo, Olympia Karadima, and Eleonora Razzicchia, for their endless support of CST simulations and experiments, as well as their discussion and feedback on the algorithm development.

I am also grateful to the Department of Engineering for the opportunity to do research and for the facilities provided. I would also like to thank Prof Zoran Cvetkovic for the opportunity to become a TA. I would also express my gratitude to my colleagues and friends from NMS, including Zhenghao, Haodi, Ming, Huiping, Shichao and Ranyin. Thanks for their support and accompaniment during this unforgettable time of my life.

Last but not least, I want to give my most thanks to my parents for their endless support and encouragement in my life.

Abstract

Non-ionising microwave (MW) is used in microwave imaging (MWI) to recover the information of the investigated tissues, such as the breast and head, for medical applications. Unlike radar-based MWI, microwave tomography (MWT) aims to reconstruct the dielectric properties by solving an electromagnetic (EM) inverse scattering problem (ISP) with measurement data obtained by an antenna array that transmits and receives MW signals. This requires a robust and efficient algorithm, as the inverse problem is ill-posed and highly nonlinear.

In this thesis, a novel distorted Born iterative method (DBIM) algorithm is proposed and applied to different scenarios, mainly for head imaging cases with the finite element method (FEM) and finite difference time domain (FDTD) method used as forward solvers to simulate wave propagation. The fast iterative shrinkage/thresholding algorithm (FISTA) is used as an inverse solver to solve the resulting linear systems. A novel two-dimensional (2-D) FEM-based forward solver that provides great efficiency is developed for DBIM, which utilises the FEM matrix to build the DBIM matrix without the need for interpolation. The 2-D FDTD-based DBIM approach has been extended to three-dimensional (3-D) versions, and an in-house 3-D FDTD forward solver is implemented with graphics processing unit (GPU) acceleration for the DBIM. With the help of the compute unified device architecture (CUDA) toolkit and MEX functions in Matlab, the 3-D implementation can use the high performance of GPU and Matlab's capacity for matrix computation directly without any interface problem.

The proposed FEM-based and FDTD-based DBIM approaches are com-

combined with FISTA to obtain better reconstruction performance. The advanced inverse solver FISTA uses a shrinkage operator and accelerated Nesterov momentum to solve ill-posed linear systems with improved robustness and efficiency, which has a better performance compared to traditional inverse solvers such as gradient descent (GD) type methods.

Two efficient tools are proposed to improve the DBIM reconstruction results. The first tool is a preprocessing technique that employs the time gating technique to denoise the experimental signals, which can improve the signal quality and thus improve reconstruction results. The second tool is a postprocessing technique using k-means to cluster and classify the obtained reconstruction values, helping to better distinguish targets from the background.

These proposed algorithms are validated with numerical data and experimental data of different scenarios, including basic cylindrical models and complex models such as head models. A preliminary study of the reconstruction possibility of head imaging by the proposed FDTD-based DBIM-FISTA approach is presented, including an anatomically complex head phantom, the Zubal head phantom.

The Zubal head phantom is a 3-D magnetic resonance imaging (MRI)-derived voxel-based anthropomorphic phantom of human males from Yale University, which is suitable for testing and evaluating computer-based modelling and simulation calculations. In this thesis, it is converted to a simplified multi-layer phantom and used in different imaging scenarios to investigate MWT head/brain imaging with limited information and offset antenna rings.

Contents

	Page
1 Introduction	1
1.1 Motivation, aim, and objectives	1
1.2 Background	2
1.3 Overview of microwave imaging	4
1.3.1 Radar-based imaging	4
1.3.2 Microwave tomography	5
1.4 Contributions	6
1.5 Overview of the thesis	10
2 Fundamentals and Related Work	11
2.1 Overview of background methods	11
2.2 Electromagnetic wave propagation	14
2.2.1 Maxwell's equations	14
2.2.2 Finite difference time domain method	17
2.2.2.1 Discretisation scheme of Maxwell's equations	17
2.2.2.2 Convolutional perfectly matched layer	22
2.2.2.3 Debye model for dispersive materials	24
2.2.3 Finite element method	25
2.3 Basics of the inverse scattering problem theory	29
2.3.1 Direct (forward) scattering problems	29
2.3.2 Formulation of inverse scattering problem	30
2.3.3 Linear sampling method	33

2.3.4	Distorted Born iterative method	34
2.4	Optimisation theory	35
2.5	Inverse solvers for linear systems	36
2.5.1	Tikhonov regularisation	37
2.5.2	Conjugate gradient for least squares	38
2.5.3	Iterative shrinkage/thresholding methods	38
2.6	Conclusion	40
3	Methodology for Developing and Testing the DBIM-FISTA MWI Algorithm	41
3.1	Methodology	41
3.1.1	Green's function with the DBIM algorithm	41
3.1.2	FEM-DBIM approach	47
3.1.3	FDTD-DBIM approach	50
3.1.4	Fast iterative shrinkage/thresholding algorithm	52
3.1.5	Data calibration	53
3.1.6	Multiple frequency approach	54
3.2	Analysis of the DBIM-FISTA algorithm	55
3.3	Numerical and experimental models	57
3.3.1	Cylindrical models	58
3.3.2	SAM model	59
3.3.3	Zubal head phantom	60
3.3.4	Experimental system and brain phantom	62
3.4	Error definition	65
3.5	Conclusion	66
4	Reconstruction with the 2-D FEM-based and FDTD-based DBIM	67

4.1	Assessment of the 2-D reconstruction images	67
4.2	Validation with the FEM-based DBIM	68
4.3	Impact of the forward solver	73
4.4	Impact of the inverse solver	78
4.4.1	Inverse solver for FEM-based DBIM	78
4.4.2	Inverse solver for FDTD-based DBIM	80
4.4.2.1	Comparison of CGLS and FISTA	80
4.4.2.2	Comparison of TwIST and FISTA	80
4.5	Reconstruction with the 2D FDTD-DBIM-FISTA	85
4.5.1	CST data reconstructions	85
4.5.1.1	Cylindrical models	85
4.5.1.2	SAM model	86
4.5.2	Zubal model	86
4.5.2.1	Reconstruction with FDTD data	88
4.5.2.2	Reconstruction with CST data	92
4.5.3	Experimental data reconstructions	93
4.5.3.1	Cylindrical models	93
4.5.3.2	Experimental brain phantom	94
4.6	Conclusion	97

5 **Three-dimensional Microwave Head Imaging Analysis Using GPU Accelerated FDTD** 98

5.1	Introduction of 3-D head imaging	98
5.2	Implementation of the 3-D FDTD-DBIM-FISTA algorithm using GPU . .	101
5.2.1	3-D FDTD on GPU with CUDA	101
5.2.2	3-D DBIM-FISTA using GPU based on MATLAB	104

5.3	Assessment of the 3-D reconstruction images	106
5.4	CST data reconstruction with the Zubal head phantom	107
5.4.1	Scenarios and reconstructions with the FDTD-DBIM-FISTA . . .	107
5.4.1.1	Case I where only target is unknown	107
5.4.1.2	Case II where limited information is known	112
5.4.1.3	Case III where a headband is used with a small target placed at an offset height	115
5.5	Experimental data reconstruction	121
5.6	Conclusion	123
6	Tools to Improve the DBIM Approach	124
6.1	Time gating for experimental data	124
6.2	Target classification with MWI algorithms	129
6.3	Conclusion	133
7	Conclusions and Future Work	134
7.1	Conclusions	134
7.2	Future work	137

Abbreviations

2-D two-dimensional

3-D three-dimensional

ABC absorbing boundary condition

BIM Born iterative method

CEM computational electromagnetic

CGLS conjugate gradient method for least squares

CPML convolutional perfectly matched layer

CPU central processing unit

CSF cerebrospinal fluid

CSI contrast source inversion

CT computed tomography

CUDA compute unified device architecture

d.o.f degrees of freedom

DBIM distorted Born iterative method

DDA discrete dipole approximation

EM electromagnetic

FDTD finite difference time domain

FEM finite element method

FFT fast Fourier transform

FISTA fast iterative shrinkage/thresholding algorithm

FIT finite integration technique

FPGA field-programmable gate array

FT Fourier transform

GD gradient descent

GN Gauss-Newton

GPU graphics processing unit

IFT inverse Fourier transform

ISP inverse scattering problem

ISTA iterative shrinkage thresholding algorithm

LHS left-hand side

LSM linear sampling method

LSQR least squares with QR-factorisation

ML machine learning

MoM method of moments

MRI magnetic resonance imaging

MW microwave

MWI microwave imaging

MWT microwave tomography

NT no target

PDE partial differential equation

PET positron emission tomography

PML perfectly matched layer

RF radio frequency

RHS right-hand side

RMSE root mean square error

RRE relative residual error

SAM specific anthropomorphic mannequin

SMs streaming multiprocessors

TE transverse electric

TEM transverse electromagnetic

TM transverse magnetic

TR transmitter-receiver

TSVD truncated singular value decomposition

TwIST two-step iterative shrinkage thresholding

UPML uniaxial perfectly matched layer

UWB ultra-wideband

UWCEM University of Wisconsin Cross-Disciplinary Electromagnetics Laboratory

VIE volume integral equation

VNA virtual network analyzer

WT with target

List of Figures

2.1	EM wave propagation.	14
2.2	Scheme of Yee's lattice. (source: https://meep.readthedocs.io/en/latest/Yee_Lattice/)	18
2.3	Mesh of the finite element method with triangular elements.	27
2.4	Example of inverse scattering scenario.	32
3.1	Perspective and top views of the CST models: (a) perspective view, (b) top view.	59
3.2	CST head model: (a) schematic of the head model, (b) top view of the head model.	60
3.3	Views of the Zubal phantom in CST: (a) 3-D side-view, (b) cross-sectional top-down view, (c) 3-D view with blood target, (d) cross-sectional slice used in 2-D experiments (93th slice of the original model, where the centre of the target is placed).	61
3.4	Photos of the experimental system.	63
3.5	Photos of (a) brain phantom, (b) phantom with target inserted, and (c) phantom placed inside the experimental tank.	64
3.6	Process of making the brain phantom.	65
3.7	The monopole antenna used in the experimental system.	65

4.1	Single-target ($\epsilon_{tg} = 1.6 - 0.5j$) reconstruction with 15 DBIM iterations at 1.0 GHz: (a) real part of ϵ_r , (b) imaginary part of ϵ_r (FEM Model 1). Two-target reconstruction with 15 DBIM iterations at 1.0 GHz: (c) real part of ϵ_r , (d) imaginary part of ϵ_r (FEM Model 2).	70
4.2	Two high-permittivity targets ($\epsilon_{tg} = 25 - 15.5j$) reconstruction with 15 DBIM iterations at 1.0 GHz. Position 1: (a) real part of ϵ_r , (b) imaginary part of ϵ_r (FEM Model 3.1). Position 2: (c) real part of ϵ_r , (d) imaginary part of ϵ_r (FEM Model 4.1).	71
4.3	Ratio of the calculated electric field between FDTD and FEM for the TR pairs.	75
4.4	Normalised ratio of the calculated electric field between FDTD and FEM for the TR pairs.	75
4.5	Experimental data reconstruction of single cylindrical target ($\epsilon_{tg} \approx 78 - 3j$) with 15 DBIM iterations at 0.9 GHz by FEM-based DBIM (a) real part, (c) imaginary part, and FDTD-based DBIM (b) real part (d) imaginary part.	76
4.6	Experimental data reconstruction of two cylindrical targets ($\epsilon_{tg} \approx 78 - 3j$) with 15 DBIM iterations at 0.9 GHz by FEM-based DBIM (a) real part, (c) imaginary part, and FDTD-based DBIM (b) real part (d) imaginary part.	77
4.7	Reconstructed real part of ϵ_r of the Fresnel dataset with 15 DBIM iterations at 1.0 GHz of cylindrical targets ($\epsilon_{tg} \approx 3$). One-target case: (a) CGLS, (c) FISTA. Two-target case: (b) CGLS, (d) FISTA.	79

4.8	Reconstruction results of two weak scatterers using CGLS and FISTA after 5 DBIM iterations: (a) ϵ_∞ of the original image, (b) relative residual error RRE and relative error of permittivity e_ϵ of CGLS and FISTA, (c) reconstruction by CGLS, (d) reconstruction by FISTA.	81
4.9	Ground truth and initial guess of the breast model.	82
4.10	Relative error of epsilon infinity e_{ϵ_∞} : (a) 1.5 GHz, (b) 2.0 GHz, and relative residual error RRE: (c) by TwIST and FISTA, with single-frequency approach after 60 DBIM iterations.	82
4.11	(a)(c) Reconstruction values of ϵ_∞ by TwIST at 1.5 and 2.0 GHz, respectively. (b)(d) Reconstruction values of ϵ_∞ by FISTA at 1.5 and 2.0 GHz, respectively.	83
4.12	Relative errors of the breast model by TwIST and FISTA with frequency hopping approach after 60 DBIM iterations: (a) relative error of epsilon infinity e_{ϵ_∞} of TwIST and FISTA, (b) relative residual error RRE.	84
4.13	Reconstructions of the breast model by TwIST and FISTA after 60 DBIM iterations with frequency hopping approach: (a) reconstruction by FISTA, (b) reconstruction by TwIST.	84
4.14	Reconstruction images of (a) real part of permittivity, (b) imaginary part of permittivity.	85
4.15	Reconstruction images of real part of permittivity (left) and imaginary part of permittivity (right) of the SAM head model: (a)(b) reconstruction at 0.8 GHz with the single frequency approach, (c)(d) reconstruction with the frequency hopping approach.	87

4.16	Reconstruction results of ϵ_{∞} of the full head plus the blood target at 1.0 GHz: (a) ground truth, (b) initial guess, (c) reconstruction, (d) reconstruction contrast of ϵ_{∞}	88
4.17	Reconstruction results of ϵ_{∞} of the head without grey matter at 0.8 GHz: (a) ground truth, (b) initial guess, (c) reconstruction, (d) reconstruction with changed colour bar.	89
4.18	Reconstruction results of ϵ_{∞} of the three-layer head at 1 GHz: (a) ground truth, (b) initial guess, (c) reconstruction, (d) reconstruction with changed colour bar.	90
4.19	Reconstruction results of ϵ_{∞} of the three-layer head at 0.8 GHz: (a) reconstruction, (b) reconstruction with changed colour bar.	91
4.20	Reconstruction results of real part of permittivity of the Zubal head phantom at 1.0 GHz when the grey matter is removed: (a) initial guess, (b) reconstruction when CSF is not included in WT, (c) reconstruction when CSF is included in WT).	92
4.21	Reconstruction images of real part of ϵ_r of the cylindrical targets using multiple-frequency approach: (a) single target, (b) two targets.	93
4.22	Reconstruction images of real part of ϵ_r of the cylindrical targets using multiple-frequency approach: (a) single target, (b) two targets.	94
4.23	Brain phantom inside tank with antenna ring in the middle.	95
4.24	Reconstruction images of real part of ϵ_r of the experimental brain phantom: (a) EXP-b, (b) EXP-bII.	95
4.25	Reconstruction images of real part of ϵ_r of the experimental brain phantom with modified initial guess: (a) original, (b) with constraints.	96

5.1	CPU and GPU structure. (source: https://docs.nvidia.com/cuda/cuda-c-programming-guide/index.html)	101
5.2	CUDA program configuration. (source: https://docs.nvidia.com/cuda/cuda-c-programming-guide/index.html)	102
5.3	Flowchart of the FDTD process.	104
5.4	Dielectric constant distribution $\Re(\epsilon_r)$ for Case I. Top: (a) y–z slice, (b)x–z slice, and (c) x–y slice for the numerical head model. Bottom: (d) y–z slice, (e) x–z slice, and (f) x–y slice for the experimental phantom.	107
5.5	3-D reconstructions with simplified Green’s functions for Case I of Fig. 3.3 at 1.0 GHz: (a), (b),(c) relative permittivity $\Re(\epsilon_r)$, and (d),(e), (f) contrast for the y-z, x-z, and x-y slices, respectively. A cylindrical eight-antenna array centred at the target height is used to produce the data.	108
5.6	3-D reconstructions, same as Fig. 5.5 but with vectorial Green’s function in (3.17), for Case I of Fig. 3.3 at 1.0 GHz. (a), (b), (c) Relative permittivity $\Re(\epsilon_r)$ for the y-z, x-z, and x-y slices, respectively.	109
5.7	2-D reconstructions of: (a) relative permittivity $\Re(\epsilon_r)$ and, (b) contrast for Case I of Fig. 3.3 at 1.0 GHz.	109
5.8	Reconstructions of Case I when RRE converges: 2-D with 200 iterations and 3-D with 120 iterations: (a), (b) residual error plot for 2-D and 3-D respectively, (c) contrast for 2-D reconstruction, (d), (e), (f) contrast for the y-z, x-z, and x-y slices of 3-D reconstruction respectively.	110
5.9	Reconstructions of Case I when the antenna position has a 5 degrees difference along the z–plane between the NT case and WT case. Contrast for the y–z, x–z, and x–y slices of 3-D reconstruction, respectively.	111

5.10	Cross-sectional view for Case II.1 and Case II.2: (a) NT model for both cases; (b) WT1 model for Case II.1 with grey matter and CSF replaced by white matter; (c) WT2 model for Case II.2 with only grey matter replaced by white matter.	112
5.11	True values of $\Re(\epsilon_r)$ of Case II.1 and II. 2 at 1.0 GHz: (a) y-z slice, (b) x-z slice, (c) x-y slice of Case II. 1. (d) y-z slice, (e) x-z slice, (f) x-y slice of Case II. 2.	113
5.12	3-D reconstructions of $\Re(\epsilon_r)$ at 1.0 GHz: (a) y-z slice, (b) x-z slice, and (c) x-y slice for Case II.1; (d) y-z slice, (e) x-z slice, and (f) x-y slice for Case II.2.	114
5.13	2-D reconstructions of $\Re(\epsilon_r)$ at 1.0 GHz: (a) Case II.1, and (b) Case II.2. A cylindrical eight-antenna array centred at the target height is used to produce the data.	114
5.14	(a) Top and (b), (c) side views of the setup used in Section 3.2. A headband is placed at the top of the head phantom, and sixteen antennas are placed in a two ring array inside the headband, with 8 antennas for each ring.	115
5.15	True values of $\Re(\epsilon_r)$ of Case III at 1.0 GHz: (a) y-z slice, (b) x-z slice, and (c) x-y slice.	116
5.16	3-D(a)(b)(c) and 2-D (d)(e)(f) reconstructions of Case III.1 at 1.0 GHz: (a) y-z slice, (b) x-z slice, and (c) x-y slice of 3-D reconstructions. 2-D slice reconstructions (d) bottom ring, (e) top ring, and (f)both rings. The headband of Fig. 5.14 is used to obtain the data.	117

5.17	3-D reconstructions of $\Re(\epsilon_r)$ for Case III.2 at 1.0 GHz: (a) y-z slice, (b) x-z slice, and (c) x-y slice. The headband of Fig. 5.14 (with the addition of absorbing material) is used to obtain the data.	118
5.18	2-D Reconstructions of $\Re(\epsilon_r)$ of Case III.2 for the x-y slice at 1.0 GHz using data from the: (a) bottom ring, (b) top ring, and (c) both rings. The headband of Fig. 5.14 (with the addition of absorbing material) is used to obtain the data.	118
5.19	3-D reconstructions of $\Re(\epsilon_r)$ for Case III.3 at 1.0 GHz: (a) y-z slice, (b) x-z slice, and (c) x-y slice. The headband of Fig. 5.14 (with an increased distance between the array and the interface with air) is used to obtain the data.	119
5.20	2-D Reconstructions of $\Re(\epsilon_r)$ of Case III.3 for the x-y slice at 1.0 GHz using data from the: (a) bottom ring, (b) top ring, and (c) both rings. The headband of Fig. 5.14 (with an increased distance between the array and the interface with air) is used to obtain the data.	119
5.21	3-D reconstructions of $\Re(\epsilon_r)$ for Case III.2 at 1.0 GHz: (a) y-z slice, (b) x-z slice, and (c) x-y slice, same as Fig.5.17 but with vectorial Green's functions in (3.17).	120
5.22	Dielectric constant distribution $\Re(\epsilon_r)$ for the validation models. (a) y-z slice, (b) x-z slice, and (c) x-y slice for the experimental phantom. . . .	121
5.23	Reconstructions of $\Re(\epsilon_r)$ for the experimental data at 1.0 GHz in 3-D: (a) y-z slice, (b) x-z slice, and (c) x-y slice, and in 2-D (d).	122
6.1	Magnitude in dB of the S-parameter in (a) time domain and (b) frequency domain.	126

6.2	Reconstructions of real permittivity of one target by 20 DBIM iterations. First and third rows (a) – (c) and (g) – (i): reconstructed by FISTA with original data. Second and fourth rows (d) – (f) and (j) – (l): reconstructed by FISTA with processed data.	127
6.3	Reconstructions of real permittivity of two targets by 20 DBIM iterations. First and third rows (a) – (c) and (g) – (i): reconstructed by FISTA with original data. Second and fourth rows (d) – (f) and (j) – (l): reconstructed by FISTA with processed data.	128
6.4	LSM results of cylindrical target cases. (a) Single target. (b) Two targets.	130
6.5	Classification of cylindrical target cases by LSM, (a) single target, and (b) two targets.	131
6.6	Classification of cylindrical target cases by DBIM, (a) single target, and (b) two targets.	131
6.7	Classification of cylindrical target cases after intersection, (a) single tar- get, and (b) two targets.	132
6.8	Classification of the CST Zubal phantom case. (a) LSM. (b) DBIM. (C) After intersection.	132

List of Tables

- 3.1 Debye parameters for the Zubal head phantom. 62
- 4.1 FEM simulation model number and description. 69
- 4.2 Relative errors and time of the FEM simulation models 69
- 5.1 Average running time for each antenna. 105
- 5.2 Reconstruction errors for Case I. 108
- 5.3 Reconstruction errors for Case II. 113
- 5.4 Reconstruction errors for Case III. 120
- 5.5 Reconstruction errors for experimental case. 121

Chapter 1

Introduction

1.1 Motivation, aim, and objectives

Over the last century, medical imaging techniques have developed rapidly and have been used in clinical diagnostics for tomographic imaging, including MRI, positron emission tomography (PET), and computed tomography (CT). Each technique can provide useful information about the tissues to be imaged. CT can provide excellent resolution images, but it uses X-rays, which has a risk of exposure to radiation [1], [2]. PET uses radioactive materials to visualise and measure changes in metabolic processes and can detect tumour tissues at an early stage, but with limited resolution [3], [4]. MRI can produce images based on the amount of absorption energy of different types of tissues using radio waves and strong magnetic fields with high resolution. However, the cost of MRI is high [5], [6]. With respect to the limitations of the abovementioned techniques, alternative imaging methods for diagnostics with low-cost and safe techniques are in need.

In recent years, MWI is gaining increasing interest worldwide for its potential to be used in medical imaging applications such as breast cancer detection and stroke detection [7]–[16]. As a non-invasive technique, MWI is harmless to human bodies, as the level of radiation used in MWI is estimated to be comparable to the levels used in cell phones [8], [17]. Moreover, it can be designed as a portable and low-cost device with the help of current computing power and hardware advances in the telecommunication industries [18]–[20], allowing the initial diagnosis of acute cerebrovascular disease such as stroke

in an ambulance or at home [21].

The aim of MWI for medical applications is to develop a fast and accurate MWI system that can efficiently collect and process measurement data, including the hardware device and the imaging algorithms [22]. The hardware consisting of antennas and other hardware components should be developed in a portable way that is suitable for usage in different diagnostic scenarios with environmental noise. Imaging algorithms should be able to produce reliable results such as diagnostic images in a short time, which is the main focus of this thesis. The main objectives are development of novel imaging algorithms with efficiency and robustness, creation of test models for the algorithms, and algorithm validation with numerical and experimental dataset.

1.2 Background

MWI techniques use EM waves in the frequency range from 300 MHz to 300 GHz [23] to detect or reconstruct a target by radar-based imaging or MWT. MWI is based on MWs which propagate inside a region to be investigated, where the EM wave is scattered by different kinds of materials. The scattered field is received and can be used to produce information of the region as it is related to the dielectric properties of the region [24].

MWI can be used in medical applications to retrieve information of the abnormal tissues inside the body, given that the abnormal tissues may have high contrast relative to normal human tissue [7], [8] due to the higher water content [25]. The dielectric properties of human tissues have been studied and reported in a wide range of frequencies in [26]–[29]. The dielectric properties of breast tissues and head tissues have been measured in [30]–[32] and in [33]–[35] respectively. There are also open-source data about dielectric properties provided by IFAC-CNR [36] and IT’IS Foundation [37].

MW has a wide band of frequency range, however, as the frequency increases, the

penetration depth of the EM wave decreases rapidly while the resolution increases. The frequency range varies depending on the application of MWI techniques. For radar-based imaging, which is based on the backscattered response of ultra-wideband (UWB) signals, the frequency range can be higher than 10 GHz [38], [39]. In contrast, MWT uses scattered signals obtained from a set of transmitters and receivers, and the frequency range is usually between 0.5 and 3.0 GHz. Moreover, for different imaging applications, the frequency range can be more rigorous due to the complexity of the tissue [8]. The higher frequency range for breast vs. head is related to stronger reflections and losses of head tissues.

The challenges of MWI should also be addressed for experiment equipment and imaging methodology [22], [40], [41]. An important experimental challenge is how to efficiently couple MW power into biological tissues when using coupling liquids, increasing the loss of microwave power [42]. The usage of coupling liquid gives rise to difficulties in the implementation of the MWI clinical system, including antenna configuration, which should be designed properly to properly couple power into human tissues [43]. The trade-off between frequency and resolution should be balanced to obtain a reliable image. A large dynamic range, *i.e.*, the ratio of the highest signal level to the lowest signal level that an antenna can handle, is needed to achieve weak scattered fields due to the discontinuity of the material. System noise and loss in the experimental environment should also be handled efficiently [44], including the reflection from system equipment and air, cables, connectors, *etc.* Accurate calibration methods can be used to enhance the signal measured by the system [45]. For the methodological level, modelling biological tissues is a challenging task, as it is hard to obtain prior information of the tissue such as shape and material property to reduce the modelling error between simulation and measurement. The nonlinearity of the ISP requires development of a robust, accurate, and fast imaging

algorithm, especially for 3-D imaging problems.

1.3 Overview of microwave imaging

There are mainly two types of MWI methods, radar-based imaging and MWT. Both use scattered signals of EM waves, while monostatic data (data obtained from an antenna that is used as transmitter and receiver simultaneously) are usually discarded for MWT.

1.3.1 Radar-based imaging

In some applications of MWI, the aim is not to obtain the dielectric properties of tissues but to detect and locate abnormal tissues such as tumours, called qualitative imaging. A simplified computational problem is considered and solved by only seeking to recognise the scatterer. Various radar-based imaging algorithms have been developed to focus the signal scattered from the target back to the antenna's location, such as confocal MWI [46], [47], space-time beamforming [48], [49], time-reversal [50], tissue sensing adaptive radar [51], and the Huygens-based radar algorithm [52].

These techniques can use UWB signals to obtain the backscatter response from the investigated region, including signals received by the transmitter antenna and the receiver antennas. The confocal MWI uses time-shifting and summation of backscattered signals but has difficulties in inhomogeneous scenarios with varying dielectric materials. The time-reversal algorithm is based on the assumption that the time-reversed received signal focuses back to the source point. The space-time beamforming uses filters to compensate for dispersion and fractional time delays by solving a penalised least-square problem. The tissue sensing adaptive radar is similar to confocal imaging but assigns more weight to the antennas, close to the focal point. The Huygens-based radar algorithm uses the Huygens principle to forward-propagate the waves, which removes the need to solve inverse

problems without any inversion technique or matrix generation.

1.3.2 Microwave tomography

Instead of only locating or detecting the target, MWT aims to generate images of tissues based on values of the dielectric properties, including relative permittivity and conductivity, by solving an EM ISP [53]. It is also called quantitative imaging as it estimates the distribution of the dielectric properties quantitatively.

The MWT system consists of two parts, including the data acquisition system to obtain measurement data and the imaging algorithms to perform image reconstructions. The data acquisition system consists of an antenna array, which is connected to electrical devices to produce and receive signals. The investigated region is usually surrounded by a set of antennas that are used as transmitters and receivers. Each transmitter illustrates an EM wave signal at a time, and then the scattered signal is collected by the receiver antennas and used for imaging algorithms. The setup is usually immersed in a lossy homogeneous matching medium to reduce reflection from the air-region interface.

Various kinds of MWT algorithms have been developed based on the Born approximation [54], such as the Born iterative method (BIM) [55] and the DBIM [56], or the source type integral equation [57], such as contrast source inversion (CSI) [58]. These proposed algorithms have been tested with numerical and experimental data for basic scenarios of cylindrical targets and then further applied to complex scenarios such as breast imaging and head imaging.

Several groups worldwide have studied MWT with their own developed systems. The Dartmouth group has first tested clinical usage of MWI for breast [59] and recently developed a 16 channel system by transmitting switch using monopole antennas [60] for breast imaging using a Gauss-Newton (GN) inversion algorithm with the FEM. Their

system has components of isolation and shielding to reduce the noise signals that propagate back to the system. A FEM-based imaging algorithm with CSI has been proposed by LoVetri from the University of Manitoba [61] for breast imaging. They have created an experimental breast phantom which is 3-D printed with polylactic acid and placed in an experimental chamber. They have also developed machine learning algorithms to classify the reconstruction results [62]. The group from King's College London aims at brain/head imaging, and a system using virtual network analyzer (VNA) with eight ports has been used with triangular monopole antennas [63]. They have also developed antennas with metamaterials to enhance the antenna performance [64]–[66], which leads to improved reconstruction results. Another group from CNR-IREA has also developed MWI algorithms based on virtual experiments and combined with the linear sampling method (LSM) [67]. Recently, they have developed a MWI head imaging system using FEM as the forward solver and truncated singular value decomposition (TSVD) as the inverse solver, and the monopole antennas are used and placed inside bricks filled with coupling liquid [68].

Recently, several algorithms have been proposed that use neural networks to improve reconstructed images [69]–[72]. They first use a back-propagation method to obtain initial reconstruction results, which are later enhanced by neural networks, but only applied to basic scenarios.

1.4 Contributions

The main contributions of this thesis are the development of MWI algorithms, including data processing, wave simulation, and reconstruction techniques. These algorithms are validated with simple and complex models in both numerical and experimental scenarios.

- The FISTA algorithm has been applied in MWT for the first time with DBIM, called

the DBIM-FISTA approach. (Ch.3)

- An FEM-based DBIM approach has been proposed, which is computationally efficient compared to the traditional approach and can also use the proposed FISTA algorithm. (Ch.3)
- The simplified scalar Green's function has been used in 3-D MWT and compared with the vectorial Green's function for complex head imaging scenarios. (Ch.3, Ch.5)
- A GPU-based FDTD forward solver is implemented with the help of the CUDA toolkit, and it is further combined with the 3-D DBIM-FISTA approach. (Ch.5)
- The proposed algorithm is validated with different numerical and experimental phantoms, including basic cylindrical targets and complex head phantoms such as the specific anthropomorphic mannequin (SAM) model and the Zubal head phantom. A preliminary study has been conducted that investigates the possibility of reconstructing anatomically complex head phantoms for the first time. (Ch.3, Ch.4, Ch.5)
- A signal processing technique has been proposed for MWI data and shows good reconstruction results. A postprocessing technique for MWI images is used to classify the reconstructed target and the background. (Ch.6)

The publications related to the above contributions are listed as the following two parts for the author's main work (first author publications) and collaboration work, respectively.

A. Publication list as first author

- (1) P. Lu, J. Córcoles and P. Kosmas, "Non-linear Microwave Imaging Using Fast Iterative Shrinkage Thresholding," *2019 Photonics & Electromagnetics Research Sympo-*

1.4. CONTRIBUTIONS

- sium - Spring (PIERS-Spring)*, 2019, pp. 1949-1956. (Ch.3, Ch.4)
- (2) P. Lu, J. Córcoles and P. Kosmas, “Tools for the Efficient Implementation of the DBIM Algorithm in Microwave Imaging Experiments,” *2020 14th European Conference on Antennas and Propagation (EuCAP)*, 2020, pp. 1-4. (Ch.2, Ch.3, Ch.6)
- (3) P. Lu, S. Ahsan and P. Kosmas, “Preliminary Study on the Feasibility of Reconstructing Anatomically Complex Numerical Brain Phantoms with Limited Prior Information,” *2020 XXXIIIrd General Assembly and Scientific Symposium of the International Union of Radio Science*, 2020, pp. 1-4.(Ch. 3, Ch. 4)
- (4) P. Lu, J. Córcoles and P. Kosmas, “Enhanced FEM-Based DBIM Approach for Two-Dimensional Microwave Imaging,” *IEEE Transactions on Antennas and Propagation*, Aug. 2021, vol. 69, no. 8, pp. 5187-5192. (Ch. 3, Ch.4)
- (5) P. Lu, and P. Kosmas, “Three-Dimensional Microwave Head Imaging with GPU-Based FDTD and the DBIM Method,” *Sensors*, 2022, no. 7: 2691. (Ch.2, Ch.3, Ch.5)

B. Publication list as coauthor

- (1) J. Córcoles, P. Lu and P. Kosmas, “Finite Element Analysis of a Wideband Microwave Tomography System for Potential Medical Imaging,” *2019 Joint International Symposium on Electromagnetic Compatibility, Sapporo and Asia-Pacific International Symposium on Electromagnetic Compatibility (EMC Sapporo/APEMC)*, 2019, pp. 358-361. (Ch.2 and Ch.3)
- (2) O. Karadima, M. Rahman, I. Sotiriou, N. Ghavami, P. Lu, S. Ahsan, and P. Kosmas, “Experimental Validation of Microwave Tomography with the DBIM-TwIST

- Algorithm for Brain Stroke Detection and Classification,” *Sensors*, 2020, no. 3: 840. (Ch.2, Ch.3, Ch. 4, Ch.5)
- (3) M. A. Mansoori, P. Lu and M. R. Casu, “FPGA Acceleration of 3D FDTD for Multi-Antennas Microwave Imaging Using HLS,” *IEEE Access*, 2021, vol. 9, pp. 122696-122711. (Ch.5)
- (4) E. Razzicchia, P. Lu, W. Guo, O. Karadima, I. Sotiriou, N. Ghavami, E. Kallos, G. Palikaras, and P. Kosmas, “Metasurface-Enhanced Antennas for Microwave Brain Imaging,” *Diagnostics*, 2021, no. 3: 424. (Ch.2, Ch.3)
- (5) O. Karadima, P. Lu and P. Kosmas, “Comparison of 2-D and 3-D DBIM-TwIST for Brain Stroke Detection and Differentiation,” *2021 15th European Conference on Antennas and Propagation (EuCAP)*, 2021, pp. 1-4. (Ch.2, Ch.3, Ch.4, Ch.5)
- (6) E. Razzicchia, P. Lu, W. Guo and P. Kosmas, “A New Metasurface-Enhanced Microstrip Patch Antenna for Haemorrhagic Stroke Detection,” *2021 15th European Conference on Antennas and Propagation (EuCAP)*, 2021, pp. 1-4. (Ch.2, Ch.3)
- (7) O. Karadima, P. Lu, I. Sotiriou and P. Kosmas, “Evaluation of Prior Information in Microwave Tomography Experiments for Brain Stroke Detection,” *2021 IEEE Conference on Antenna Measurements and Applications*, 2021, pp. 535-539. (Ch.2, Ch.3, Ch.4)
- (8) N. Ghavami, E. Razzicchia, O. Karadima, P. Lu, W. Guo, I. Sotiriou, E. Kallos, G. Palikaras, and P. Kosmas, “The Use of Metasurfaces to Enhance Microwave Imaging: Experimental Validation for Tomographic and Radar-Based Algorithms,” *IEEE Open Journal of Antennas and Propagation*, 2022, vol. 3, pp. 89-100. (Ch. 2, Ch.3, Ch.4)

- (9) O. Karadima, P. Lu, I. Sotiriou, and P. Kosmas, “Experimental Validation of the DBIM-TwIST Algorithm for Brain Stroke Detection and Differentiation Using a Multi-Layered Anatomically Complex Head Phantom,” *IEEE Open Journal of Antennas and Propagation*, 2022, vol. 3, pp. 274-286. (Ch.2, Ch.3, Ch.4)

1.5 Overview of the thesis

The remainder of the thesis is organised as follows. Chapter 2 reviews background MWI theory topics related to the development of our imaging algorithms. Chapter 3 details the proposed methods, focusing mainly on the mathematical formulation of the DBIM matrix building approach. The tools and models used in this thesis are introduced in this chapter, including numerical models such as the SAM model and the Zubal phantom, as well as experimental models. Chapter 4 presents the reconstruction results of our proposed 2-D FDTD-based and FEM-based DBIM approaches. Chapter 5 details the implementation of an in-house 3-D GPU-based FDTD forward solver for our 3-D DBIM-FISTA algorithm and presents reconstruction results with the 3-D head phantom models, which are compared with the 2-D reconstruction results. Chapter 6 presents preprocessing and postprocessing techniques for MWI based on our approach. Chapter 7 concludes the work of this thesis and discusses future work.

Chapter 2

Fundamentals and Related Work

2.1 Overview of background methods

In this chapter, the fundamental knowledge of MW theory is reviewed, including the methods to simulate EM wave propagation and solve the non-linear EM ISP, as well as techniques for linear inverse problems.

In MWI, an EM wave (excitation signal) is produced by the transmitter antenna, and it propagates in the region to be investigated. After it is scattered by different materials inside the region, the EM wave is received by a set of receiver antennas. These scattered signals are related to the permittivity and conductivity of the region, which can be used to reconstruct the dielectric profile.

A MWT algorithm usually consists of two components, the forward solver and the inverse solver. The forward solver is used to simulate the wave propagation and produce the simulated scattered signals received by the antenna. The simulated result is combined with the data from measurement to build the linear system by imaging algorithms. Finally, the inverse solver is used to solve the linear system and obtain the solution that is the dielectric contrast.

Several numerical algorithms are used to solve the computational electromagnetic (CEM) problems based on Maxwell's equations, including integral and differential equation solvers. The two widely used integral equation solvers are the discrete dipole approximation (DDA) [73], [74] and the method of moments (MoM) [75], [76]. The DDA calcu-

lates scattering and absorption properties using an approximation of the continuum target by a finite array of polarisable dipole points. MoM solves a system of linear equations by the application of appropriate boundary conditions. The differential equation solvers include finite integration technique (FIT) , FDTD, FEM, *etc.* The FIT uses a spatial discretisation scheme and covers all fields of electromagnetism, which was first proposed in 1977 [77]. It has also been used and developed in the commercial software CST Studio Suite. The FDTD approximates the partial derivatives by finite difference and solves Maxwell's equations in the time domain, which was first proposed by Yee [78]. The FEM was first used to solve the partial differential equation (PDE), which approximates the solution by discrete the region into smaller parts of elements. It has been extended to be used in electromagnetic society to solve EM problems such as wave propagation [79].

Among these numerical methods, MoM, FEM, and FDTD are most commonly used in MWI. MoM automatically incorporates radiation conditions, which works better for far-field problems, and it is efficient for perfectly conducting surfaces but does not handle inhomogeneous materials well. Compared with MoM and FEM, FDTD is easy to implement and provides solutions at multiple frequencies. FEM is good at dealing with complex structures with the usage of flexible meshes. However, FEM is hard to implement as it requires complex mathematical formulations, and the FEM matrix may be difficult to solve when large problems are considered, as in 3-D cases.

Over the last three decades, MWT algorithms [80]–[83] have been developed rapidly with the help of increased computer power. Born and Rytov approximations have been first introduced to MWT for weak scatterers. However, these two methods assume that the EM inverse linear scattering problem is linear and are unsuitable for practical problems with strong scattering materials [84]. An iterative method has been proposed based on the GN algorithm [85], which seeks to build a set of linear equations with unknowns

and solves the problem iteratively. The CSI is another iterative method to retrieve the value of the contrast of scattering objects by minimising a source functional based on the source type integral equation [58]. The Born approximation has been modified to an iterative version in [55], which is called the BIM, to solve ISPs where Born approximation fails. The DBIM is further proposed, which is equivalent to the GN method [86]. The Green's function of DBIM is updated at each iteration, which is different from the BIM as the Green's function of BIM remains unchanged. The DBIM has a faster convergence compared with BIM, while BIM is more robust to noise [56], and both show better performance than non-iterative linear inversion with the Born approximation.

Solvers for the resulting linear system obtained by linearizing the EM ISP with the Born approximation are essential as well. The ISP is ill-posed (a problem is well-posed if its solution exists, is unique, and depends continuously on the data) as the solution of ISPs may not be unique or continuous on the data, and the resulting linear system is ill-conditioned as the number of rows of the matrix is much smaller than the number of columns. If the inverse solver is not properly used, wrong solutions may be obtained due to the ill-posedness of the problem, resulting in false reconstruction images. The most commonly used inverse solvers are GD methods such as the GD algorithms, the conjugate gradient method for least squares (CGLS) , and the least squares with QR-factorisation (LSQR) [87], [88]. However, due to the ill-conditioned linear system, iterative solvers with regularisation terms are usually required to obtain a robust and stable solution. Tikhonov regularisation is a regularisation method that helps inverse solvers to regularise the solution. Recently, inverse solvers using advanced techniques have also been used in MWI, such as the iterative shrinkage thresholding algorithm (ISTA), which solves the linear system with the shrinkage operator [89].

2.2 Electromagnetic wave propagation

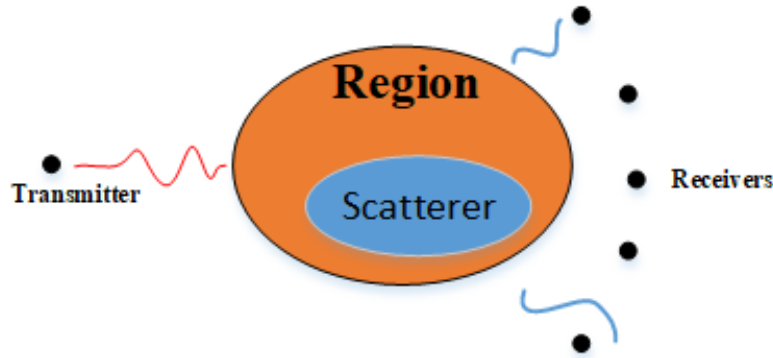


Figure 2.1: EM wave propagation.

In MWI, the EM wave is produced by an excitation signal, and it propagates inside a region as shown in Fig. 2.1. The EM wave, scattered by different materials and reflected by the interfaces inside the region, travels from the transmitter antenna to the receiver antenna and carries dielectric information of the region.

2.2.1 Maxwell's equations

Maxwell's equations are a set of equations that describes the relation between magnetic and electric fields and how they interact and propagate inside materials. There are different forms of Maxwell's equations, and the differential form governing EM wave propagation is described as follows,

$$\begin{aligned}
 \text{Faraday's law:} & \quad \frac{\partial \vec{\mathbf{B}}}{\partial t} + \vec{\mathbf{M}} = -\nabla \times \vec{\mathbf{E}}. \\
 \text{Ampere's law:} & \quad \frac{\partial \vec{\mathbf{D}}}{\partial t} + \vec{\mathbf{J}} = \nabla \times \vec{\mathbf{H}}. \\
 \text{Gauss's law for electric field:} & \quad \nabla \cdot \vec{\mathbf{D}} = 0. \\
 \text{Gauss's law for magnetic field:} & \quad \nabla \cdot \vec{\mathbf{B}} = 0.
 \end{aligned} \tag{2.1}$$

2.2. ELECTROMAGNETIC WAVE PROPAGATION

where $\vec{\mathbf{B}}$ is the magnetic flux density (Wb/m^2), $\vec{\mathbf{E}}$ is the electric field (V/m), $\vec{\mathbf{D}}$ is the electric flux density (C/m^2), $\vec{\mathbf{H}}$ is the magnetic field (A/m), $\vec{\mathbf{M}}$ is the magnetic current density (V/m) and $\vec{\mathbf{J}}$ is the electric current density (A/m^2). In non-dispersive material, of which the dielectric properties are independent of wave frequency, $\vec{\mathbf{D}}$ and $\vec{\mathbf{B}}$ can be represented by simple relations as,

$$\begin{aligned}\vec{\mathbf{D}} &= \epsilon \vec{\mathbf{E}} = \epsilon_0 \epsilon_r \vec{\mathbf{E}}, \\ \vec{\mathbf{B}} &= \mu \vec{\mathbf{H}} = \mu_0 \mu_r \vec{\mathbf{H}},\end{aligned}\tag{2.2}$$

where $\epsilon_0 = 8.854 \times 10^{-12} F/m$ and $\mu_0 = 4\pi \times 10^{-7} H/m$ are the free-space permittivity and permeability, ϵ_r and μ_r are the relative permittivity and permeability, When only electric source is used (which is the usually the case as there is no magnetic source in reality), i.e. $\vec{\mathbf{J}} = \vec{\mathbf{J}}_{\text{source}} + \sigma \vec{\mathbf{E}}$ and $\vec{\mathbf{M}} = \sigma^* \vec{\mathbf{H}}$ where σ and σ^* are electric conductivity and magnetic loss, the partial differential form of (2.1) is given by,

$$\begin{aligned}\frac{\partial \vec{\mathbf{H}}}{\partial t} &= -\frac{1}{\mu} \nabla \times \vec{\mathbf{E}} - \frac{1}{\mu} \sigma^* \vec{\mathbf{H}}, \\ \frac{\partial \vec{\mathbf{E}}}{\partial t} &= \frac{1}{\epsilon} \nabla \times \vec{\mathbf{H}} - \frac{1}{\epsilon} (\vec{\mathbf{J}}_{\text{source}} + \sigma \vec{\mathbf{E}}).\end{aligned}\tag{2.3}$$

As each of the vectorial fields has three components, including the x -, y - and z -components, the time-dependent vectorial equation (2.3) can be rewritten in six scalar equations in Cartesian coordinates as,

$$\begin{aligned}
 \frac{\partial H_x}{\partial t} &= \frac{1}{\mu} \left(\frac{\partial E_y}{\partial z} - \frac{\partial E_z}{\partial y} - \sigma^* H_x \right), \\
 \frac{\partial H_y}{\partial t} &= \frac{1}{\mu} \left(\frac{\partial E_z}{\partial x} - \frac{\partial E_x}{\partial z} - \sigma^* H_y \right), \\
 \frac{\partial H_z}{\partial t} &= \frac{1}{\mu} \left(\frac{\partial E_x}{\partial y} - \frac{\partial E_y}{\partial x} - \sigma^* H_z \right), \\
 \frac{\partial E_x}{\partial t} &= \frac{1}{\epsilon} \left(\frac{\partial H_z}{\partial y} - \frac{\partial H_y}{\partial z} - J_x - \sigma E_x \right), \\
 \frac{\partial E_y}{\partial t} &= \frac{1}{\epsilon} \left(\frac{\partial H_x}{\partial z} - \frac{\partial H_z}{\partial x} - J_y - \sigma E_y \right), \\
 \frac{\partial E_z}{\partial t} &= \frac{1}{\epsilon} \left(\frac{\partial H_y}{\partial x} - \frac{\partial H_x}{\partial y} - J_z - \sigma E_z \right),
 \end{aligned} \tag{2.4}$$

where J_x , J_y and J_z denote the x -, y -, and z -components of $\vec{\mathbf{J}}_{\text{source}}$.

The analytical solutions of (2.4) are usually not possible to obtain. To this end, numerical methods like FDTD and FEM are required to approximate the solution of the differential form of Maxwell's equations. Similarly, the solution of other forms of Maxwell's equations should also be obtained by numerical methods, for example, DDA and MoM can be used to solve the integral format of Maxwell's equations.

For 2-D problems, a reduced set of equations are considered. The three modes for 2-D EM wave propagation are transverse magnetic (TM) mode, transverse electric (TE) mode and transverse electromagnetic (TEM) mode, where some components of the electric and magnetic fields are zero. The TM mode is considered for the 2-D problems as z -polarised antenna is considered, where H_x , H_y , E_z are nonzero and H_z , E_x , E_y are zero. Thus, (2.4) can be reduced to the following 2-D form,

$$\begin{aligned}
 \frac{\partial H_x}{\partial t} &= \frac{1}{\mu} \left(-\frac{\partial E_z}{\partial y} - \sigma^* H_x \right), \\
 \frac{\partial H_y}{\partial t} &= \frac{1}{\mu} \left(\frac{\partial E_z}{\partial x} - \sigma^* H_y \right), \\
 \frac{\partial E_z}{\partial t} &= \frac{1}{\epsilon} \left(\frac{\partial H_y}{\partial x} - \frac{\partial H_x}{\partial y} - J_z - \sigma E_z \right).
 \end{aligned} \tag{2.5}$$

2.2.2 Finite difference time domain method

2.2.2.1 Discretisation scheme of Maxwell's equations

FDTD method is one of the numerical approximation methods for solving EM wave propagation problems based on the finite difference method which uses finite differences to approximate the derivatives of differential equations. By Taylor's theorem, a Taylor series expansion is built as for a function f at point x with a small step Δx ,

$$f(x + \Delta x) = f(x) + \frac{f'(x)}{1!}\Delta x + \frac{f^{(2)}(x)}{2!}\Delta x^2 + \dots + \frac{f^{(n)}(x)}{n!}\Delta x^n + \dots \quad (2.6)$$

The approximated first-order derivative, when the items with second-order or higher are assumed to be small and ignored, is written as,

$$\frac{\partial f}{\partial x} \approx \frac{f(x + \Delta x) - f(x)}{\Delta x}, \quad (2.7)$$

which is called the first-order forward difference. There are also central difference and backward difference schemes written respectively as,

$$\frac{\partial f}{\partial x} \approx \frac{f(x + \frac{\Delta x}{2}) - f(x - \frac{\Delta x}{2})}{\Delta x}, \quad (2.8)$$

$$\frac{\partial f}{\partial x} \approx \frac{f(x) - f(x - \Delta x)}{\Delta x}. \quad (2.9)$$

The central difference is used for the discretisation of time and space in the FDTD method in this thesis. Higher-order finite difference can also be used to increase accuracy and reduce numerical dispersion, such as the FDTD method with second-order in time and fourth-order in space [90], [91].

To approximate Maxwell's equations in the time domain, Yee first proposed a scheme

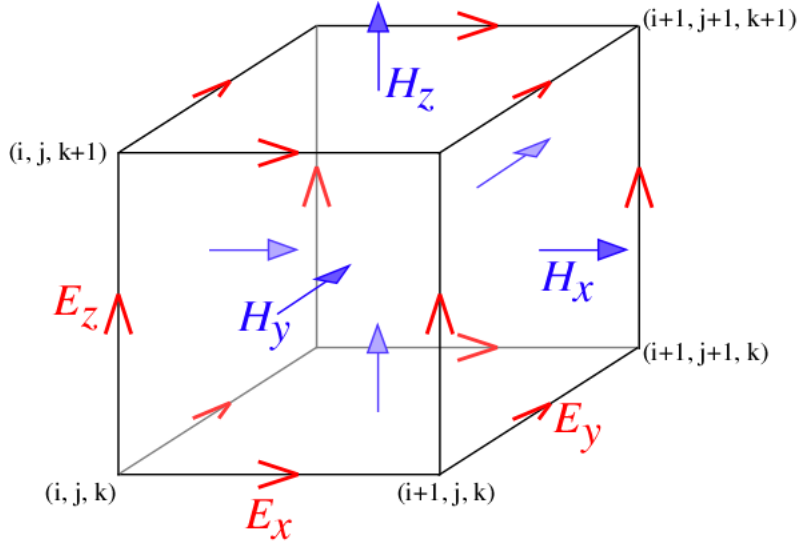


Figure 2.2: Scheme of Yee's lattice. (source:https://meep.readthedocs.io/en/latest/Yee_Lattice/)

to discretise the electric and magnetic fields with time t , and introduced Yee's lattice as shown in Fig. 2.2 [78], where electric fields are calculated at the middle point of each edge and magnetic fields are calculated at the centre point of each surface. Assuming the discretisation steps for each dimension are Δx , Δy and Δz respectively, *i.e.* $(i, j, k) = (i\Delta x, j\Delta y, k\Delta z)$, the partial differential form of Maxwell's equations can be discretised as the following procedure using finite difference when the central difference is used for the time and space derivatives, E_x for example,

$$\begin{aligned} \frac{E_x|_{i+\frac{1}{2},j,k}^{n+\frac{1}{2}} - E_x|_{i+\frac{1}{2},j,k}^{n-\frac{1}{2}}}{\Delta t} = & \frac{1}{\epsilon_{i+\frac{1}{2},j,k}} \left(\frac{H_z|_{i+\frac{1}{2},j+\frac{1}{2},k}^n - H_z|_{i+\frac{1}{2},j-\frac{1}{2},k}^n}{\Delta y} \right. \\ & - \frac{H_y|_{i+\frac{1}{2},j+\frac{1}{2},k+\frac{1}{2}}^n - H_y|_{i+\frac{1}{2},j+\frac{1}{2},k-\frac{1}{2}}^n}{\Delta z} \\ & \left. - J_x|_{i+\frac{1}{2},j,k}^n - \sigma_{i+\frac{1}{2},j,k} \frac{E_x|_{i+\frac{1}{2},j,k}^{n+\frac{1}{2}} + E_x|_{i+\frac{1}{2},j,k}^{n-\frac{1}{2}}}{2} \right), \end{aligned} \quad (2.10)$$

where ϵ_r and σ are considered as constants inside each voxel, and the electric field for

2.2. ELECTROMAGNETIC WAVE PROPAGATION

σE is calculated by the semi-implicit approximation, which is the average value between previous time step $n - \frac{1}{2}$ and current time step $n + \frac{1}{2}$ as

$$E_x|_{i+\frac{1}{2},j,k}^n = \frac{E_x|_{i+\frac{1}{2},j,k}^{n+\frac{1}{2}} + E_x|_{i+\frac{1}{2},j,k}^{n-\frac{1}{2}}}{2}. \quad (2.11)$$

Rearranging the terms in (2.10), the following equation is obtained for updating E_x at each time step,

$$\begin{aligned} E_x|_{i+\frac{1}{2},j,k}^{n+\frac{1}{2}} &= \frac{2\varepsilon_{i+\frac{1}{2},j,k} - \sigma_{i+\frac{1}{2},j,k}\Delta t}{2\varepsilon_{i+\frac{1}{2},j,k} + \sigma_{i+\frac{1}{2},j,k}\Delta t} E_x|_{i+\frac{1}{2},j,k}^{n-\frac{1}{2}} \\ &+ \frac{2\Delta t}{2\varepsilon_{i+\frac{1}{2},j,k} + \sigma_{i+\frac{1}{2},j,k}\Delta t} \left(\frac{H_z|_{i+\frac{1}{2},j+\frac{1}{2},k}^n - H_z|_{i+\frac{1}{2},j-\frac{1}{2},k}^n}{\Delta y} \right. \\ &\quad \left. - \frac{H_y|_{i+\frac{1}{2},j+\frac{1}{2},k+\frac{1}{2}}^n - H_y|_{i+\frac{1}{2},j+\frac{1}{2},k-\frac{1}{2}}^n}{\Delta z} - J_x|_{i+\frac{1}{2},j,k}^n \right), \end{aligned} \quad (2.12)$$

where J_x is the x -component of the source.

Similarly, equations for updating E_y and E_z are constructed as follows,

$$\begin{aligned} E_y|_{i,j+\frac{1}{2},k}^{n+\frac{1}{2}} &= \frac{2\varepsilon_{i,j+\frac{1}{2},k} - \sigma_{i,j+\frac{1}{2},k}\Delta t}{2\varepsilon_{i,j+\frac{1}{2},k} + \sigma_{i,j+\frac{1}{2},k}\Delta t} E_y|_{i,j+\frac{1}{2},k}^{n-\frac{1}{2}} \\ &+ \frac{2\Delta t}{2\varepsilon_{i,j+\frac{1}{2},k} + \sigma_{i,j+\frac{1}{2},k}\Delta t} \left(\frac{H_x|_{i,j+\frac{1}{2},k+\frac{1}{2}}^n - H_x|_{i,j+\frac{1}{2},k-\frac{1}{2}}^n}{\Delta z} \right. \\ &\quad \left. - \frac{H_z|_{i+\frac{1}{2},j+\frac{1}{2},k}^n - H_z|_{i-\frac{1}{2},j+\frac{1}{2},k}^n}{\Delta x} - J_y|_{i+\frac{1}{2},j,k}^n \right), \end{aligned} \quad (2.13)$$

$$\begin{aligned} E_z|_{i,j,k+\frac{1}{2}}^{n+\frac{1}{2}} &= \frac{2\varepsilon_{i,j,k+\frac{1}{2}} - \sigma_{i,j,k+\frac{1}{2}}\Delta t}{2\varepsilon_{i,j,k+\frac{1}{2}} + \sigma_{i,j,k+\frac{1}{2}}\Delta t} E_z|_{i,j,k+\frac{1}{2}}^{n-\frac{1}{2}} \\ &+ \frac{2\Delta t}{2\varepsilon_{i,j,k+\frac{1}{2}} + \sigma_{i,j,k+\frac{1}{2}}\Delta t} \left(\frac{H_y|_{i+\frac{1}{2},j,k+\frac{1}{2}}^n - H_y|_{i-\frac{1}{2},j,k+\frac{1}{2}}^n}{\Delta x} \right. \\ &\quad \left. - \frac{H_x|_{i,j+\frac{1}{2},k+\frac{1}{2}}^n - H_x|_{i,j-\frac{1}{2},k+\frac{1}{2}}^n}{\Delta y} - J_z|_{i,j,k+\frac{1}{2}}^n \right). \end{aligned} \quad (2.14)$$

2.2. ELECTROMAGNETIC WAVE PROPAGATION

The finite difference equations for the magnetic field components can be also derived by analogy as,

$$\begin{aligned}
 H_x|_{i,j+\frac{1}{2},k+\frac{1}{2}}^{n+1} &= \frac{2\mu_{i,j+\frac{1}{2},k+\frac{1}{2}} - \sigma_{i,j+\frac{1}{2},k+\frac{1}{2}}^* \Delta t}{2\mu_{i,j+\frac{1}{2},k+\frac{1}{2}} + \sigma_{i,j+\frac{1}{2},k+\frac{1}{2}}^* \Delta t} H_x|_{i,j+\frac{1}{2},k+\frac{1}{2}}^n \\
 &+ \frac{2\Delta t}{2\mu_{i,j+\frac{1}{2},k+\frac{1}{2}} + \sigma_{i,j+\frac{1}{2},k+\frac{1}{2}}^* \Delta t} \left(\frac{E_y|_{i,j+\frac{1}{2},k+1}^{n+\frac{1}{2}} - E_y|_{i,j+\frac{1}{2},k}^{n+\frac{1}{2}}}{\Delta z} \right. \\
 &\left. - \frac{E_z|_{i,j+1,k+\frac{1}{2}}^{n+\frac{1}{2}} - E_z|_{i,j,k+\frac{1}{2}}^{n+\frac{1}{2}}}{\Delta y} \right), \tag{2.15}
 \end{aligned}$$

$$\begin{aligned}
 H_y|_{i+\frac{1}{2},j,k+\frac{1}{2}}^{n+1} &= \frac{2\mu_{i+\frac{1}{2},j,k+\frac{1}{2}} - \sigma_{i+\frac{1}{2},j,k+\frac{1}{2}}^* \Delta t}{2\mu_{i+\frac{1}{2},j,k+\frac{1}{2}} + \sigma_{i+\frac{1}{2},j,k+\frac{1}{2}}^* \Delta t} H_y|_{i+\frac{1}{2},j,k+\frac{1}{2}}^n \\
 &+ \frac{2\Delta t}{2\mu_{i+\frac{1}{2},j,k+\frac{1}{2}} + \sigma_{i+\frac{1}{2},j,k+\frac{1}{2}}^* \Delta t} \left(\frac{E_z|_{i+1,j,k+\frac{1}{2}}^{n+\frac{1}{2}} - E_z|_{i,j,k+\frac{1}{2}}^{n+\frac{1}{2}}}{\Delta x} \right. \\
 &\left. - \frac{E_x|_{i+\frac{1}{2},j,k+1}^{n+\frac{1}{2}} - E_x|_{i+\frac{1}{2},j,k}^{n+\frac{1}{2}}}{\Delta z} \right), \tag{2.16}
 \end{aligned}$$

$$\begin{aligned}
 H_z|_{i+\frac{1}{2},j+\frac{1}{2},k}^{n+1} &= \frac{2\mu_{i+\frac{1}{2},j+\frac{1}{2},k} - \sigma_{i+\frac{1}{2},j+\frac{1}{2},k}^* \Delta t}{2\mu_{i+\frac{1}{2},j+\frac{1}{2},k} + \sigma_{i+\frac{1}{2},j+\frac{1}{2},k}^* \Delta t} H_z|_{i+\frac{1}{2},j+\frac{1}{2},k}^n \\
 &+ \frac{2\Delta t}{2\mu_{i+\frac{1}{2},j+\frac{1}{2},k} + \sigma_{i+\frac{1}{2},j+\frac{1}{2},k}^* \Delta t} \left(\frac{E_x|_{i+\frac{1}{2},j+1,k}^{n+\frac{1}{2}} - E_x|_{i+\frac{1}{2},j,k}^{n+\frac{1}{2}}}{\Delta y} \right. \\
 &\left. - \frac{E_y|_{i+1,j+\frac{1}{2},k}^{n+\frac{1}{2}} - E_y|_{i,j+\frac{1}{2},k}^{n+\frac{1}{2}}}{\Delta x} \right). \tag{2.17}
 \end{aligned}$$

The resulting three equations have a similar form to that of the electric equations. For the scenarios considered in this work, as well as in most MWI applications, the materials are usually non-metallic materials. The permeability of the region is constant and equal to free space permeability, and the magnetic loss is nearly zero $\mu = \mu_0$ and $\sigma^* = 0$. Thus,

2.2. ELECTROMAGNETIC WAVE PROPAGATION

(2.15), (2.16) and (2.17) are reduced to a simplified version as,

$$H_x|_{i,j+\frac{1}{2},k+\frac{1}{2}}^{n+1} = H_x|_{i,j+\frac{1}{2},k+\frac{1}{2}}^n + \frac{\Delta t}{\mu_0} \left(\frac{E_y|_{i,j+\frac{1}{2},k+1}^{n+\frac{1}{2}} - E_y|_{i,j+\frac{1}{2},k}^{n+\frac{1}{2}}}{\Delta z} - \frac{E_z|_{i,j+1,k+\frac{1}{2}}^{n+\frac{1}{2}} - E_z|_{i,j,k+\frac{1}{2}}^{n+\frac{1}{2}}}{\Delta y} \right), \quad (2.18)$$

$$H_y|_{i+\frac{1}{2},j,k+\frac{1}{2}}^{n+1} = H_y|_{i+\frac{1}{2},j,k+\frac{1}{2}}^n + \frac{\Delta t}{\mu_0} \left(\frac{E_z|_{i+1,j,k+\frac{1}{2}}^{n+\frac{1}{2}} - E_z|_{i,j,k+\frac{1}{2}}^{n+\frac{1}{2}}}{\Delta x} - \frac{E_x|_{i+\frac{1}{2},j,k+1}^{n+\frac{1}{2}} - E_x|_{i+\frac{1}{2},j,k}^{n+\frac{1}{2}}}{\Delta z} \right), \quad (2.19)$$

$$H_z|_{i+\frac{1}{2},j+\frac{1}{2},k}^{n+1} = H_z|_{i+\frac{1}{2},j+\frac{1}{2},k}^n + \frac{\Delta t}{\mu_0} \left(\frac{E_x|_{i+\frac{1}{2},j+1,k}^{n+\frac{1}{2}} - E_x|_{i+\frac{1}{2},j,k}^{n+\frac{1}{2}}}{\Delta y} - \frac{E_y|_{i+1,j+\frac{1}{2},k}^{n+\frac{1}{2}} - E_y|_{i,j+\frac{1}{2},k}^{n+\frac{1}{2}}}{\Delta x} \right). \quad (2.20)$$

For 2-D TM wave propagation, the finite difference equations of magnetic fields can be reduced as well for H_x and H_y ,

$$H_x|_{i,j+\frac{1}{2},k+\frac{1}{2}}^{n+1} = H_x|_{i,j+\frac{1}{2},k+\frac{1}{2}}^n + \frac{\Delta t}{\mu_0} \left(-\frac{E_z|_{i,j+1,k+\frac{1}{2}}^{n+\frac{1}{2}} - E_z|_{i,j,k+\frac{1}{2}}^{n+\frac{1}{2}}}{\Delta y} \right), \quad (2.21)$$

$$H_y|_{i+\frac{1}{2},j,k+\frac{1}{2}}^{n+1} = H_y|_{i+\frac{1}{2},j,k+\frac{1}{2}}^n + \frac{\Delta t}{\mu_0} \left(\frac{E_z|_{i+1,j,k+\frac{1}{2}}^{n+\frac{1}{2}} - E_z|_{i,j,k+\frac{1}{2}}^{n+\frac{1}{2}}}{\Delta x} \right). \quad (2.22)$$

With the expressions of the finite difference equations, the values of each component at any voxel point can be calculated successively, and the new value of the current time step is only related to the value at the previous time step. This allows updating each component simultaneously of the electric field or magnetic field, and the computation can be designed in parallel.

To achieve stability and reduce numerical dispersion, the Courant-Friedrich-Levy condition must be satisfied [92] to limit the time step t ,

$$\Delta t \leq \frac{1}{c \sqrt{\frac{1}{\Delta x^2} + \frac{1}{\Delta y^2} + \frac{1}{\Delta z^2}}}, \quad (2.23)$$

where c is the speed of the EM wave.

According to the Nyquist sampling theorem, the discretisation step $\Delta h = \frac{\lambda}{n_d}$ (Δx , Δy or Δz) should be smaller than $\frac{\lambda}{2}$. However, larger n_d (much smaller Δh) is required to ensure the accuracy of the FDTD method for practical problems, which is usually between 10 and 40.

2.2.2.2 Convolutional perfectly matched layer

The simulation region in the computer is limited for numerical algorithms, while the real scenario of EM wave propagation is unlimited and unbounded. A computational domain in simulation should be large enough to include the area of interest, and a suitable absorbing condition must be used to extend the domain to infinity. Therefore, the absorbing boundary condition (ABC) is needed to absorb the outgoing waves from the computational region and avoid reflections from the boundaries [93].

Analytical ABCs are first used by constructing operators that expand the outgoing wave, for example, the one presented in [94]. An alternative approach to implement ABCs is to add extra layers as absorbing materials with only a few cells thick, which has more utility compared with analytical ABCs. A highly effective ABC material called the perfectly matched layer (PML) [95] was proposed by Berenger in 1994. PML is widely used as it has the capacity to terminate areas of inhomogeneous, dispersive, anisotropic, and even nonlinear materials, which was not possible with analytical ABCs. PML is proven to be a robust and efficient technique to terminate the FDTD lattices [92].

Based on Berenger's work, PMLs with modifications to enhance performance were proposed [96]–[101]. Two advanced PMLs of them are usually considered, which are called the uniaxial perfectly matched layer (UPML), proposed by Gedney [100], [101], and the convolutional perfectly matched layer (CPML) proposed by Roden and Gedney

[99]. The UPML formulation is based on Maxwell's equations and more efficient than PMLs [101]. While CPML accommodates more general metric tensor coefficients, leading to improved absorption and reduced computational memory. CPML is highly robust in isotropic and homogeneous media, and it can also be used in inhomogeneous, lossy, dispersive, anisotropic, or nonlinear media without any further modifications [99]. With respect to UPML, CPML has a better performance as it is independent of the host media and easy to implement [92], [102].

The formulation of CPML for the x -component of Ampere's law is constructed as,

$$j\omega\epsilon E_x + \sigma E_x = \frac{1}{s_y} \frac{\partial H_z}{\partial y} - \frac{1}{s_z} \frac{\partial H_y}{\partial z}, \quad (2.24)$$

where $s_i = \kappa_i + \frac{\sigma_i}{\alpha_i + j\omega\epsilon_0}$, $i = x, y$ or z , and α_i and σ_i are assumed to be positive real and κ_i is real and ≥ 1 . In time domain, (2.24) is transformed to,

$$\epsilon \frac{\partial E_x}{\partial t} + \sigma E_x = \bar{s}_y(t) * \frac{\partial H_z}{\partial y} - \bar{s}_z(t) * \frac{\partial H_y}{\partial z}, \quad (2.25)$$

where \bar{s}_i is the inverse Laplace transform of s_i^{-1} and $*$ represents for the convolution operator. Based on Yee's grid, the above equation can be discretised as,

$$\begin{aligned} & \epsilon_r \epsilon_0 \frac{E_x|_{i+\frac{1}{2},j,k}^{n+\frac{1}{2}} - E_x|_{i+\frac{1}{2},j,k}^{n-\frac{1}{2}}}{\Delta t} + \sigma \frac{E_x|_{i+\frac{1}{2},j,k}^{n+\frac{1}{2}} + E_x|_{i+\frac{1}{2},j,k}^{n-\frac{1}{2}}}{2} \\ &= \frac{H_z|_{i+\frac{1}{2},j+\frac{1}{2},k}^n - H_z|_{i+\frac{1}{2},j-\frac{1}{2},k}^n}{\kappa_y \Delta y} - \frac{H_y|_{i+\frac{1}{2},j,k+\frac{1}{2}}^n - H_y|_{i+\frac{1}{2},j,k-\frac{1}{2}}^n}{\kappa_z \Delta z} + \psi_{e_{xy}}|_{i+\frac{1}{2},j,k}^n - \psi_{e_{xz}}|_{i+\frac{1}{2},j,k}^n. \end{aligned} \quad (2.26)$$

2.2. ELECTROMAGNETIC WAVE PROPAGATION

The coefficients are calculated as,

$$\begin{aligned}\psi_{e_{xy}}|_{i+\frac{1}{2},j,k}^n &= b_y \psi_{e_{xy}}|_{i+\frac{1}{2},j,k}^{n-1} + a_y \frac{H_z|_{i+\frac{1}{2},j+\frac{1}{2},k}^n - H_z|_{i+\frac{1}{2},j-\frac{1}{2},k}^n}{\Delta y}, \\ \psi_{e_{xz}}|_{i+\frac{1}{2},j,k}^n &= b_z \psi_{e_{xz}}|_{i+\frac{1}{2},j,k}^{n-1} + a_z \frac{H_y|_{i+\frac{1}{2},j,k+\frac{1}{2}}^n - H_y|_{i+\frac{1}{2},j,k-\frac{1}{2}}^n}{\Delta z},\end{aligned}\quad (2.27)$$

where

$$a_p = \frac{\sigma_p}{\sigma_p \kappa_p + \kappa_p^2 \alpha_p} (e^{-(\frac{\sigma_p}{\kappa_p} + \alpha_p) \frac{\Delta t}{\epsilon_0}} - 1) \text{ and } b_p = e^{-(\frac{\sigma_p}{\kappa_p} + \alpha_p) \frac{\Delta t}{\epsilon_0}}. \quad (2.28)$$

According to [92], the optimal value σ_{opt} of σ_{max} is computed as,

$$\sigma_{\text{opt}} = \frac{0.8(m+1)}{\eta_0 \Delta \sqrt{\epsilon_r \mu_r}}, \quad (2.29)$$

where m and m_α are the orders for polynomial grading, and the related parameters in (2.28) at position d_p of the whole CPML layer with d are calculated as $\sigma_p(d_p) = (\frac{d_p}{d})^m \sigma_{\text{opt}}$, $\kappa_p(d_p) = 1 + (\kappa_{p,\text{max}} - 1)(\frac{d_p}{d})^m$, $\alpha_p(d_p) = \alpha_{p,\text{max}}(\frac{d-d_p}{d})^{m_\alpha}$.

2.2.2.3 Debye model for dispersive materials

Materials are called dispersive when the dielectric properties are frequency-dependent, which means the permittivity and conductivity change as the frequency changes [92]. Modelling dispersive materials in FDTD is important in MWI to simulate wave propagation in biological tissues that are dispersive. Different models are proposed to modelling dispersive materials such as Lorentz model [103], Debye model [104] and Drude model [105]. In this thesis, the single-pole Debye model [106] is used in FDTD as,

$$\epsilon_r = \epsilon'_r - j\epsilon''_r = \epsilon_\infty + \frac{\Delta\epsilon}{1 + j\omega\tau} + \frac{\sigma_s}{j\omega\epsilon_0} = \epsilon_\infty + \frac{\epsilon_s - \epsilon_\infty}{1 + j\omega\tau} + \frac{\sigma_s}{j\omega\epsilon_0}, \quad (2.30)$$

2.2. ELECTROMAGNETIC WAVE PROPAGATION

where τ is the relaxation time of the single-pole Debye model, ϵ_s is the static relative permittivity, ϵ_∞ is the relative permittivity at infinite frequency, $\Delta\epsilon$ is the change in relative permittivity, and σ_s is the static conductivity. An additional equation for updating the pole current density \vec{J}_p due to the Debye model requires to be solved as [92],

$$\vec{J}_p + \tau \frac{\partial \vec{J}_p}{\partial t} = \epsilon_0 \Delta \epsilon \frac{\partial \vec{E}}{\partial t}. \quad (2.31)$$

The above equation can be discretised using the same finite difference scheme as,

$$\frac{\vec{J}_p^{n+\frac{1}{2}} + \vec{J}_p^{n-\frac{1}{2}}}{2} + \tau \frac{\vec{J}_p^{n+\frac{1}{2}} - \vec{J}_p^{n-\frac{1}{2}}}{\Delta t} = \epsilon_0 \Delta \epsilon \frac{\vec{E}_p^{n+\frac{1}{2}} - \vec{E}_p^{n-\frac{1}{2}}}{\Delta t}, \quad (2.32)$$

which can be further calculated using the same procedure as (2.10) and (2.12). The resulted current density \vec{J}_p should be included in the previous current density as $\vec{J} = \sigma \vec{E} + \vec{J}_{\text{source}} + \vec{J}_p$.

2.2.3 Finite element method

FEM is another widely used numerical method to approximate solutions to partial differential equations arising in EM propagation problems. In this thesis, only 2-D FEM is considered, as 3-D FEM is not easy to implement, and it is inefficient for MWI problems due to large matrix computations. A TM wave equation in terms of the longitudinal component of the electric field E_z is described as,

$$\Delta_t E_z + \omega^2 \mu_0 \epsilon_0 \epsilon_r E_z = j \omega \mu_0 J_z, \quad (2.33)$$

where Δ_t is the transverse Laplacian operator, J_z is current density of the z -directed source, and the permeability is considered to be μ_0 for the materials used in this work.

2.2. ELECTROMAGNETIC WAVE PROPAGATION

For any region S bounded by a closed boundary C , the formulation of Galerkin's method for (2.33) is given by [107],

$$\iint_S W \nabla_t \cdot \nabla_t E_z dS + k_0^2 \iint_S \epsilon_r W E_z dS = j\omega\mu_0 \iint_S W J_z dS, \quad (2.34)$$

where ∇_t is the transverse nabla operator, W is the weighting function, and k_0 is the wavenumber with $k_0^2 = \omega^2\mu_0\epsilon_0$. By applying Green's first identity,

$$\iint_S W \nabla_t \cdot \nabla_t E_z dS + \iint_S \nabla_t W \cdot \nabla_t E_z dS = \oint_C W \frac{\partial E_z}{\partial n} dC, \quad (2.35)$$

to the left-hand side item in (2.34) which includes ∇_t , the second order derivatives are eliminated and (2.34) is reduced to

$$\iint_S \nabla_t W \cdot \nabla_t E_z dS - k_0^2 \iint_S \epsilon_r W E_z dS - \oint_C W \frac{\partial E_z}{\partial n} dC = -j\omega\mu_0 \iint_S W J_z dS. \quad (2.36)$$

An ABC is also required in FEM to simulate EM wave propagation in a limited computational domain and eliminate the outgoing waves. A circular second-order boundary condition of Bayliss and Turkel [108] is employed for the boundary C in a cylindrical coordinate system (ρ, ϕ) as,

$$\oint_C W \frac{\partial E_z}{\partial n} dC = -a(\rho) \oint_C W E_z dC + \frac{b(\rho)}{\rho^2} \oint_C W \frac{\partial^2 E_z}{\partial \phi^2} dC, \quad (2.37)$$

where ρ is the radius of the circular boundary C , $a(\rho) = jk + \frac{1}{2\rho} - \frac{b(\rho)}{4\rho^2}$, $b(\rho) = \frac{1}{2(jk + \frac{1}{\rho})}$. Integrating by parts of the second-order derivative and substituting the boundary item in

(2.36) yields,

$$\begin{aligned} \iint_S \nabla_t W \cdot \nabla_t E_z dS - k_0^2 \iint_S \epsilon_r W E_z dS + a(\rho) \oint_C W E_z dC + b(\rho) \oint_C \frac{\partial W}{\partial C} \frac{\partial E_z}{\partial C} dC \\ = -j\omega\mu_0 \iint_S W J_z dS. \end{aligned} \quad (2.38)$$

Solving this integral-differential equation by FEM requires subdividing the region S into N_e finite elements. Moreover, the electric field E_z in each of the elements is approximated by a linear combination of nodal basis functions [107]. Different FEM elements can be used, including triangular element, rectangular element, *etc.* In this work, the triangular elements are used for decomposition, as shown in Fig. 2.3. The electric field E_z^n in the

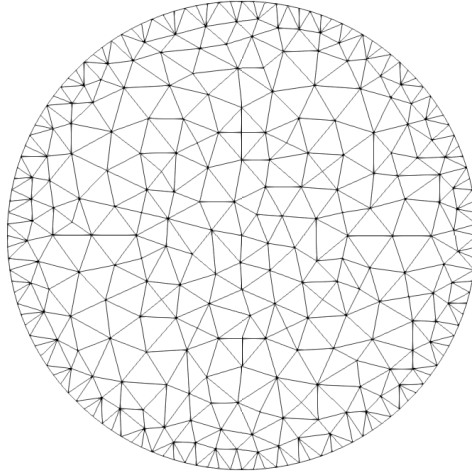


Figure 2.3: Mesh of the finite element method with triangular elements.

n -th element is then approximated as,

$$E_z^n = \sum_{p=1}^{p^n} e_p^n \phi_p^n, \quad (2.39)$$

which is a combination of the basis function ϕ_p^n weighted with the values of the degrees of freedom (d.o.f) and e_p^n at each node p of the triangular element n with P^n being the number of d.o.f of each element.

After the standard application of the FEM [107], the local matrix equation expressing the contribution from a single triangular element n to the global linear system of equations, assuming the permittivity to be constant over the triangle, takes the form

$$(\mathbf{K}^n - \omega^2 \mu_0 \epsilon_0 \epsilon_r^n \mathbf{M}^n + \mathbf{D}^n) \mathbf{e}_i^n = -j\omega \mu_0 \mathbf{f}_i^n. \quad (2.40)$$

The local matrices in the above equation are constructed (for every entry in row p and column q , with $p = 1 \dots P^n, q = 1 \dots P^n$) as the following integrations of the basis functions and its derivatives:

$$\begin{aligned} \{\mathbf{K}^n\}_{pq} &= \iint_{S^n} \nabla_t \phi_p^n(\mathbf{r}) \cdot \nabla_t \phi_q^n(\mathbf{r}) dS, \\ \{\mathbf{M}^n\}_{pq} &= \iint_{S^n} \phi_p^n(\mathbf{r}) \phi_q^n(\mathbf{r}) dS, \\ \{\mathbf{f}_i^n\}_p &= \iint_{S^n} \phi_p^n(\mathbf{r}) J(\mathbf{r}_i) dS, \\ \{\mathbf{D}^n\}_{pq} &= \int_{C^n} \left(a_C \phi_p^n(\mathbf{r}) \phi_q^n(\mathbf{r}) + b_C \frac{\partial \phi_p^n(\mathbf{r})}{\partial C} \frac{\partial \phi_q^n(\mathbf{r})}{\partial C} \right) dC, \end{aligned} \quad (2.41)$$

where \mathbf{f}_i^n is $\mathbf{0}$ except in the elements with a node where the source is placed. Matrix \mathbf{D}^n is only evaluated on the contour C of S , where analytical second-order absorbing boundary conditions of Bayliss and Turkel through coefficients a_C and b_C [107] are used to eliminate the reflection of the outgoing waves. After the assembly procedure [107] of every local system in (2.40), the values of the d.o.f in the whole domain for every different source can be obtained by solving the multiple right-hand side (RHS) global linear system in the form of $\mathbf{SE} = -j\omega \mu_0 \mathbf{F}$. A direct factorisation method is used since the solution can be easily obtained for every different source once the system matrix is factorised. For a

simulation domain with N_d d.o.f and N_a sources, the dimensions of \mathbf{E} and \mathbf{F} are $N_d \times N_a$.

2.3 Basics of the inverse scattering problem theory

2.3.1 Direct (forward) scattering problems

The direct EM wave scattering satisfies the following Helmholtz equation at position \mathbf{r} with a source $\vec{\mathbf{J}}_0$,

$$\nabla \times \frac{1}{\mu} \nabla \times \vec{\mathbf{E}}(\mathbf{r}) - \omega^2 \epsilon \vec{\mathbf{E}}(\mathbf{r}) = -j\omega \vec{\mathbf{J}}_0(\mathbf{r}), \quad (2.42)$$

which is also written as,

$$\nabla^2 \vec{\mathbf{E}}(\mathbf{r}) + \omega^2 \epsilon \mu \vec{\mathbf{E}}(\mathbf{r}) = j\omega \mu [\mathbf{I} + \frac{\nabla \nabla}{k^2}] \cdot \vec{\mathbf{J}}_0(\mathbf{r}), \quad (2.43)$$

where

$$\nabla^2 = \nabla \cdot \nabla = \Delta = \frac{\partial^2}{\partial x^2} + \frac{\partial^2}{\partial y^2} + \frac{\partial^2}{\partial z^2}, \quad \nabla \nabla = \begin{bmatrix} \frac{\partial^2}{\partial x^2} & \frac{\partial^2}{\partial x \partial y} & \frac{\partial^2}{\partial x \partial z} \\ \frac{\partial^2}{\partial y \partial x} & \frac{\partial^2}{\partial y^2} & \frac{\partial^2}{\partial y \partial z} \\ \frac{\partial^2}{\partial z \partial x} & \frac{\partial^2}{\partial z \partial y} & \frac{\partial^2}{\partial z^2} \end{bmatrix}. \quad (2.44)$$

The solution of the above direct scattering equation inside a region V is given by [109],

$$\vec{\mathbf{E}}(\mathbf{r}) = -j\omega \mu \int_V \vec{\mathbf{J}}_0(\mathbf{r}') \cdot \vec{\mathbf{G}}(\mathbf{r}', \mathbf{r}) d\mathbf{r}'. \quad (2.45)$$

The electric field $\vec{\mathbf{E}}$ can be computed with the dyadic Green's function $\vec{\mathbf{G}}$, and the formulation of the dyadic Green's function is constructed as follows,

$$\begin{aligned}
 \vec{\mathbf{G}}(\mathbf{r}', \mathbf{r}) &= [\mathbf{I} + \frac{\nabla' \nabla'}{k^2}] g(\mathbf{r}', \mathbf{r}) \\
 &= \begin{bmatrix} 1 & 0 & 0 \\ 0 & 1 & 0 \\ 0 & 0 & 1 \end{bmatrix} g(\mathbf{r}', \mathbf{r}) + \begin{bmatrix} \frac{\partial^2}{\partial x^2} & \frac{\partial^2}{\partial x \partial y} & \frac{\partial^2}{\partial x \partial z} \\ \frac{\partial^2}{\partial y \partial x} & \frac{\partial^2}{\partial y^2} & \frac{\partial^2}{\partial y \partial z} \\ \frac{\partial^2}{\partial z \partial x} & \frac{\partial^2}{\partial z \partial y} & \frac{\partial^2}{\partial z^2} \end{bmatrix} \frac{g(\mathbf{r}', \mathbf{r})}{k^2} \\
 &= \begin{bmatrix} k^2 + \frac{\partial^2}{\partial x^2} & \frac{\partial^2}{\partial x \partial y} & \frac{\partial^2}{\partial x \partial z} \\ \frac{\partial^2}{\partial y \partial x} & k^2 + \frac{\partial^2}{\partial y^2} & \frac{\partial^2}{\partial y \partial z} \\ \frac{\partial^2}{\partial z \partial x} & \frac{\partial^2}{\partial z \partial y} & k^2 + \frac{\partial^2}{\partial z^2} \end{bmatrix} \frac{g(\mathbf{r}', \mathbf{r})}{k^2},
 \end{aligned} \tag{2.46}$$

where

$$g(\mathbf{r}', \mathbf{r}) = \frac{e^{ik|\mathbf{r}' - \mathbf{r}|}}{4\pi|\mathbf{r}' - \mathbf{r}|} \tag{2.47}$$

, is the scalar Green's function.

The Green's function also holds that $\vec{\mathbf{G}}(\mathbf{r}', \mathbf{r}) = \vec{\mathbf{G}}^T(\mathbf{r}, \mathbf{r}')$ according to reciprocity. Therefore, the solution (2.45) also has the following form,

$$\vec{\mathbf{E}}(\mathbf{r}) = -j\omega\mu \int_V \vec{\mathbf{G}}(\mathbf{r}, \mathbf{r}') \cdot \vec{\mathbf{J}}_0(\mathbf{r}') d\mathbf{r}'. \tag{2.48}$$

2.3.2 Formulation of inverse scattering problem

Subtracting the known background terms $\nabla \times \frac{1}{\mu_b} \nabla \times \vec{\mathbf{E}}(\mathbf{r}) - \omega^2 \epsilon_b \vec{\mathbf{E}}(\mathbf{r})$ from both sides of (2.42), the following inverse scattering equation is obtained as,

$$\nabla \times \left(\frac{1}{\mu} - \frac{1}{\mu_b} \right) \nabla \times \vec{\mathbf{E}}(\mathbf{r}) - \omega^2 (\epsilon - \epsilon_b) \vec{\mathbf{E}}(\mathbf{r}) = -j\omega \vec{\mathbf{J}}_0(\mathbf{r}) - \nabla \times \frac{1}{\mu_b} \nabla \times \vec{\mathbf{E}}(\mathbf{r}) + \omega^2 \epsilon_b \vec{\mathbf{E}}(\mathbf{r}). \tag{2.49}$$

With the following equation, which the dyadic Green's function satisfies,

$$\nabla \times \frac{1}{\mu_b} \nabla \times \vec{\mathbf{G}}(\mathbf{r}, \mathbf{r}') - \omega^2 \epsilon_b \vec{\mathbf{G}}(\mathbf{r}, \mathbf{r}') = \frac{1}{\mu_b} \mathbf{I} \delta(\mathbf{r} - \mathbf{r}'), \quad (2.50)$$

the solution of (2.49) can be obtained,

$$\begin{aligned} \vec{\mathbf{E}}(\mathbf{r}) = & -j\omega \int_V \mu_b \vec{\mathbf{G}}(\mathbf{r}, \mathbf{r}') \cdot \vec{\mathbf{J}}_0(\mathbf{r}') d\mathbf{r}' + \omega^2 \int_V \mu_b (\epsilon - \epsilon_b) \vec{\mathbf{G}}(\mathbf{r}, \mathbf{r}') \cdot \vec{\mathbf{E}}(\mathbf{r}') d\mathbf{r}' \\ & - \int_V \mu_b \vec{\mathbf{G}}(\mathbf{r}, \mathbf{r}') \cdot \nabla' \times \left(\frac{1}{\mu} - \frac{1}{\mu_b} \right) \nabla' \times \vec{\mathbf{E}}(\mathbf{r}') d\mathbf{r}', \end{aligned} \quad (2.51)$$

where the first term in the RHS is the known incident field $\vec{\mathbf{E}}_{\text{inc}}(\mathbf{r}')$. Considering $\mu_b = \mu_0$, (2.51) is reduced to,

$$\vec{\mathbf{E}}(\mathbf{r}) = \vec{\mathbf{E}}_{\text{inc}}(\mathbf{r}) + \omega^2 \mu_0 \epsilon_0 \int_V O(\mathbf{r}') \vec{\mathbf{G}}(\mathbf{r}, \mathbf{r}') \cdot \vec{\mathbf{E}}(\mathbf{r}') d\mathbf{r}', \quad (2.52)$$

where $O(\mathbf{r}') = \epsilon_r(\mathbf{r}') - \epsilon_b(\mathbf{r}')$ is the contrast of the relative permittivity (to simplify, ϵ_b is used to represent the relative permittivity of background case) and $\vec{\mathbf{E}}$ is called the total field.

In ISPs, the electric field can be recorded at the antennas only, which are outside the reconstruction region (the region to be investigated), with an example shown in Fig. 2.4. The integral part in (2.52) is related to the total field inside the reconstruction region, and it contains information of the scatterer. The inverse scattering equation (2.52) is nonlinear due to that the total field is related to contrast of permittivity.

Approximations are usually needed to solve the nonlinear equation (2.52) as the electric field $\vec{\mathbf{E}}$ unknown inside the reconstruction domain. Born approximation replaces the

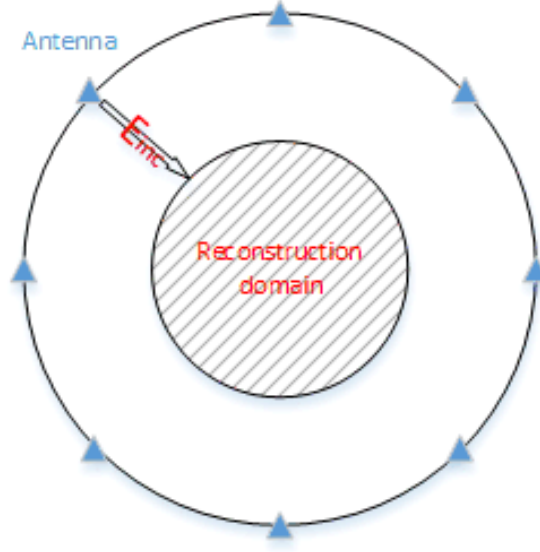


Figure 2.4: Example of inverse scattering scenario.

total field $\vec{\mathbf{E}}(\mathbf{r})$ inside the integral part by the known incident field $\vec{\mathbf{E}}_{\text{inc}}(\mathbf{r})$

$$\vec{\mathbf{E}}(\mathbf{r}) \approx \vec{\mathbf{E}}_{\text{inc}}(\mathbf{r}), \quad (2.53)$$

where $\vec{\mathbf{E}}_{\text{inc}}(\mathbf{r})$ is calculated by simulation algorithms with known background properties.

Thus, the total field in (2.52) can be approximated as,

$$\vec{\mathbf{E}}(\mathbf{r}) \approx \vec{\mathbf{E}}_{\text{inc}}(\mathbf{r}) + \omega^2 \mu_0 \epsilon_0 \int_V O(\mathbf{r}') \vec{\mathbf{G}}(\mathbf{r}, \mathbf{r}') \cdot \vec{\mathbf{E}}_{\text{inc}}(\mathbf{r}') d\mathbf{r}', \quad (2.54)$$

which is called as the first-order Born approximation and is linearly proportional to $O(\mathbf{r})$.

The integral part in (2.55) corresponds to the scattered field,

$$\vec{\mathbf{E}}_s(\mathbf{r}) = \omega^2 \mu_0 \epsilon_0 \int_V O(\mathbf{r}') \vec{\mathbf{G}}(\mathbf{r}, \mathbf{r}') \cdot \vec{\mathbf{E}}_{\text{inc}}(\mathbf{r}') d\mathbf{r}', \quad (2.55)$$

which is suitable for solving weak scatterer problems. However, when the scatterers

are strong, advanced techniques are required to reduce the influence of the first-order approximation.

2.3.3 Linear sampling method

The LSM is one of the common techniques to solve ISPs of a similar scenario as in Fig. 2.4 qualitatively, which estimates the shape of the target. The LSM is derived from the following far-field integral equation for a TM wave as [110],

$$\mathcal{F}(\Phi) = \int_V E_s(\mathbf{r}_n, \phi) \Phi(\mathbf{r}, \phi) d\phi = G(\mathbf{r}_n, \mathbf{r}), \quad (2.56)$$

where \mathcal{F} is the far-field operator, E_s is the scattered field measured by the receiver antenna \mathbf{r}_n , Φ is a unknown indicator to be determined, and G is the Green's function. The LSM partitions the domain under investigation into a number of sampling points and calculates the following discrete equation at each point \mathbf{r} for a system with N_m transmitters and N_n receivers,

$$\mathbf{E}_s \vec{\Phi}(\mathbf{r}) = \vec{G}(\mathbf{r}), \quad (2.57)$$

where \mathbf{E}_s is a matrix of dimension $N_n \times N_m$ for the scattered field with $\mathbf{E}_s(i, j) = E_s(\mathbf{r}_i, \mathbf{r}_j)$ and monostatic data should be discarded when the antenna is used both as transmitter and receiver, $\vec{G}(\mathbf{r}) = [G(\mathbf{r}_1, \mathbf{r}), G(\mathbf{r}_2, \mathbf{r}), \dots, G(\mathbf{r}_n, \mathbf{r})]^T$ is a vector of Green's function of dimension $N_n \times 1$, $\vec{\Phi}(\mathbf{r}) = [\Phi(\mathbf{r}, \mathbf{r}_1), \Phi(\mathbf{r}, \mathbf{r}_2), \dots, \Phi(\mathbf{r}, \mathbf{r}_m)]^T$ is a indicator of dimension $N_m \times 1$ given by [111],

$$\vec{\Phi}(\mathbf{r}) = \sum_{i=1}^{\min(N_m, N_n)} \frac{\lambda_i}{\lambda_i^2 + \alpha} \langle \vec{G}(\mathbf{r}), \mathbf{u}_i \rangle \mathbf{v}_i, \quad (2.58)$$

where $\mathbf{u}_i, \lambda_i, \mathbf{v}_i$ are the left singular vector, singular value, and right singular vector of \mathbf{E}_s , such that $\mathbf{U}\mathbf{\Lambda}\mathbf{V}^T = \mathbf{E}_s$, $\mathbf{U} = [\mathbf{u}_1, \mathbf{u}_2, \dots, \mathbf{u}_n]$, $\mathbf{\Lambda} = \text{diag}(\lambda_1, \lambda_2, \dots, \lambda_m)$, $\mathbf{V} = [\mathbf{v}_1, \mathbf{v}_2, \dots, \mathbf{v}_m]$ are the singular value decomposition matrices, $\langle \cdot, \cdot \rangle$ represents the inner product, and α is a Tikhonov parameter. Since the right singular vectors \mathbf{v}_i are orthonormal, (2.58) can be calculated using the following expression as,

$$\|\vec{\Phi}(\mathbf{r})\|^2 = \sum_{i=1}^{\min(N_m, N_n)} \left(\frac{\lambda_i}{\lambda_i^2 + \alpha} \right)^2 |\langle \vec{G}(\mathbf{r}), \mathbf{u}_i \rangle|^2. \quad (2.59)$$

Moreover, as some of the singular values may be too small, the solution can be further improved with the TSVD which selects a number of largest singular values to compute [112].

2.3.4 Distorted Born iterative method

For scenarios including strong scatterers with increased nonlinearity, iterative solvers with advanced techniques must be used to solve the resulting nonlinear problems, for example, DBIM and BIM. The difference between DBIM and BIM is whether the Green's function is updated, for DBIM, or not, for BIM, at each iteration. The DBIM is proven to be equivalent to GN type method [86].

The DBIM is considered in this thesis, which solves nonlinear EM ISPs iteratively and reconstructs the spatial distribution of dielectric properties within a region V [113]. It is based on approximating the nonlinear integral equation, which describes the relationship of the electric field with the continuous spatial distribution of dielectric properties via the Born approximation. The nonlinear integral equation of the electric fields scattered by the object to be imaged for each transmitter-receiver (TR) pair $(\mathbf{r}_n, \mathbf{r}_m)$ can be written based

on (2.55) as,

$$\vec{\mathbf{E}}_s(\mathbf{r}_n, \mathbf{r}_m) = \omega^2 \mu_0 \epsilon_0 \int_V O(\mathbf{r}) \vec{\mathbf{G}}(\mathbf{r}_n, \mathbf{r}) \cdot \vec{\mathbf{E}}_b(\mathbf{r}, \mathbf{r}_m) d\mathbf{r}. \quad (2.60)$$

Assuming the dielectric property contrast is constant over each discretisation voxel, (2.60) can be discretised for each TR pair as,

$$\vec{\mathbf{E}}_s(\mathbf{r}_n, \mathbf{r}_m) = \omega^2 \mu_0 \epsilon_0 \sum_{\mathbf{r}_k \in V} O(\mathbf{r}_k) \int_{V_{\mathbf{r}_k}} \vec{\mathbf{G}}(\mathbf{r}_n, \mathbf{r}) \cdot \vec{\mathbf{E}}_b(\mathbf{r}, \mathbf{r}_m) d\mathbf{r}, \quad (2.61)$$

where \mathbf{r}_k is a point at the centre of each voxel $V_{\mathbf{r}_k}$. After computing the integral, this equation leads to a linear system using the process described in Section 3.1,

$$\mathbf{b} = \mathbf{A}\mathbf{x}, \quad (2.62)$$

where \mathbf{A} is a $M \times N$ matrix with M denotes the number of TR pairs and N denotes the number of voxels inside the reconstruction region V . The DBIM solves (2.61) iteratively until a preset stop criterion is satisfied. At each DBIM iteration i , after calculating the electric field and Green's function by the forward solver, (2.62) is built with a set of linear equations and solved by the inverse solver. The contrast is the solution \mathbf{x} of the linear system, which is used to update the background profile as $\epsilon_r^{i+1}(\mathbf{r}) = \epsilon_r^i(\mathbf{r}) + O(\mathbf{r})$.

2.4 Optimisation theory

The ISP can be recast as an optimisation problem by the following functional to be minimised as,

$$F = \alpha \|\vec{\mathbf{E}}_s(\mathbf{r}) - S(\mathbf{r})\|^2 + \beta Y, \quad (2.63)$$

where S is the nonlinear scattering operator $S(\mathbf{r}) = \omega^2 \mu_0 \epsilon_0 \int_V O(\mathbf{r}') \vec{\mathbf{G}}(\mathbf{r}, \mathbf{r}') \cdot \vec{\mathbf{E}}(\mathbf{r}') d\mathbf{r}'$, α and β are coefficients, and Y is the limitation of prior information. The original ISP is

nonlinear as there are two sets of unknowns in (2.52), the electric field $\vec{\mathbf{E}}$ inside the investigation domain and the dielectric properties of the scatterers. Due to the nonlinearity of the functional, many local minima may exist, and the algorithm may get stuck in these local minima and give a completely different solution. Therefore, the convergence towards global minima depends on the initial guess of the background profile, and a good initial guess can help reduce the nonlinearity of the problem.

The nonlinear ISP can be linearised by the first-order Born approximation, which approximates the unknown electric field inside the integral by the background electric field calculated by the forward solver. A linearised problem is then obtained by only considering the contrast function as unknown, and the minimisation of the functional can be achieved by linear inverse solvers. However, the resulting linear system is ill-posed, which requires powerful and mature regularisation linear solvers. For practical applications, iterative methods are usually considered to achieve a reliable solution, which alternatively updates the background profile and the electric field inside the reconstruction domain, such as the DBIM.

2.5 Inverse solvers for linear systems

The resulting linear system (2.62) is under-determined as $N \gg M$, which means that there are fewer equations than unknowns, and infinite solutions may exist. Advanced inverse solvers are required to guarantee a reliable solution for the considered ISP. Iterative solvers, approaching the solution gradually, are usually used instead of direct solvers, as iterative solvers are more robust to the ill-posed problems. The commonly used iterative solvers for ISPs are the GD-type algorithms such as CGLS and LSQR, and the ISTA-type algorithms such as [114], [115] the two-step iterative shrinkage thresholding (TwIST) algorithm [116] and the FISTA [117].

As matrix \mathbf{A} is ill-posed and under-determined, it is impractical to compute the inverse of \mathbf{A} as well as the solution of the linear system by $\mathbf{x} = \mathbf{A}^{-1}\mathbf{b}$. Thus, instead of solving (2.62) directly, a typical way is to minimise the following functional $f(x)$,

$$f(\mathbf{x}) = \frac{1}{2} \|\mathbf{Ax} - \mathbf{b}\|_2^2, \quad (2.64)$$

which aims to the optimal \mathbf{x} that minimises $f(\mathbf{x})$ based on the l_2 -norm $\|\mathbf{x}\|_2 = \sqrt{\sum x_i^2}$. Additional regularisation term $g(x)$ can be added to limit the solution with expected attribute such as prior information for MWI ISPs,

$$F(\mathbf{x}) = \frac{1}{2} \|\mathbf{Ax} - \mathbf{b}\|_2^2 + g(\mathbf{x}), \quad (2.65)$$

where $g(x)$ is usually a limitation of the solution \mathbf{x} .

2.5.1 Tikhonov regularisation

Tikhonov regularisation minimises the following object functional using the Tikhonov matrix Γ for a particular solution with desirable properties as,

$$F(\mathbf{x}) = \frac{1}{2} \|\mathbf{Ax} - \mathbf{b}\|_2^2 + \|\Gamma\mathbf{x}\|_2^2, \quad (2.66)$$

for some chosen Tikhonov matrix Γ . In many cases, a multiple of identity matrix \mathbf{I} can be used as the Tikhonov matrix $\Gamma = \alpha\mathbf{I}$ giving preference to solutions with smaller norms. This regularisation step improves the conditioning of the problem and enables a direct numerical solution expressed as,

$$\mathbf{x} = (\mathbf{A}^T\mathbf{A} + 2\alpha^2\mathbf{I})^{-1}\mathbf{A}^T\mathbf{b}. \quad (2.67)$$

2.5.2 Conjugate gradient for least squares

Algorithm 1 Conjugate gradient for least squares problems

```

 $\mathbf{x}_0 \leftarrow 0, \mathbf{d}_0 = \mathbf{b}, \mathbf{r}_0 = \mathbf{A}^T \mathbf{b}, \mathbf{p}_0 = \mathbf{r}_0, \mathbf{t}_0 = \mathbf{A} \mathbf{p}_0$ 
for  $k \leftarrow 1, 2, \dots$  until stop criterion do
   $\alpha_k = \frac{\|\mathbf{r}_{k-1}\|^2}{\|\mathbf{t}_{k-1}\|^2}$ 
   $\mathbf{x}_k = \mathbf{x}_{k-1} + \alpha_{k-1} \mathbf{p}_{k-1}$ 
   $\mathbf{d}_k = \mathbf{d}_{k-1} - \alpha_{k-1} \mathbf{t}_{k-1}$ 
   $\mathbf{r}_k = \mathbf{A}_k^T \mathbf{d}_k$ 
   $\beta_k = \frac{\|\mathbf{r}_k\|^2}{\|\mathbf{r}_{k-1}\|^2}$ 
   $\mathbf{p}_k = \mathbf{r}_k + \beta_k \mathbf{p}_{k-1}$ 
   $\mathbf{t}_k = \mathbf{A} \mathbf{p}_k$ 
end for

```

The matrix \mathbf{A} is asymmetric for the linear system (2.62), and hence it cannot be solved by the conjugate gradient methods in a straightforward manner. An equivalent system of normal equations can be used instead,

$$\mathbf{A}^T \mathbf{A} \mathbf{x} = \mathbf{A}^T \mathbf{b}, \quad (2.68)$$

where $\mathbf{A}^T \mathbf{A}$ is a symmetric matrix and can be seen as the new matrix. However, $\mathbf{A}^T \mathbf{A}$ is never computed and stored; instead, $\mathbf{A} \mathbf{x}$ is computed first and then with \mathbf{A}^T at each iteration of CGLS. This is because the computation of $\mathbf{A}^T \mathbf{A}$ could waste large computational time and memory. For large problems, especially 3-D problems, usually the computation of $\mathbf{A}^T \mathbf{A}$ could exceed the computer memory. The CGLS algorithm is shown in Algorithm 1.

2.5.3 Iterative shrinkage/thresholding methods

In ISPs, the solution needs to be limited to avoid large values. ISTAs define a solution x that minimises the convex object functional $F(x)$ with a least squares function $f(x)$ and a

penalty regulariser $g(x) = \lambda \Phi(\mathbf{x})$,

$$F(x) = \frac{1}{2} \|\mathbf{Ax} - \mathbf{b}\|_2^2 + \lambda \Phi(\mathbf{x}), \quad (2.69)$$

where $\lambda \in [0, +\infty]$ is a weighting parameter, and $\Phi(x)$ is a regularisation function, which is usually chosen as the l_1 -norm or l_2 -norm. The minimisation problem (2.69) can be solved different types of iterative thresholding methods, such as the ISTA [89] and the TwIST algorithm[118].

The basic ISTA algorithm updates the solution based on the following structure,

$$\mathbf{x}_{t+1} = \Psi_\lambda(\mathbf{x}_t + \frac{1}{L} \mathbf{A}^T(\mathbf{y} - \mathbf{Ax}_t)), \quad (2.70)$$

where $\Psi_\lambda(\mathbf{x})$ is the thresholding function, and L is the gradient step. The regularisation function is chosen to be the l_1 -norm in this thesis, *i.e.* $\Phi(\mathbf{x}) = \|\mathbf{x}\|_1$, resulting the soft thresholding operation as,

$$\Psi_\lambda(\mathbf{x}) = \text{sign}(\mathbf{x}) \max\{0, |\mathbf{x}| - \lambda\}, \quad (2.71)$$

where

$$\text{sign}(x) = \begin{cases} 1 & x > 0 \\ 0 & x = 0 \\ -1 & x < 0 \end{cases}. \quad (2.72)$$

Modified ISTA-type algorithms have been proposed to enhance performance, such as

the TwIST algorithm with the following two-step update structure,

$$\begin{aligned}\mathbf{x}_{t+1} &= (1 - \alpha)\mathbf{x}_{t-1} + (\alpha - \beta)\mathbf{x}_t + \beta\Gamma_\lambda(\mathbf{x}_t), \\ \Gamma_\lambda(\mathbf{x}) &= \Psi_\lambda(\mathbf{x} + \frac{1}{L}\mathbf{A}^T(\mathbf{y} - \mathbf{A}\mathbf{x})),\end{aligned}\tag{2.73}$$

where α and β are the parameters of the TwIST algorithm.

According to [119], the optimal parameters are chosen as,

$$\kappa = \frac{\xi_1}{\xi_m}, \rho = \frac{1 - \sqrt{\kappa}}{1 + \sqrt{\kappa}}, \alpha = \rho^2 + 1, \beta = \frac{2\alpha}{\xi_1 + \xi_m},\tag{2.74}$$

where ξ_1 and ξ_m are the smallest and largest eigenvalues of $\mathbf{A}^T\mathbf{A}$ respectively. To obtain a reliable solution, the parameters for the TwIST algorithm should be chosen appropriately, otherwise the algorithm may diverge and lead to a false solution. For MW ISPs, the parameters must be optimised specifically for the problem at hand [120].

2.6 Conclusion

In this chapter, the theory of EM wave propagation starting from the Maxwell equations has been introduced, which can be simulated by numerical methods. The mathematical formulations of FDTD and FEM have been reviewed, including ABCs, which are used to eliminate outgoing waves in a limited computational domain. The algorithm for solving inverse problems has been presented, including DBIM and LSM, with descriptions of inverse solvers followed. This chapter is the basis of the next chapter.

Chapter 3

Methodology for Developing and Testing the DBIM-FISTA MWI Algorithm

This chapter proposes the DBIM-FISTA approach for MWI applications with specific implemented FEM and FDTD forward solvers. The procedure for constructing the scattering matrix of the DBIM is described, including the mathematical formulation of Green's functions arising in the DBIM integral equation. The FISTA is applied to solve the resulting ill-posed and under-determined linear system by DBIM. Different numerical and experimental models used in this thesis are also introduced in this chapter, including basic cylindrical models and complex phantoms such as head and brain phantoms.

3.1 Methodology

3.1.1 Green's function with the DBIM algorithm

The forward EM propagation problem can be solved without involving calculation of Green's function. However, in the DBIM equation (2.60), the Green's function is an important part that must be calculated by using the results from the forward solver to construct the linear system. When a direct EM scattering problem (the background case) is considered, the Green's function holds the condition in association with the current and

the electric field as (2.48) [109],

$$\vec{\mathbf{E}}(\mathbf{r}) = -j\omega\mu_0 \int_V \vec{\mathbf{G}}(\mathbf{r}, \mathbf{r}') \cdot \vec{\mathbf{J}}_0(\mathbf{r}') d\mathbf{r}'. \quad (3.1)$$

Though the basic formulation of the Green's function is already presented in (2.46), it is not easy to compute and can be further simplified in the considered scenarios with a single-polarisation source to avoid calculating the partial derivatives. The relation (2.48) can be used to link the Green's function with the background electric field calculated by the forward solver.

Assuming a single-polarisation point source with intensity $\vec{\mathbf{I}}_0$ located at \mathbf{r}_0 is used, the electric current density $\vec{\mathbf{J}}_0$ has the following form,

$$\vec{\mathbf{J}}_0(\mathbf{r}) = \vec{\mathbf{I}}_0 L \delta(\mathbf{r} - \mathbf{r}_0), \quad (3.2)$$

where L is the length of source, the electric current is a vector

$$\vec{\mathbf{I}}_0 = [I_x, I_y, I_z]^T, \quad (3.3)$$

and the Dirac delta function $\delta(\mathbf{r} - \mathbf{r}_0)$ is infinity at \mathbf{r}_0 and zero elsewhere.

It should be noted that only one of I_x , I_y and I_z is nonzero for the single-polarisation source, *e.g.* $I_x = 0, I_y = 0$ and $I_z \neq 0$. Replacing \mathbf{r} with $(\mathbf{r}, \mathbf{r}_0)$ to represent scenario produced by the above-mentioned source located at \mathbf{r}_0 , the following equation can be obtained [113], [121],

$$\vec{\mathbf{E}}(\mathbf{r}, \mathbf{r}_0) = -j\omega\mu_0 \int_V \vec{\mathbf{G}}(\mathbf{r}, \mathbf{r}') \cdot \vec{\mathbf{J}}_0(\mathbf{r}', \mathbf{r}_0) d\mathbf{r}'. \quad (3.4)$$

In matrix form with details, the above equation is expressed as,

$$\begin{aligned}
 \begin{bmatrix} E_x(\mathbf{r}, \mathbf{r}_0) \\ E_y(\mathbf{r}, \mathbf{r}_0) \\ E_z(\mathbf{r}, \mathbf{r}_0) \end{bmatrix} &= -j\omega\mu_0 \int_V \begin{bmatrix} G_{xx}(\mathbf{r}, \mathbf{r}'), G_{xy}(\mathbf{r}, \mathbf{r}'), G_{xz}(\mathbf{r}, \mathbf{r}') \\ G_{yx}(\mathbf{r}, \mathbf{r}'), G_{yy}(\mathbf{r}, \mathbf{r}'), G_{yz}(\mathbf{r}, \mathbf{r}') \\ G_{zx}(\mathbf{r}, \mathbf{r}'), G_{zy}(\mathbf{r}, \mathbf{r}'), G_{zz}(\mathbf{r}, \mathbf{r}') \end{bmatrix} \cdot \begin{bmatrix} J_x(\mathbf{r}', \mathbf{r}_0) \\ J_y(\mathbf{r}', \mathbf{r}_0) \\ J_z(\mathbf{r}', \mathbf{r}_0) \end{bmatrix} d\mathbf{r}' \\
 \begin{bmatrix} E_x(\mathbf{r}, \mathbf{r}_0) \\ E_y(\mathbf{r}, \mathbf{r}_0) \\ E_z(\mathbf{r}, \mathbf{r}_0) \end{bmatrix} &= -j\omega\mu_0 \int_V \begin{bmatrix} J_x(\mathbf{r}', \mathbf{r}_0)G_{xx}(\mathbf{r}, \mathbf{r}') + J_y(\mathbf{r}', \mathbf{r}_0)G_{xy}(\mathbf{r}, \mathbf{r}') + J_z(\mathbf{r}', \mathbf{r}_0)G_{xz}(\mathbf{r}, \mathbf{r}') \\ J_x(\mathbf{r}', \mathbf{r}_0)G_{yx}(\mathbf{r}, \mathbf{r}') + J_y(\mathbf{r}', \mathbf{r}_0)G_{yy}(\mathbf{r}, \mathbf{r}') + J_z(\mathbf{r}', \mathbf{r}_0)G_{yz}(\mathbf{r}, \mathbf{r}') \\ J_x(\mathbf{r}', \mathbf{r}_0)G_{zx}(\mathbf{r}, \mathbf{r}') + J_y(\mathbf{r}', \mathbf{r}_0)G_{zy}(\mathbf{r}, \mathbf{r}') + J_z(\mathbf{r}', \mathbf{r}_0)G_{zz}(\mathbf{r}, \mathbf{r}') \end{bmatrix} d\mathbf{r}' \\
 \begin{bmatrix} E_x(\mathbf{r}, \mathbf{r}_0) \\ E_y(\mathbf{r}, \mathbf{r}_0) \\ E_z(\mathbf{r}, \mathbf{r}_0) \end{bmatrix} &= -j\omega\mu_0 L \begin{bmatrix} I_x G_{xx}(\mathbf{r}, \mathbf{r}_0) + I_y G_{xy}(\mathbf{r}, \mathbf{r}_0) + I_z G_{xz}(\mathbf{r}, \mathbf{r}_0) \\ I_x G_{yx}(\mathbf{r}, \mathbf{r}_0) + I_y G_{yy}(\mathbf{r}, \mathbf{r}_0) + I_z G_{yz}(\mathbf{r}, \mathbf{r}_0) \\ I_x G_{zx}(\mathbf{r}, \mathbf{r}_0) + I_y G_{zy}(\mathbf{r}, \mathbf{r}_0) + I_z G_{zz}(\mathbf{r}, \mathbf{r}_0) \end{bmatrix} .
 \end{aligned} \tag{3.5}$$

When the z -directed (or x -directed, y -directed, which means only one component of I_x , I_y and I_z is nonzero) antenna is used, the following formulation of Green's function can be obtained,

$$\vec{\mathbf{G}}(\mathbf{r}, \mathbf{r}_0) = \frac{1}{-j\omega\mu_0 L} \begin{bmatrix} \frac{1}{I_x} E_x(\mathbf{r}, \mathbf{r}_0), \frac{1}{I_y} E_x(\mathbf{r}, \mathbf{r}_0), \frac{1}{I_z} E_x(\mathbf{r}, \mathbf{r}_0) \\ \frac{1}{I_x} E_y(\mathbf{r}, \mathbf{r}_0), \frac{1}{I_y} E_y(\mathbf{r}, \mathbf{r}_0), \frac{1}{I_z} E_y(\mathbf{r}, \mathbf{r}_0) \\ \frac{1}{I_x} E_z(\mathbf{r}, \mathbf{r}_0), \frac{1}{I_y} E_z(\mathbf{r}, \mathbf{r}_0), \frac{1}{I_z} E_z(\mathbf{r}, \mathbf{r}_0) \end{bmatrix}, \tag{3.6}$$

which holds for $\forall \mathbf{r} \in V$ (note that only one column of (3.6) is nonzero). Using the principle of reciprocity [121], the relative transposed Green's function is expressed as

$$\vec{\mathbf{G}}(\mathbf{r}_0, \mathbf{r}) = \vec{\mathbf{G}}^T(\mathbf{r}, \mathbf{r}_0) = \frac{1}{-j\omega\mu_0 L} \begin{bmatrix} \frac{1}{I_x} E_x(\mathbf{r}, \mathbf{r}_0), \frac{1}{I_x} E_y(\mathbf{r}, \mathbf{r}_0), \frac{1}{I_x} E_z(\mathbf{r}, \mathbf{r}_0) \\ \frac{1}{I_y} E_x(\mathbf{r}, \mathbf{r}_0), \frac{1}{I_y} E_y(\mathbf{r}, \mathbf{r}_0), \frac{1}{I_y} E_z(\mathbf{r}, \mathbf{r}_0) \\ \frac{1}{I_z} E_x(\mathbf{r}, \mathbf{r}_0), \frac{1}{I_z} E_y(\mathbf{r}, \mathbf{r}_0), \frac{1}{I_z} E_z(\mathbf{r}, \mathbf{r}_0) \end{bmatrix}. \tag{3.7}$$

3.1. METHODOLOGY

Assuming the z -polarised source is used, (3.7) is reduced with the first two rows becoming zero as,

$$\vec{\mathbf{G}}(\mathbf{r}_0, \mathbf{r}) = \vec{\mathbf{G}}^T(\mathbf{r}, \mathbf{r}_0) = \frac{1}{-j\omega\mu_0 L} \begin{bmatrix} 0 & 0 & 0 \\ 0 & 0 & 0 \\ \frac{1}{L_z}E_x(\mathbf{r}, \mathbf{r}_0) & \frac{1}{L_z}E_y(\mathbf{r}, \mathbf{r}_0) & \frac{1}{L_z}E_z(\mathbf{r}, \mathbf{r}_0) \end{bmatrix}. \quad (3.8)$$

Therefore, the DBIM equation can be constructed and reduced as,

$$\begin{aligned} & \vec{\mathbf{E}}_s(\mathbf{r}_n, \mathbf{r}_m) \\ &= \omega^2 \mu_0 \epsilon_0 \int_V O(\mathbf{r}') \vec{\mathbf{G}}(\mathbf{r}_n, \mathbf{r}') \cdot \vec{\mathbf{E}}_b(\mathbf{r}', \mathbf{r}_m) d\mathbf{r}' \\ &= j\omega\epsilon_0 \int_V O(\mathbf{r}') \begin{bmatrix} 0 & 0 & 0 \\ 0 & 0 & 0 \\ \frac{1}{L_z}E_x(\mathbf{r}', \mathbf{r}_n) & \frac{1}{L_z}E_y(\mathbf{r}', \mathbf{r}_n) & \frac{1}{L_z}E_z(\mathbf{r}', \mathbf{r}_n) \end{bmatrix} \cdot \begin{bmatrix} E_x(\mathbf{r}', \mathbf{r}_m) \\ E_y(\mathbf{r}', \mathbf{r}_m) \\ E_z(\mathbf{r}', \mathbf{r}_m) \end{bmatrix} d\mathbf{r}' \\ &= j\omega\epsilon_0 \int_V O(\mathbf{r}') \begin{bmatrix} 0 \\ 0 \\ \frac{1}{L_z}(E_x(\mathbf{r}', \mathbf{r}_n)E_x(\mathbf{r}', \mathbf{r}_m) + E_y(\mathbf{r}', \mathbf{r}_n)E_y(\mathbf{r}', \mathbf{r}_m) + E_z(\mathbf{r}', \mathbf{r}_n)E_z(\mathbf{r}', \mathbf{r}_m)) \end{bmatrix} d\mathbf{r}'. \end{aligned} \quad (3.9)$$

For a 2-D problem with TM wave where the electric field only has z -component and the z -direction is considered as infinite, (3.9) is reduced to a scalar equation as,

$$E_s^z(\mathbf{r}_n, \mathbf{r}_m) = j\omega\epsilon_0 \int_S \frac{1}{L_z} O(\mathbf{r}') E_z(\mathbf{r}', \mathbf{r}_n) E_z(\mathbf{r}', \mathbf{r}_m) d\mathbf{r}'. \quad (3.10)$$

When the dielectric properties are considered constant over each grid, the integral part in the above equation can be discretised in a number of 2-D grids with point $\mathbf{r} \in S$ located at the centre of each grid. The following summation for each TR pair is obtained when also

assuming the field are constant over each grid with size $\Delta h \times \Delta h$,

$$E_s^z(\mathbf{r}_n, \mathbf{r}_m) = \frac{j\omega\epsilon_0(\Delta h)^2}{I_z} \sum_{\mathbf{r} \in S} O(\mathbf{r}) E_z(\mathbf{r}, \mathbf{r}_n) E_z(\mathbf{r}, \mathbf{r}_m). \quad (3.11)$$

In 3-D problems, assuming the uniform cubic voxel is used with size $\Delta h \times \Delta h \times \Delta h$, (3.9) can be written in a discrete formulation with point $\mathbf{r} \in V$ at the centre of each voxel $V_{\mathbf{r}}$ as,

$$\bar{\mathbf{E}}_s(\mathbf{r}_n, \mathbf{r}_m) = k_0^2 (\Delta h)^3 \sum_{\mathbf{r} \in V} \bar{\mathbf{G}}_b(\mathbf{r}_n, \mathbf{r}) \bar{\mathbf{E}}_b(\mathbf{r}, \mathbf{r}_m) O(\mathbf{r}), \quad (3.12)$$

where the scattered and background electric fields are vectors,

$$\bar{\mathbf{E}}_s(\mathbf{r}_n, \mathbf{r}_m) = \begin{bmatrix} E_s^x(\mathbf{r}_n, \mathbf{r}_m) \\ E_s^y(\mathbf{r}_n, \mathbf{r}_m) \\ E_s^z(\mathbf{r}_n, \mathbf{r}_m) \end{bmatrix} \text{ and } \bar{\mathbf{E}}_b(\mathbf{r}, \mathbf{r}_m) = \begin{bmatrix} E_x(\mathbf{r}, \mathbf{r}_m) \\ E_y(\mathbf{r}, \mathbf{r}_m) \\ E_z(\mathbf{r}, \mathbf{r}_m) \end{bmatrix}, \quad (3.13)$$

with E_x, E_y, E_z representing the x -, y -, z -direction fields of the electric field $\bar{\mathbf{E}}_b$ respectively, and k_0 is the free-space wavenumber.

The scattered field $\bar{\mathbf{E}}_s$ is a vector in 3-D problems, while the measurement data obtained from experiment or CST Microwave Studio only has phase and magnitude. To this end, scalar approximation of the scattered field is used as,

$$\bar{E}_s = \bar{\mathbf{E}}_s \cdot \hat{\mathbf{z}} = E_s^z. \quad (3.14)$$

In the following, E_s is used to represent E_s^z for simplification. Previous works have already shown that when the single-polarisation antenna is used, the impact of scalar approximation is trivial and negligible [53], [113], [121]–[123]. This results in further reduction of

(3.12) to a scalar equation as,

$$E_s = k_0^2(\Delta h)^3 \sum_{r \in V} [\bar{\mathbf{G}}_b(\mathbf{r}_n, \mathbf{r}) \bar{\mathbf{E}}_b(\mathbf{r}, \mathbf{r}_m) O(\mathbf{r})] \cdot \hat{\mathbf{z}}, \quad (3.15)$$

where the z -component of product in the RHS of (3.15) is computed as,

$$\bar{\mathbf{G}}_b^z(\mathbf{r}_n, \mathbf{r}) \bar{\mathbf{E}}_b(\mathbf{r}, \mathbf{r}_m) = \frac{j}{\omega_0 \mu_0 I_z L} \sum_{i=x,y,z} E_i(\mathbf{r}, \mathbf{r}_n) E_i(\mathbf{r}, \mathbf{r}_m), \quad (3.16)$$

with Green's function reduced to a vector,

$$\bar{\mathbf{G}}_b^z(\mathbf{r}_n, \mathbf{r}) = \frac{j}{\omega_0 \mu_0 I_z L} \begin{bmatrix} E_x(\mathbf{r}, \mathbf{r}_n) & E_y(\mathbf{r}, \mathbf{r}_n) & E_z(\mathbf{r}, \mathbf{r}_n) \end{bmatrix}. \quad (3.17)$$

Assuming that the cross-products of x - and y -components are negligible [113] when a z -polarised antenna is used, the Green's function can be further simplified to account only for the z -directed components as,

$$G_b(\mathbf{r}_n, \mathbf{r}) = \frac{j}{\omega_0 \mu_0 I_z L} E_z(\mathbf{r}, \mathbf{r}_n). \quad (3.18)$$

The simplification of assuming a z -polarised source is only done by the proposed inversion imaging algorithm, and is not used to generate the data in CST, which models the exact antenna used in experiments. Moreover, the assumption that only the z -component of the Green's function is non-zero is employed only in the inversion of the linear matrix at each DBIM iteration. The 3-D FDTD forward solver used by the imaging algorithm calculates all three field components as usual. This allows comparing the z -only approximation of the Green's function with the vector formulation in (3.17), which is done in Chapter 5.

3.1.2 FEM-DBIM approach

Considering using FEM as the forward solver at each DBIM iteration, the FEM solution is used to construct the linear system $\mathbf{Ax} = \mathbf{b}$. For each TR pair $(\mathbf{r}_i, \mathbf{r}_j)$ discretising (3.10) by using the same elements as the FEM triangles in the reconstruction domain S , taken as a subdomain of the total FEM computational domain S_T , the DBIM equation is rewritten as,

$$E_s(\mathbf{r}_i, \mathbf{r}_j) = \frac{j\omega\epsilon_0}{I_z} \sum_{k=1}^K O(\mathbf{r}_k) \iint_{S^k} E_b(\mathbf{r}_i, \mathbf{r}') E_b(\mathbf{r}', \mathbf{r}_j) dS, \quad (3.19)$$

where $O(\mathbf{r}_k)$ is the dielectric contrast of the k -th element. For the traditional approach, the electric fields are assumed to be constant over the whole triangular element, resulting in the following discretised form,

$$E_s(\mathbf{r}_i, \mathbf{r}_j) = \frac{j\omega\epsilon_0}{I_z} \sum_{k=1}^K O(\mathbf{r}_k) S^k E_b(\mathbf{r}_i, \mathbf{r}_k) E_b(\mathbf{r}_k, \mathbf{r}_j), \quad (3.20)$$

where S^k is the area of the k -th element, \mathbf{r}_k is the centre of the triangle where the field is to be interpolated by using (2.39). However, the computational of the integral part is not straightforward, especially in FEM, where geometrical transformations are usually involved, and can be time-consuming and also result in loss of accuracy.

Unlike the typical approach in (3.20), this work proposes to take advantage of the fact that correlations of basis functions have already been integrated inside each element through well-established quadrature rules in the FEM framework [124]. Thus, the information related to the integration of multiplication of fields is available seamlessly from the forward solution, without the need to consider them constant and avoiding interpolation.

To that effect, the following equation holds by using (2.39) and (2.41) in (3.19),

$$\iint_{S^k} E_b(\mathbf{r}_i, \mathbf{r}') E_b(\mathbf{r}', \mathbf{r}_j) dS = \iint_{S^k} \left(\sum_{p=1}^{p^k} \phi_p^k(\mathbf{r}') e_{p,i}^k \right) \left(\sum_{q=1}^{p^k} \phi_q^k(\mathbf{r}') e_{q,j}^k \right) dS = (\mathbf{e}_i^k)^T \mathbf{M}^k \mathbf{e}_j^k, \quad (3.21)$$

where \mathbf{e}_i^k is a vector consisting of the basis functions $e_{p,i}^k$ inside each element.

By direct inspection of (3.19) and (3.21), it can easily be seen that every element from a TR pair in row $m = (i, j)$ and column n of matrix \mathbf{A} in the linear system of each iteration of the DBIM can be straightforwardly calculated from the already available computed FEM matrices and solutions as

$$\{\mathbf{A}\}_{m,n} = \frac{j\omega\epsilon_0}{I_z} (\mathbf{e}_i^n)^T \mathbf{M}^n \mathbf{e}_j^n, \quad (3.22)$$

while the scattered fields at the m -th row can be calculated as

$$\{\mathbf{b}\}_m = \tilde{E}(\mathbf{r}_i, \mathbf{r}_j) - \{\mathbf{E}\}_{p(j),i}, \quad (3.23)$$

where $p(j)$ stands for the global numbering in the FEM solution of the d.o.f. corresponding to point receiver j , which is located at a node for ease of computation of matrix \mathbf{b} , and \tilde{E} is the field obtained from measurements or a reference simulation.

The implementation of this proposed FEM-DBIM approach is based on the open-source FEniCS high-level Python interface [125]. As an interpreted language, it provides additional flexibility and ease of coding without losing efficiency in the critical FEM steps (assembly, solution). Moreover, it allows seamless access to the matrices and information required for the proposed inverse-problem matrix building technique.

For dispersive materials, the complex-valued linear system $\mathbf{Ax} = \mathbf{b}$ is usually cast in real-valued form with regard to real-valued parameters (i.e. Debye parameters, conduc-

tivity, etc.) in order to use powerful real-valued inverse problem solvers. In the FEM-DBIM approach, the common definition of the relative permittivity is used as $\varepsilon_r(\mathbf{r}) = \varepsilon'_r(\mathbf{r}) - j\varepsilon''_r(\mathbf{r})$, with $\varepsilon'_r \geq 1, \varepsilon''_r \geq 0$, and the contrast can be identically expressed as $O(\mathbf{r}) = O'(\mathbf{r}) - jO''(\mathbf{r})$ to yield,

$$\hat{\mathbf{A}}\hat{\mathbf{x}} = \hat{\mathbf{b}} \Leftrightarrow \begin{bmatrix} \mathbf{A}_{\Re} & \mathbf{A}_{\Im} \\ \mathbf{A}_{\Im} & -\mathbf{A}_{\Re} \end{bmatrix} \begin{bmatrix} \mathbf{O}' \\ \mathbf{O}'' \end{bmatrix} = \begin{bmatrix} \mathbf{b}_{\Re} \\ \mathbf{b}_{\Im} \end{bmatrix}, \quad (3.24)$$

where the real and imaginary parts of \mathbf{A} , \mathbf{O} and \mathbf{b} are separated.

The dimension of the new inverse problem matrix $\hat{\mathbf{A}}$, contrast $\hat{\mathbf{x}}$ and scattered fields $\hat{\mathbf{b}}$ are doubled as $2M \times 2N$, $2N \times 1$ and $2M \times 1$ respectively. By inspection, it is straightforward to see $\mathbf{b}_{\Re} = \Re\{\mathbf{b}\}$ and $\mathbf{b}_{\Im} = \Im\{\mathbf{b}\}$. The same would apply for the construction of the new real-valued matrix $\hat{\mathbf{A}}$ from the complex-valued matrix \mathbf{A} . However, for implementation purposes, the FEM approximation in (2.39) can be directly cast in real-valued form by doubling the function-space and the number of unknowns as

$$E^k(\mathbf{r}) = \sum_{p=1}^{P^k} \phi_{\Re,p}^k(\mathbf{r}) e_{\Re,p}^k + j \sum_{p=1}^{P^k} \phi_{\Im,p}^k(\mathbf{r}) e_{\Im,p}^k. \quad (3.25)$$

Derivation of the local matrices of the FEM involved in this case is similar to (2.41), but more tedious. The direct construction of the real-valued inverse problem matrix is again straightforward for this real-valued formulation of the proposed FEM-based DBIM approach, as the element for the m th row (coming from the i, j TR pair) and the n th column of the involved matrices in (3.24) can be readily computed as [124],

$$\begin{bmatrix} \{\mathbf{A}_{\Re}\}_{mn} \\ \{\mathbf{A}_{\Im}\}_{mn} \end{bmatrix} = \frac{\omega \varepsilon_0}{I_z} \begin{bmatrix} \mathbf{e}_{\Re,i}^n & \mathbf{e}_{\Im,i}^n \\ -\mathbf{e}_{\Im,i}^n & \mathbf{e}_{\Re,i}^n \end{bmatrix}^T \begin{bmatrix} -\mathbf{M}_{\Im}^n & -\mathbf{M}_{\Re}^n \\ \mathbf{M}_{\Re}^n & -\mathbf{M}_{\Im}^n \end{bmatrix} \begin{bmatrix} \mathbf{e}_{\Re,j}^n \\ \mathbf{e}_{\Im,j}^n \end{bmatrix}, \quad (3.26)$$

where local matrices $\mathbf{M}_{\mathfrak{R}}^n$ and $\mathbf{M}_{\mathfrak{S}}^n$ are already available from the FEM procedure as,

$$\begin{aligned}\{\mathbf{M}_{\mathfrak{R}}^n\}_{pq} &= \iint_{S^n} \left(\phi_{\mathfrak{R},p}^n(\mathbf{r}') \phi_{\mathfrak{R},q}^n(\mathbf{r}') - \phi_{\mathfrak{S},p}^n(\mathbf{r}') \phi_{\mathfrak{S},q}^n(\mathbf{r}') \right) dS, \\ \{\mathbf{M}_{\mathfrak{S}}^n\}_{pq} &= \iint_{S^n} \left(\phi_{\mathfrak{R},p}^n(\mathbf{r}') \phi_{\mathfrak{S},q}^n(\mathbf{r}') + \phi_{\mathfrak{S},p}^n(\mathbf{r}') \phi_{\mathfrak{R},q}^n(\mathbf{r}') \right) dS.\end{aligned}\quad (3.27)$$

Finally, the real-valued linear system is solved by iterative solvers such as CGLS or ISTAs.

3.1.3 FDTD-DBIM approach

Similar to the FEM-DBIM approach, when the single-pole Debye model is used in FDTD, to best use the powerful linear solvers and avoid complex number computations, the linear system for DBIM can be expressed in real and imaginary parts as the following procedure,

$$\begin{aligned}(\mathbf{A}_{\mathfrak{R}} + j\mathbf{A}_{\mathfrak{S}})(\mathbf{O}_{\varepsilon_{\infty}} + \frac{\mathbf{O}_{\Delta\varepsilon}}{1 + j\omega\tau} + \frac{\mathbf{O}_{\sigma_s}}{j\omega\varepsilon_0}) \\ = (\mathbf{A}_{\mathfrak{R}} + j\mathbf{A}_{\mathfrak{S}})\mathbf{O}_{\varepsilon_{\infty}} + (\mathbf{A}_{\mathfrak{R}} + j\mathbf{A}_{\mathfrak{S}})\frac{\mathbf{O}_{\Delta\varepsilon}}{1 + j\omega\tau} + (\mathbf{A}_{\mathfrak{R}} + j\mathbf{A}_{\mathfrak{S}})\frac{\mathbf{O}_{\sigma_s}}{j\omega\varepsilon_0} \\ = (\mathbf{A}_{\mathfrak{R}} + j\mathbf{A}_{\mathfrak{S}})\mathbf{O}_{\varepsilon_{\infty}} + \left(\frac{\mathbf{A}_{\mathfrak{R}} + \omega\tau\mathbf{A}_{\mathfrak{S}}}{1 + \omega^2\tau^2} + j\frac{\mathbf{A}_{\mathfrak{S}} - \omega\tau\mathbf{A}_{\mathfrak{R}}}{1 + \omega^2\tau^2}\right)\mathbf{O}_{\Delta\varepsilon} + \left(\frac{\mathbf{A}_{\mathfrak{S}}}{\omega\varepsilon_0} - j\frac{\mathbf{A}_{\mathfrak{R}}}{j\omega\varepsilon_0}\right)\mathbf{O}_{\sigma_s},\end{aligned}\quad (3.28)$$

where the scattering matrix \mathbf{A} is represented by two parts as $\mathbf{A} = \mathbf{A}_{\mathfrak{R}} + j\mathbf{A}_{\mathfrak{S}}$, and the contrast \mathbf{O} consists of three components of the Debye parameters. The following real-valued equation is obtained as,

$$\begin{aligned}\mathbf{b}_{\mathfrak{R}} + j\mathbf{b}_{\mathfrak{S}} \\ = (\mathbf{A}_{\mathfrak{R}} + j\mathbf{A}_{\mathfrak{S}})\mathbf{O}_{\varepsilon_{\infty}} + \left(\frac{\mathbf{A}_{\mathfrak{R}} + \omega\tau\mathbf{A}_{\mathfrak{S}}}{1 + \omega^2\tau^2} + j\frac{\mathbf{A}_{\mathfrak{S}} - \omega\tau\mathbf{A}_{\mathfrak{R}}}{1 + \omega^2\tau^2}\right)\mathbf{O}_{\Delta\varepsilon} + \left(\frac{\mathbf{A}_{\mathfrak{S}}}{\omega\varepsilon_0} - j\frac{\mathbf{A}_{\mathfrak{R}}}{j\omega\varepsilon_0}\right)\mathbf{O}_{\sigma_s},\end{aligned}\quad (3.29)$$

leading to the following linear system for a problem with M TR pairs and N voxels inside the reconstruction region.

$$\begin{bmatrix} \mathbf{b}_{\mathfrak{R}}(1) \\ \mathbf{b}_{\mathfrak{S}}(1) \\ \mathbf{b}_{\mathfrak{R}}(2) \\ \mathbf{b}_{\mathfrak{S}}(2) \\ \dots \\ \mathbf{b}_{\mathfrak{R}}(M) \\ \mathbf{b}_{\mathfrak{S}}(M) \end{bmatrix} = \begin{bmatrix} \bar{\mathbf{A}}_{\mathfrak{R}}^{\varepsilon_{\infty}}(1), \bar{\mathbf{A}}_{\mathfrak{R}}^{\Delta\varepsilon}(1), \bar{\mathbf{A}}_{\mathfrak{R}}^{\sigma_s}(1) \\ \bar{\mathbf{A}}_{\mathfrak{S}}^{\varepsilon_{\infty}}(1), \bar{\mathbf{A}}_{\mathfrak{S}}^{\Delta\varepsilon}(1), \bar{\mathbf{A}}_{\mathfrak{S}}^{\sigma_s}(1) \\ \bar{\mathbf{A}}_{\mathfrak{R}}^{\varepsilon_{\infty}}(2), \bar{\mathbf{A}}_{\mathfrak{R}}^{\Delta\varepsilon}(2), \bar{\mathbf{A}}_{\mathfrak{R}}^{\sigma_s}(2) \\ \bar{\mathbf{A}}_{\mathfrak{S}}^{\varepsilon_{\infty}}(2), \bar{\mathbf{A}}_{\mathfrak{S}}^{\Delta\varepsilon}(2), \bar{\mathbf{A}}_{\mathfrak{S}}^{\sigma_s}(2) \\ \dots, \dots, \dots \\ \bar{\mathbf{A}}_{\mathfrak{R}}^{\varepsilon_{\infty}}(M), \bar{\mathbf{A}}_{\mathfrak{R}}^{\Delta\varepsilon}(M), \bar{\mathbf{A}}_{\mathfrak{R}}^{\sigma_s}(M) \\ \bar{\mathbf{A}}_{\mathfrak{S}}^{\varepsilon_{\infty}}(M), \bar{\mathbf{A}}_{\mathfrak{S}}^{\Delta\varepsilon}(M), \bar{\mathbf{A}}_{\mathfrak{S}}^{\sigma_s}(M) \end{bmatrix} \begin{bmatrix} \mathbf{O}_{\varepsilon_{\infty}}(1) \\ \mathbf{O}_{\varepsilon_{\infty}}(2) \\ \dots \\ \mathbf{O}_{\varepsilon_{\infty}}(N) \\ \mathbf{O}_{\Delta\varepsilon}(1) \\ \mathbf{O}_{\Delta\varepsilon}(2) \\ \dots \\ \mathbf{O}_{\Delta\varepsilon}(N) \\ \mathbf{O}_{\sigma_s}(1) \\ \mathbf{O}_{\sigma_s}(2) \\ \dots \\ \mathbf{O}_{\sigma_s}(N) \end{bmatrix}, \quad (3.30)$$

where the left-hand side (LHS) is a $2M \times 1$ vector, the RHS is the multiplication of a $2M \times 3N$ matrix and a $3N \times 1$ vector, and the resulting matrix elements of $\bar{\mathbf{A}}$ are calculated as,

$$\bar{\mathbf{A}}_{\mathfrak{R}}^{\varepsilon_{\infty}} = \mathbf{A}_{\mathfrak{R}}, \bar{\mathbf{A}}_{\mathfrak{S}}^{\varepsilon_{\infty}} = \mathbf{A}_{\mathfrak{S}}, \bar{\mathbf{A}}_{\mathfrak{R}}^{\Delta\varepsilon} = \frac{\mathbf{A}_{\mathfrak{R}} + \omega\tau\mathbf{A}_{\mathfrak{S}}}{1 + \omega^2\tau^2}, \bar{\mathbf{A}}_{\mathfrak{S}}^{\Delta\varepsilon} = \frac{\mathbf{A}_{\mathfrak{S}} - \omega\tau\mathbf{A}_{\mathfrak{R}}}{1 + \omega^2\tau^2}, \bar{\mathbf{A}}_{\mathfrak{R}}^{\sigma_s} = \frac{\mathbf{A}_{\mathfrak{S}}}{\omega\varepsilon_0}, \bar{\mathbf{A}}_{\mathfrak{S}}^{\sigma_s} = \frac{-\mathbf{A}_{\mathfrak{R}}}{\omega\varepsilon_0}. \quad (3.31)$$

When nondispersive materials (or real and imaginary parts of the permittivity) are considered, the above formulation is also valid by removing the $\Delta\varepsilon$ part in the scattering matrix \mathbf{A} and contrast \mathbf{x} , leading to a reduced linear system.

3.1.4 Fast iterative shrinkage/thresholding algorithm

FISTA is another type of ISTA-type algorithms that can be used to solve the linear system arising in ISPs. FISTA [126] uses Nesterov accelerated momentum [127] and reduced number of parameters than the TwIST algorithm [117]. Similarly, a minimisation problem, including a regularisation term, is considered by FISTA as the following steps when l_1 norm is chosen,

$$F(\mathbf{x}) = \frac{1}{2} \|\mathbf{Ax} - \mathbf{b}\|_2^2 + \lambda \|\mathbf{x}\|_1, \quad (3.32)$$

where λ is a regularisation parameter. The structure of FISTA is constructed as [126],

$$\begin{aligned} \mathbf{x}_k &= p_{L_k}(\mathbf{y}_k) = \Psi \left(\mathbf{y}_k - \frac{1}{L_k} \mathbf{A}^T (\mathbf{A} \mathbf{y}_k - \mathbf{b}) \right), \\ \mathbf{y}_{k+1} &= \mathbf{x}_k + \frac{t_k - 1}{t_{k+1}} (\mathbf{x}_k - \mathbf{x}_{k-1}), \end{aligned} \quad (3.33)$$

where $t_0 = 1$, $t_{k+1} = \frac{1 + \sqrt{1 + 4t_k^2}}{2}$, Ψ is the soft thresholding function $\Psi(x) = \text{sign}(x)|x - \lambda|$, \mathbf{y}_k is the solution at the k -th iteration. L_k is a non-negative parameter which is selected based on the following strategy: Find the smallest non-negative integers i_k with $L_k = \eta^{i_k} L_{k-1}$ and $L_0 = 1$, such that

$$F(p_{L_k}(\mathbf{y}_k)) \leq Q_{L_k}((p_{L_k}(\mathbf{y}_k), \mathbf{y}_k), \quad (3.34)$$

where $\eta > 1$ and

$$Q_L(\mathbf{x}, \mathbf{y}) = \frac{1}{2} \|\mathbf{Ay} - \mathbf{b}\|_2^2 + \langle \mathbf{x} - \mathbf{y}, \mathbf{A}^T \mathbf{Ay} - \mathbf{b} \rangle + \frac{1}{2} \|\mathbf{x} - \mathbf{y}\|_2^2 + \lambda \|\mathbf{x}\|_1. \quad (3.35)$$

The computational complexity for FISTA is $O(kMN)$ with a higher-order convergence rate $O(\frac{1}{k^2})$ compared with the traditional GD-type algorithm. The improvement is caused

by the use of the accelerated momentum t_k , which also reduces the chance of getting stuck into a local minimum when combined with a regularisation term [128]. As a result of this implementation, FISTA does not require pre-setting the parameters α and β in (2.73), which are related to the eigenvalues $A^T A$. For 3-D problems, the eigenvalues of matrix A are usually not computable due to limited computational memory. This allows FISTA to be more robust, efficient, and easier to optimise the thresholding approach than the TwIST algorithm.

This implementation selects the initial value of \mathbf{x} to be all 0 and the regularisation parameter as $\lambda = \delta \|\mathbf{A}^T \mathbf{b}\|_\infty$, where δ is a factor with $0 < \delta < 1$. The stopping criterion is based on the relative error between current $F(\mathbf{x}_k)$ and previous $F(\mathbf{x}_{k-1})$, defined as

$$e_{\text{opt}} = \frac{|F(\mathbf{x}_k) - F(\mathbf{x}_{k-1})|}{F(\mathbf{x}_{k-1})}. \quad (3.36)$$

FISTA stops when the relative error e_{opt} becomes smaller than a preset tolerance value, usually chosen between 1e-2 and 1e-4.

The tolerance value has a significant impact on the quality of the recovered images using the DBIM approach. If the tolerance is too small, the algorithm can produce a false reconstruction image due to over-fitting. If the tolerance is too large, the number of iterations may not be enough to ensure that the algorithm produces an accurate image.

3.1.5 Data calibration

The data produced by CST or measured from the experiment are different from the data obtained by the simulations due to discrepancy. Although there are no experimental factors for CST simulations, the data produced by CST and FEM/FDTD need to be calibrated, as the CST simulation models the structure of the scenario realistically, while the

FEM/FDTD simulation uses simplified point source antenna structure, modified geometry, *etc.* For the measured data from the experiment, the modelling discrepancy also exists. Moreover, reflections from the experimental system, such as cables, connectors, and tanks, are not trivial, and noise from the experimental environment also has an impact on the data. Therefore, a calibration procedure is needed to reduce the discrepancy, which assumes that the ratio between two sets of data is equivalent, including two scenarios, the background case noted as no target (NT), and the case to be investigated, noted as with target (WT).

$$\frac{E_{\text{NT},\text{sim}}}{E_{\text{WT},\text{sim}}} = \frac{E_{\text{NT},\text{meas}}}{E_{\text{WT},\text{meas}}}, \quad (3.37)$$

where the subscript “sim” represents the data obtained by simulation of FDTD or FEM and the subscript “meas” represents the data measured by the experimental system or the data produced by CST. Thus, with the measured data, the scattered field can be calculated as,

$$E_s = E_{\text{WT},\text{sim}} = \frac{E_{\text{NT},\text{sim}}}{E_{\text{NT},\text{meas}}} E_{\text{WT},\text{meas}}, \quad (3.38)$$

which is used as the scattered field for the reconstruction algorithm.

3.1.6 Multiple frequency approach

The data obtained from the measurement usually cover a range of frequencies, and the single-frequency data may not be sufficient to produce expected reconstruction results due to the nonlinearity of the problem. Multiple frequency approaches can be used to enhance reconstruction performance with increased knowledge, thus reducing nonlinearity.

There are mainly two approaches for multiple frequency MWI. The first approach is to combine multiple frequency information simultaneously in DBIM [118], where the

linear system is built as the following form for N_f frequencies,

$$\begin{bmatrix} \bar{\mathbf{b}}(\omega_1) \\ \dots \\ \bar{\mathbf{b}}(\omega_{N_f}) \end{bmatrix} = \begin{bmatrix} \bar{\mathbf{A}}(\omega_1) \\ \dots \\ \bar{\mathbf{A}}(\omega_{N_f}) \end{bmatrix} \begin{bmatrix} \mathbf{O}_{\varepsilon_\infty} \\ \mathbf{O}_{\Delta\varepsilon} \\ \mathbf{O}_{\sigma_s} \end{bmatrix}. \quad (3.39)$$

As dispersion exists for multiple frequencies, the single-pole Debye model can be used to estimate the parameters. This approach solves a linear system with multiple data. The computational time remains the same as the single frequency approach when using the FDTD method, since the multiple frequency data can be obtained by the Fourier transform (FT) of the time domain data. However, the frequencies and algorithm parameters need to be carefully selected to achieve a reliable solution due to the increased non-linearity.

The second approach is based on frequency hopping [129], which performs single frequency reconstructions successively from low to high frequencies. The use of lower frequencies in the initial inversion stages reduces the nonlinearity of the problem, which could prepare a better initial guess for reconstructions at higher frequencies. However, the approach is computationally expensive for a DBIM algorithm, as each of the frequencies needs to be performed for a number of iterations, and the computational time for N frequencies is N times of the single frequency approach. It may be biased toward the solutions provided by low frequencies [130].

3.2 Analysis of the DBIM-FISTA algorithm

The DBIM-FISTA algorithm is an iterative solver with several parameters that influence the reconstruction result and can be adjusted, including the number of iterations, the initial guess of the background profile, FISTA parameters, and constraints to limit the obtained contrast. By optimising these parameters, the reconstruction results can be improved.

3.2. ANALYSIS OF THE DBIM-FISTA ALGORITHM

The parameter used in the DBIM-FISTA algorithm can be chosen based on the following.

- Number of DBIM iterations: Too small or large number of DBIM iterations can cause a failed reconstruction. A small number of DBIM iterations may not guarantee the convergence of the problem. As the ISP is ill-posed, a large number of DBIM iterations may cause the solution to converge to an unexpected local minimum. According to [131], 15-20 iterations are enough to obtain a good reconstruction result. Usually after this number of iterations, the reconstruction images will not change much, and only the reconstruction values will increase slightly depending on the number of iterations.
- Initial guess: The background scenario is needed for DBIM to perform the forward solver, and certain prior information must be known. A false background startup can also cause failed reconstruction results. The typical background profile is selected as the average value of materials or a homogeneous background material, and an empty background can increase the difficulty of reconstruction. For the Debye parameters used in FDTD, the Debye values are obtained from curving fitting the used permittivity values from the experiment or library.
- FISTA parameters: FISTA parameters include the maximum number of iterations, tolerance, and thresholding parameter. The max number of iterations is a hard constraint to limit the number of iterations, which are usually chosen to be less than several hundred, such as 200 or 300. The tolerance influences the number of iterations, and FISTA stops when the tolerance value is reached. Tolerance is selected according to the specific problem. For highly nonlinear problems, the tolerance should be chosen to a more accurate value (smaller) to ensure convergence. The

thresholding parameter is used to denoise the obtained solution. However, a large thresholding parameter may over-reduce the solution and cause small reconstruction contrast values.

- Constraints: Limitation of the range of values can be imposed to ensure that the reconstructed values are in a reasonable range. Physically, the real part of the permittivity should be larger than 1, and the conductivity should be larger than 0. In practice, certain values can be set if a prior estimation of the model values is known.

3.3 Numerical and experimental models

Numerical and experimental models are used to validate and evaluate the performance of the proposed MWI algorithm, including basic models such as cylindrical models and complex models such as breast and head phantoms. For complex models, this thesis mainly focuses on the head phantoms, as the reconstruction of the breast phantoms is already presented in [118] with the TwIST algorithm. In this thesis, only one of the numerical breast phantoms is used in the 2-D case to compare the performance of TwIST and FISTA, which is shown later in Section 4.4.2.2. The numerical head phantoms used in this work include the SAM model [132] and an anatomically complicated model, *i.e.* the Zubal model [133].

To emulate the measurement data, the original models are imported into CST or FDTD and converted to a suitable format. In CST simulations, the S-parameters of the full-wave 3-D interaction of the antenna array with the phantom are produced, similar to the procedure of the experiment. The obtained S-parameters are calibrated with the simulation fields to perform reconstructions.

The models are usually placed in a homogeneous background such as air or coupling liquid. Coupling liquid is usually used instead of air to reduce the influence of reflections

and noise caused by the experimental environment. The coupling liquid used in this work is glycerol (90%)–water (10%) mixture to balance signal loss and penetration depth and to improve impedance matching between medium and boundary materials that usually have low permittivity. Moreover, this medium is used to develop the experimental prototype, and the antennas of the experimental system have been designed to operate inside this medium [63], [134]. The permittivity of glycerol (90%)–water (10%) mixture is $\epsilon_r \approx 15.9 - 14.2j$ at 1.0 GHz. The Debye parameters are $\epsilon_\infty = 6.566$, $\Delta\epsilon = 16.86$ and $\sigma_s = 0.3231$ and the relaxation time τ is fixed as 0.14288 ns for all materials used in FDTD.

The number of antennas required for a 2-D MWI problem has been defined in [135] using the approximation,

$$m \approx 2k_0\rho_{\text{rec}}, \quad (3.40)$$

where ρ_{rec} is the radius of the investigated region, while for 3-D problems the required number is slightly larger. This requirement may be difficult to satisfy in practice due to experimental limitations; for example, the experimental setup uses eight antennas hosted by an eight-port VNA system, and the same setup is used for each antenna ring in the CST scenarios. The antennas are modelled as point sources in this thesis, and the received signals by the antennas are normalised with respect to the source.

3.3.1 Cylindrical models

Basic validation models for the proposed algorithm comprise cylindrical targets immersed in air or a coupling liquid such as glycerol (90%)–water (10%) mixture. Strong scatterer targets are usually made of water, blood, *etc.*, which have a high contrast compared to immersion. The configuration of the system in CST is shown in Fig. 3.1, which resembles the configuration of the experimental system. Two long cylindrical tubes are filled with pure water as targets and placed inside the inner tank. Both tanks are made of plastic and

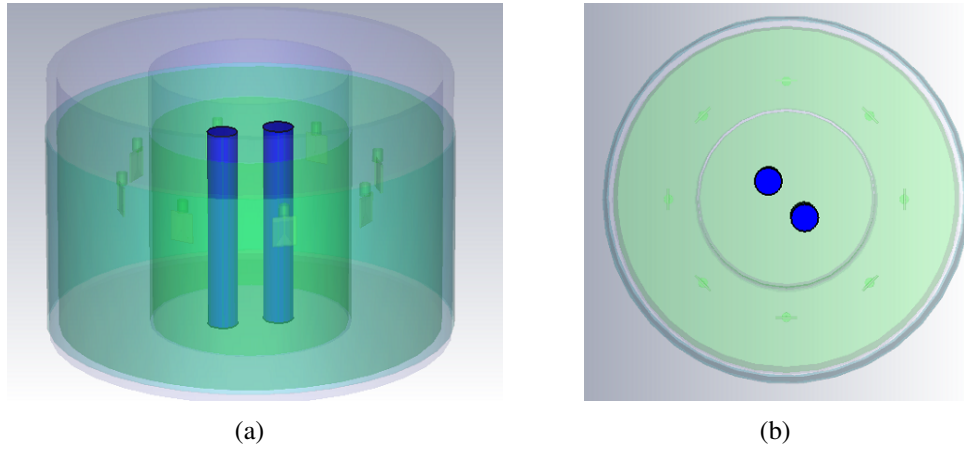


Figure 3.1: Perspective and top views of the CST models: (a) perspective view, (b) top view.

are filled with coupling liquid. The antenna array consisting of eight antennas is placed between the inner tank and the outer tank at a relatively middle height to avoid unexpected reflections from the top air-background interface. Absorbing materials can be placed at the outermost layer of the outer tank to absorb outgoing waves.

This type of scenario is also suitable for 2-D algorithms, as it can be seen as an infinite cylinder, and there is no vertical variant of the materials. The 2-D cross-sectional plane cut from the 3-D model resembles the 2-D simulation scenario.

3.3.2 SAM model

A widely used standard head model used in MWI is the SAM model from IEEE Std [132], of which the size was based on selected dimensions from the much larger anthropometric database of 1774 US Army males. The 3-D geometry, the top view of the SAM model imported into CST, and the cross-sectional geometry are shown in Fig. 3.2. The head model has two layers, including the bone layer and the brain layer. Material properties are set using the values from the CST library. The head is placed in air and surrounded by a circular headband filled with 90% glycerol-water mixture, and eight antennas with

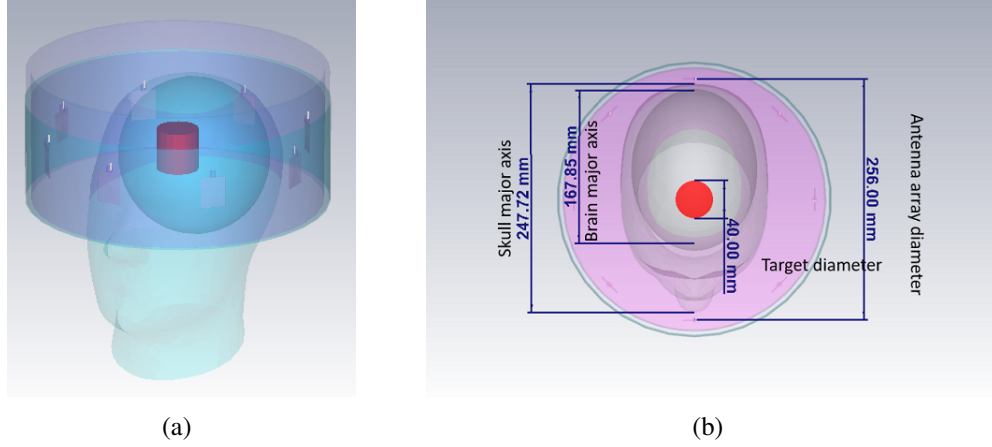


Figure 3.2: CST head model: (a) schematic of the head model, (b) top view of the head model.

radius $\rho_{\text{ant}} = 128$ mm are placed in a circle. Absorbing materials are used at the outermost layer of the headband to avoid reflections from the interface. A blood target with radius $\rho_{\text{tg}} = 20$ mm and height $h_{\text{tg}} = 40$ mm is inserted into the model. This model is used to test the 2-D reconstructions with the FDTD-based DBIM approach in Chapter 4.

3.3.3 Zubal head phantom

The original MRI-derived high-resolution Zubal head phantom [133] is a voxel-based anthropomorphic phantom and comprises $256 \times 256 \times 128$ voxels with a size of $1.1 \text{ mm} \times 1.1 \text{ mm} \times 1.4 \text{ mm}$. The Zubal model has a high resolution of human anatomy and can be used as a phantom suitable for many computer-based modelling and simulation validation.

To obtain numerical measurement data, it is imported into CST to perform realistic simulations. As it is impractical to model all the materials, the original Zubal head phantom is transformed into an eight-material model to reduce complexity. The 3-D structure of the Zubal head phantoms in CST is shown in Figure 3.3. The model in FDTD simulation is resized to fit the used FDTD grid of 2 mm for each side. For the 2-D cases, a slice

3.3. NUMERICAL AND EXPERIMENTAL MODELS

of the Zubal head phantom inside the brain is used in FDTD as shown in Figure 3.3(d), which is cut from the 3-D model.

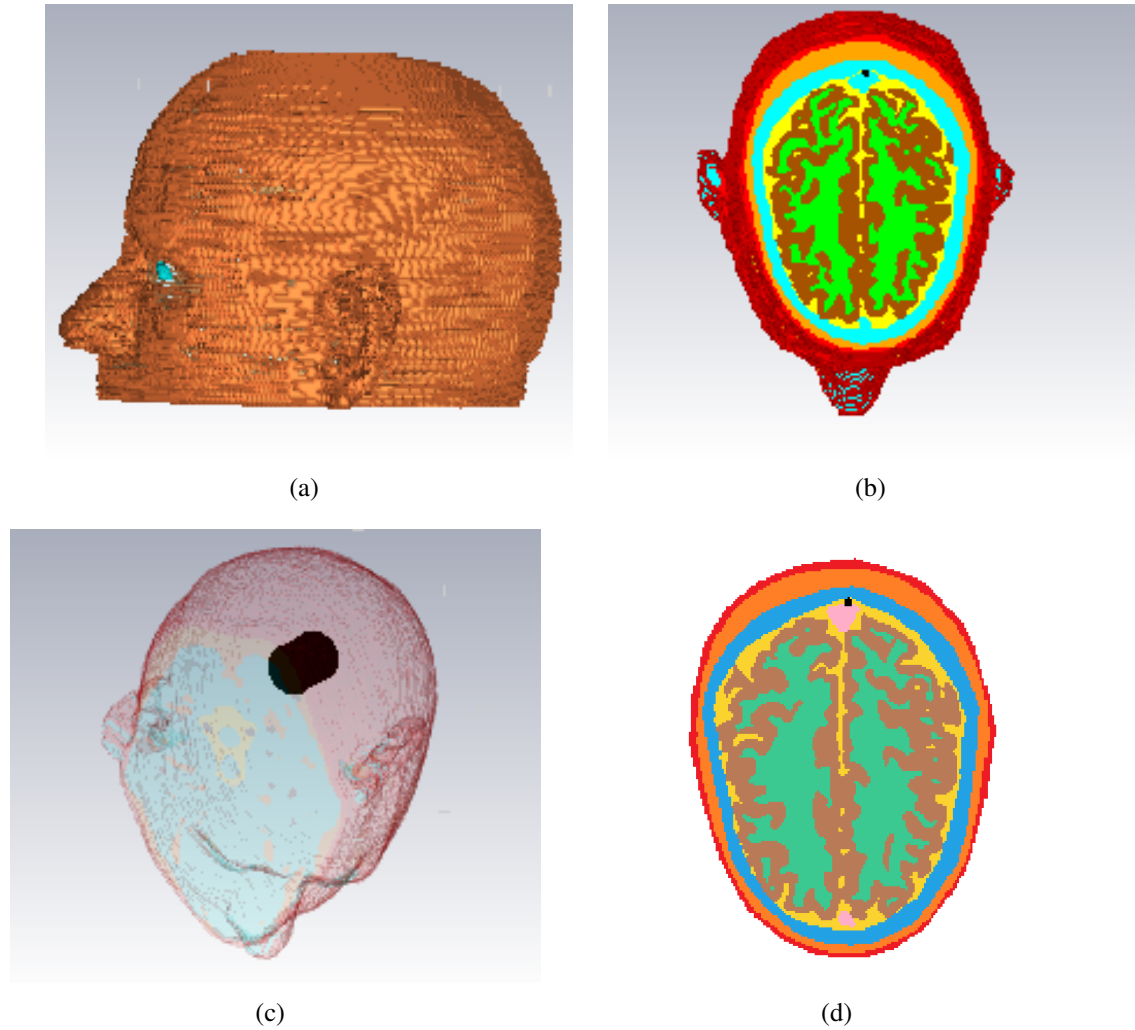


Figure 3.3: Views of the Zubal phantom in CST: (a) 3-D side-view, (b) cross-sectional top-down view, (c) 3-D view with blood target, (d) cross-sectional slice used in 2-D experiments (93th slice of the original model, where the centre of the target is placed).

The permittivity of the materials used in CST is obtained from the IT'IS foundation database [37]. This dataset is also used to develop single-pole Debye models for the FDTD code by curve fitting. The model includes eight layers with tissue types, colour codes, and respective Debye parameters (for the FDTD models) shown in Table 3.1. As

3.3. NUMERICAL AND EXPERIMENTAL MODELS

these two approaches are not identical, there are discrepancies between the CST and FDTD Debye models. The head models are surrounded by glycerol (90%)–water (10%) mixture if not specified. A blood target is inserted into the brain centred at the 93th slice of the Zubal head phantom. The details of different scenarios are discussed later in Chapter 4 and Chapter 5.

Table 3.1: Debye parameters for the Zubal head phantom.

Tissue type and color in Fig 3.3(d)	ϵ_{∞}	$\Delta\epsilon$	$\sigma_s(\text{S/m})$
skin (red)	37.65	11.36	0.62
fat (orange)	8.61	2.92	0.08
bone (blue)	8.48	4.38	0.08
white matter (green)	35.89	6.73	0.45
gray matter (brown)	40.03	14.47	0.72
blood (black)	44.67	18.02	1.32
CSF (yellow)	66.08	4.61	2.34
dura (pink)	39.89	6.00	0.85

3.3.4 Experimental system and brain phantom

The experimental system includes eight ports embedded in the Keysight M9019A PXIe Chassis connected to a desktop, shown in Fig. 3.4. The details of the experimental system can be found in [63]. An experimental brain phantom shown in Fig. 3.5 is made to validate the proposed FDTD-based DBIM approach with the process of making the phantom shown in Fig. 3.6 [63]. The phantom is made of a 3-D-printed plastic mould with a size of 17 cm \times 12 cm \times 8 cm. In the experiments, it is filled with an “average brain tissue” material with $\epsilon_r \approx 41.6 - 5.9j$ at 1.0 GHz (in the middle part of the brain). The permittivity of brain tissue differs at different positions, *i.e.* the permittivity near the different surface, in the inner parts or near the bottom, has different values [63]. The values are smaller near the surface and larger inside the phantom. The brain phantom

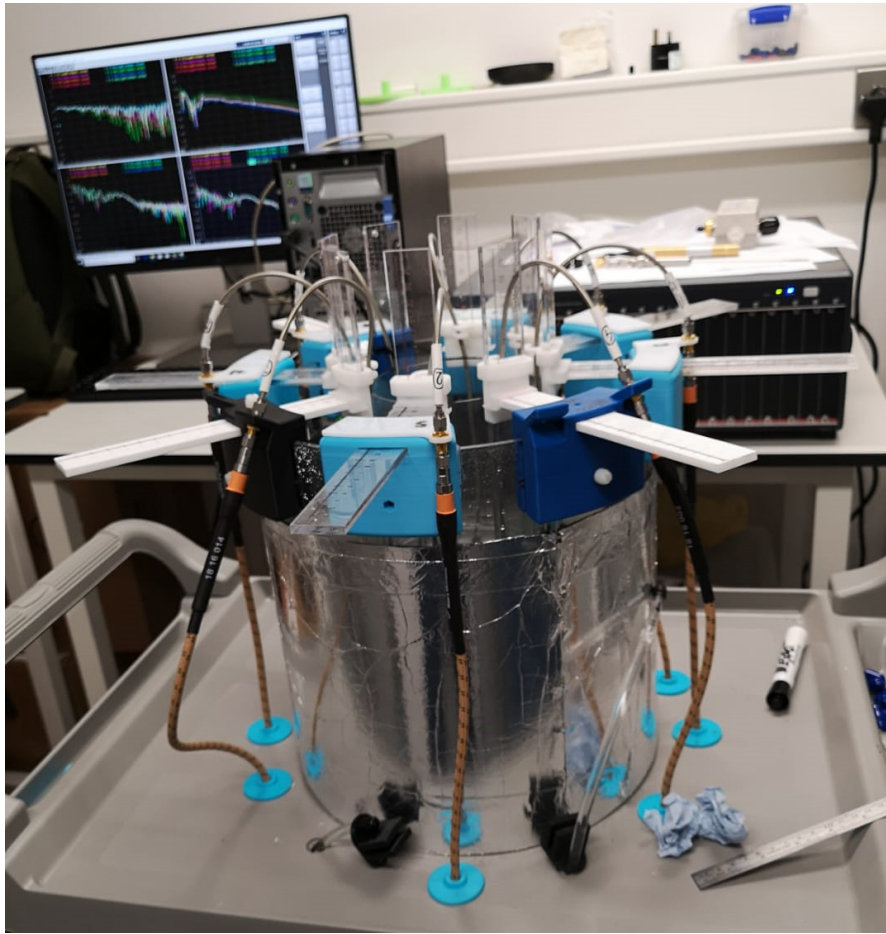


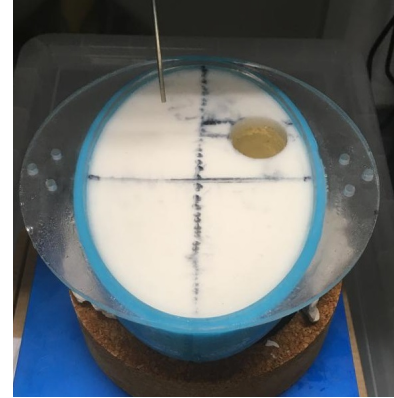
Figure 3.4: Photos of the experimental system.

is immersed in the 90%-10% glycerol-water mixture inside an imaging tank, which is made of acrylic and is surrounded by absorbing material ECCOSORB MCS covered by a metallic shield. A printed monopole triangular patch antenna operating well in the frequency range 0.5–2 GHz [136] is used, as shown in Figure 3.7. The antenna array is placed at different heights to evaluate reconstruction performance, including positions near the bottom, middle, and top. However, the signals of the top case are poor due to the influence of the curvature of the phantom, reflecting the EM wave up to the air, which is not captured by the antenna.

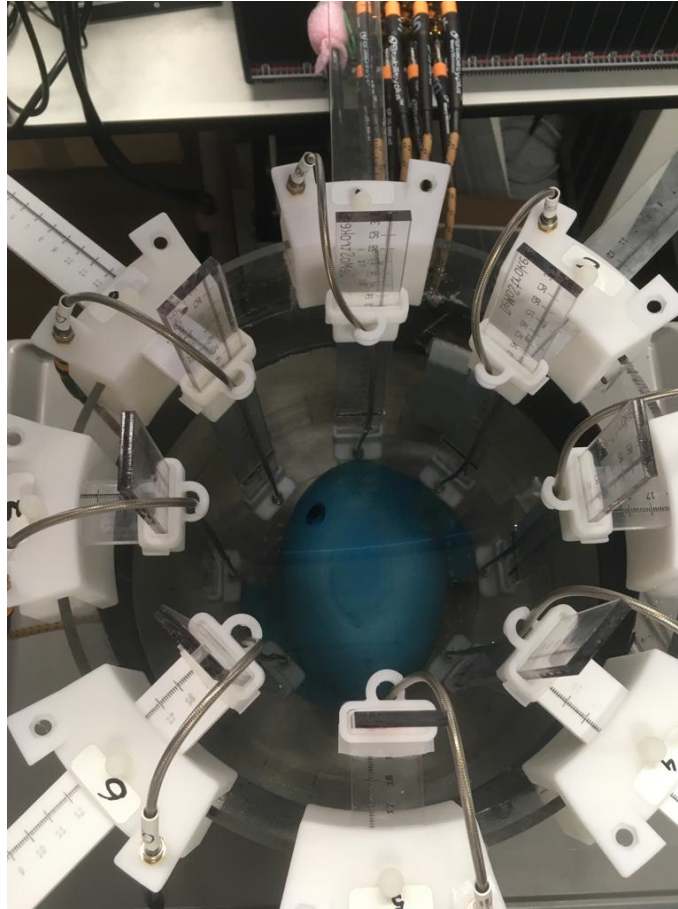
3.3. NUMERICAL AND EXPERIMENTAL MODELS



(a)



(b)



(c)

Figure 3.5: Photos of (a) brain phantom, (b) phantom with target inserted, and (c) phantom placed inside the experimental tank.

3.4. ERROR DEFINITION

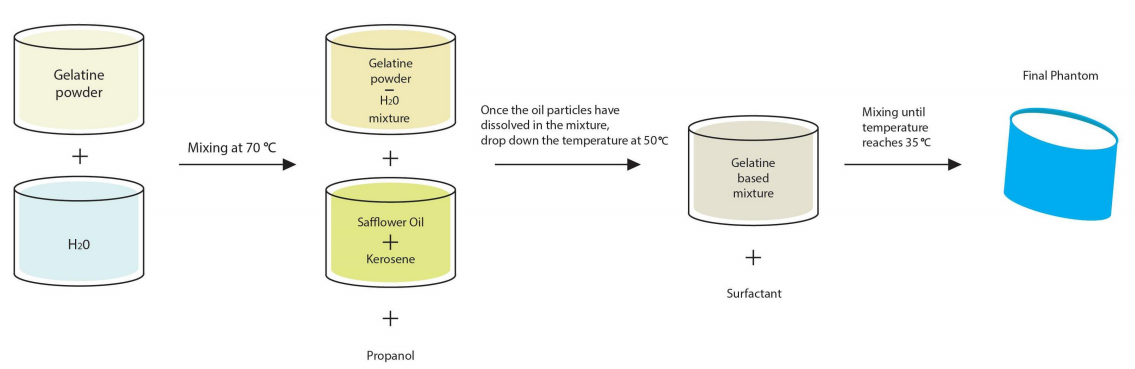
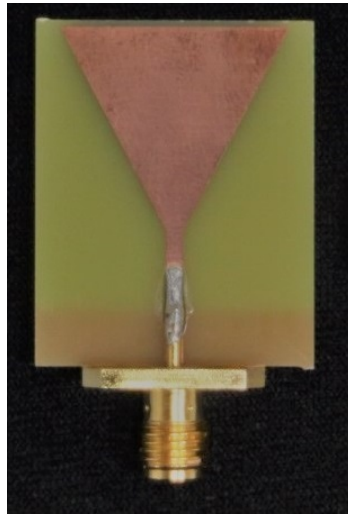


Figure 3.6: Process of making the brain phantom.



(a)

Figure 3.7: The monopole antenna used in the experimental system.

3.4 Error definition

Several errors related to the reconstruction results are used to evaluate the DBIM performance. The relative residual error (RRE) to estimate the residual \mathbf{b} is defined as

$$\text{RRE} = \frac{\|\mathbf{b}_K\|_2}{\sqrt{\sum_{m,n} |E_s(\mathbf{r}_n, \mathbf{r}_m)|^2}}, \quad (3.41)$$

3.5. CONCLUSION

which can also be used as a stop criterion for the DBIM procedure when a preset value is satisfied.

To assess the reconstruction accuracy of the FEM reconstruction results, the relative error of the reconstructed value with respect to the ground truth can be defined, including the relative errors of the real and imaginary parts as

$$e_{\epsilon'} = \frac{\|\epsilon'_{\text{tg}} - \epsilon'_r\|_2}{\|\epsilon'_{\text{tg}}\|_2}, e_{\epsilon''} = \frac{\|\epsilon''_{\text{tg}} - \epsilon''_r\|_2}{\|\epsilon''_{\text{tg}}\|_2}, \quad (3.42)$$

respectively, where $\epsilon'_{\text{tg}}, \epsilon''_{\text{tg}}$ are the real and imaginary parts of the actual relative permittivity of the reconstruction domain.

Several types of errors are used to evaluate the 3-D reconstructions shown in Chapter 5. The root mean square error (RMSE) of the xy-slice reconstruction contrast is used to compare the 2-D and 3-D reconstructions, defined as

$$\text{RMSE} = \sqrt{\frac{1}{N_r} \sum_{\mathbf{r} \in V} e_{\epsilon}^2(\mathbf{r})}, \quad (3.43)$$

where N_r is the number of voxels inside the reconstruction region V , The max error of the xy-slice reconstruction contrast is defined as

$$e_{\max} = \max |\epsilon'_{\text{tg}} - \epsilon'_r|. \quad (3.44)$$

3.5 Conclusion

In this chapter, the proposed DBIM approaches using FEM and FDTD with FISTA as inverse solver have been presented. The parameters used in the proposed approach have been discussed. Moreover, numerical and experimental models, including the materials and system used in this work, have been presented.

Chapter 4

Reconstruction with the 2-D FEM-based and FDTD-based DBIM

In this chapter, the performance of the proposed FEM-based DBIM is validated with numerical data since the FDTD-based DBIM was already evaluated in previous work [137]. The impact of using the FEM and FDTD method as forward solvers for the DBIM is compared using cylindrical target cases, followed by comparisons of reconstructions using different inverse solvers. Finally, considering there is no big difference between the two forward solvers, the proposed 2-D FDTD-based DBIM FISTA approach is used to perform reconstructions with simulated data from CST and experimental data.

4.1 Assessment of the 2-D reconstruction images

To assess the reconstruction images, some criteria can be used including the relative errors of permittivity, reconstructed permittivity values, and target position if the actual values of targets are known, which can be calculated after reconstruction. For the numerical models, these values are accurately known. Reconstructions can be considered as “good” when the obtained contrast inside the target domain is much higher than the other part of the reconstruction domain (the average contrast value of the target domain is several times bigger than that of the other area), which means that the reconstructed values are close to the actual values and relative error of the permittivity is small, for example, the

relative error e'_ε is less than 0.1 (10%) for simple cases. However, for numerical models with complicated structures and experimental scenarios where the actual values are only approximated and measured from experiment, the relative errors are not accurate and may be significantly affected by experimental noise, which can just be used as an auxiliary criterion. Thus, the assessment mainly depends on the contrast, with higher average value inside the target domain that is more than two times bigger than the other area.

4.2 Validation with the FEM-based DBIM

In this section, reconstruction results of the FEM-based DBIM with numerical are performed for validation, of which the reconstruction frequency is selected to be 1.0 GHz. Eight antennas placed in a circular ring are used as transmitters and receivers for all the following FEM simulations, where antennas are modelled as point sources and the CGLS algorithm is used as the inverse solver. For the overall computational FEM domain as well as for the circular imaging subdomain of radius ρ_r , the centre point is the origin $(0,0)$, and the horizontal and vertical directions are set at the x -, and y -axis, respectively.

The stopping criterion of the DBIM can be set based on the convergence of RRE. In practical setups, a fixed number of iterations is usually used [131], and here it is set to 15 as it guarantees convergence. The average running time of each DBIM iteration is defined as t_m .

The FEM simulation models used for validation are shown in Table 4.1. Values for the relative residual error and the relative errors of permittivity, as well as the average running time, are given in Table 4.2 for the reconstructions of the numerical models in the following. The simulated data for all the reconstructions is generated using the FEM with a known target configuration but with a different mesh from the one used in reconstruction that only has the background information, avoiding the so-called inverse crime

4.2. VALIDATION WITH THE FEM-BASED DBIM

Table 4.1: FEM simulation model number and description.

No.	Description
1	Single weak scatterer, first-order element.
2	Two weak scatterer, first-order element.
3.1	Two strong scatterers at Position 1, first-order element.
3.2	Same as 3.1 but with second-order element.
3.3	Same as 3.1 but with traditional approach.
3.4	Same as 3.2 but with traditional approach.
4.1	Two strong scatterers at Position 2, first-order element.
4.2	Same as 4.1 but with traditional approach.

Table 4.2: Relative errors and time of the FEM simulation models

No.	1	2	3.1	3.2	3.3	3.4	4.1	4.2
RRE	0.0236	0.0144	0.0032	0.0012	0.0033	0.0012	0.0027	0.0028
$e_{\varepsilon'}$	0.0670	0.0766	0.0873	0.0835	0.0875	0.0837	0.1020	0.1022
$e_{\varepsilon''}$	0.2609	0.2765	0.0492	0.0433	0.0489	0.0435	0.0630	0.0628
$t_m(s)$	1.91	1.98	1.99	2.39	92.44	259.82	1.92	98.98

in benchmarking performance.

First, a simple model (FEM Model 1) with a single circular target is used to test the FEM-based DBIM implementation. The frequency used in this model is 1.0 GHz, and the radius of the antenna array is $\rho_{\text{ant}} = \lambda = 30$ cm, where λ represents the wavelength of the incident wave. The radius of the total and reconstruction domains are $\rho_C = 2\lambda = 60$ cm and $\rho_r = 0.9\lambda = 27$ cm, respectively. The relative permittivity of the background medium is $\varepsilon_b = 1 - 0.1j$, and for the target located at (-3 cm, -3 cm) with radius $\rho = 0.3\lambda = 9$ cm, it is $\varepsilon_{\text{tg}} = 1.6 - 0.5j$. In the inversion, the initial start profile is the background medium only. The mesh includes 6212 triangular elements and 3203 d.o.f, of which 1244 triangular elements are inside the reconstruction domain. First-order Lagrange elements (with 3 d.o.f each) are considered in FEM. Reconstruction images are shown in Fig. 4.1(a)

and Fig. 4.1(b), where only the reconstruction domain is shown and the exact target size is marked with a black circle.

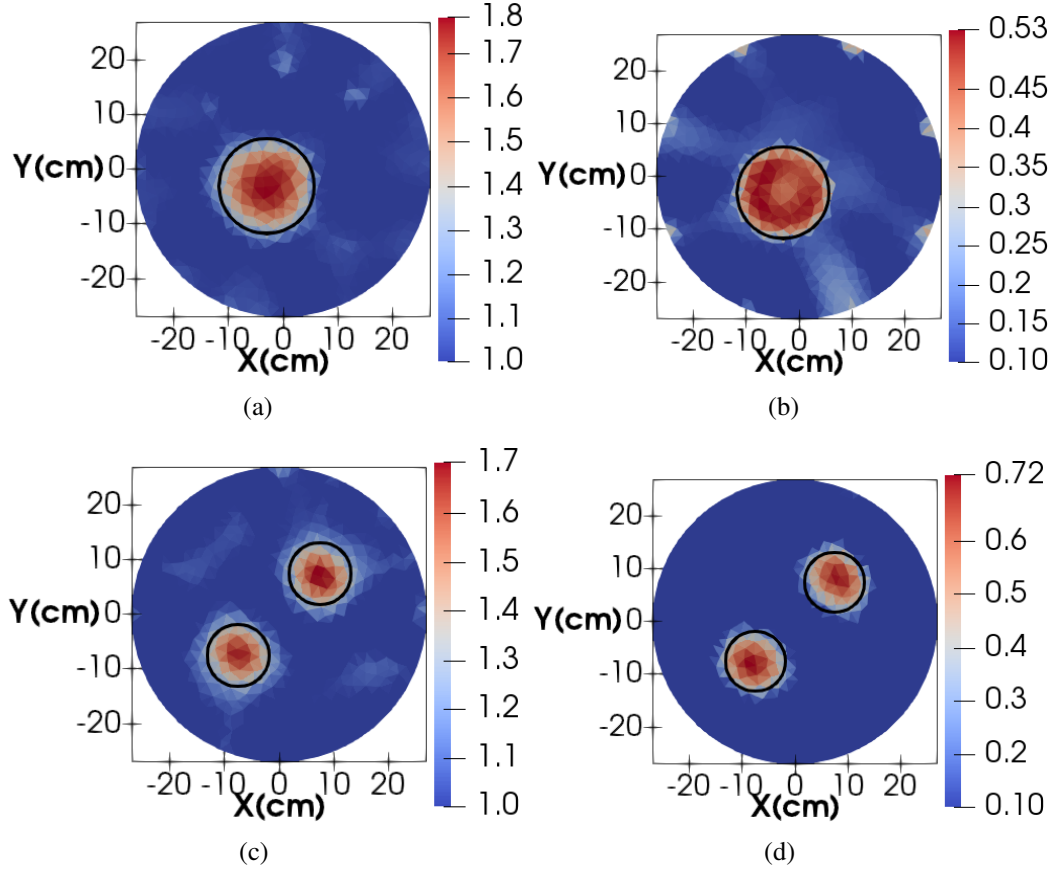


Figure 4.1: Single-target ($\epsilon_{\text{tg}} = 1.6 - 0.5j$) reconstruction with 15 DBIM iterations at 1.0 GHz: (a) real part of ϵ_r , (b) imaginary part of ϵ_r (FEM Model 1). Two-target reconstruction with 15 DBIM iterations at 1.0 GHz: (c) real part of ϵ_r , (d) imaginary part of ϵ_r (FEM Model 2).

Reconstructions of similar quality are achieved for the second model (FEM Model 2), including two targets with the same permittivity as Model 1. Results are shown in Fig. 4.1(c) and Fig. 4.1(d). The only differences with respect to Model 1 are the radius and positions of the targets, which are $\rho = 0.2\lambda = 6$ cm and $(\mp 7.5$ cm, ∓ 7.5 cm) in Model 2. The mesh for the reconstruction is exactly the same as Model 1. The average running time t_m of both models is shown in Table 4.1. As can be seen from the above two weak-

scattering simulation scenarios, the reconstruction results recover the targets clearly, and the permittivity values are very close to the original values.

Another numerical model (FEM Model 3.1), with much higher values of ϵ_r'' in both the background medium as well as the targets, has been used to test the algorithm's ability to reconstruct scenarios with high losses. In particular, the relative permittivity of the background and targets are $\epsilon_b = 16 - 12.1j$ and $\epsilon_{tg} = 25 - 15.5j$, respectively, and the targets are located at $(\mp 2.5 \text{ cm}, \mp 2.5 \text{ cm})$, named Position 1. Reconstruction results are shown in Fig. 4.2(a) and 4.2(b).

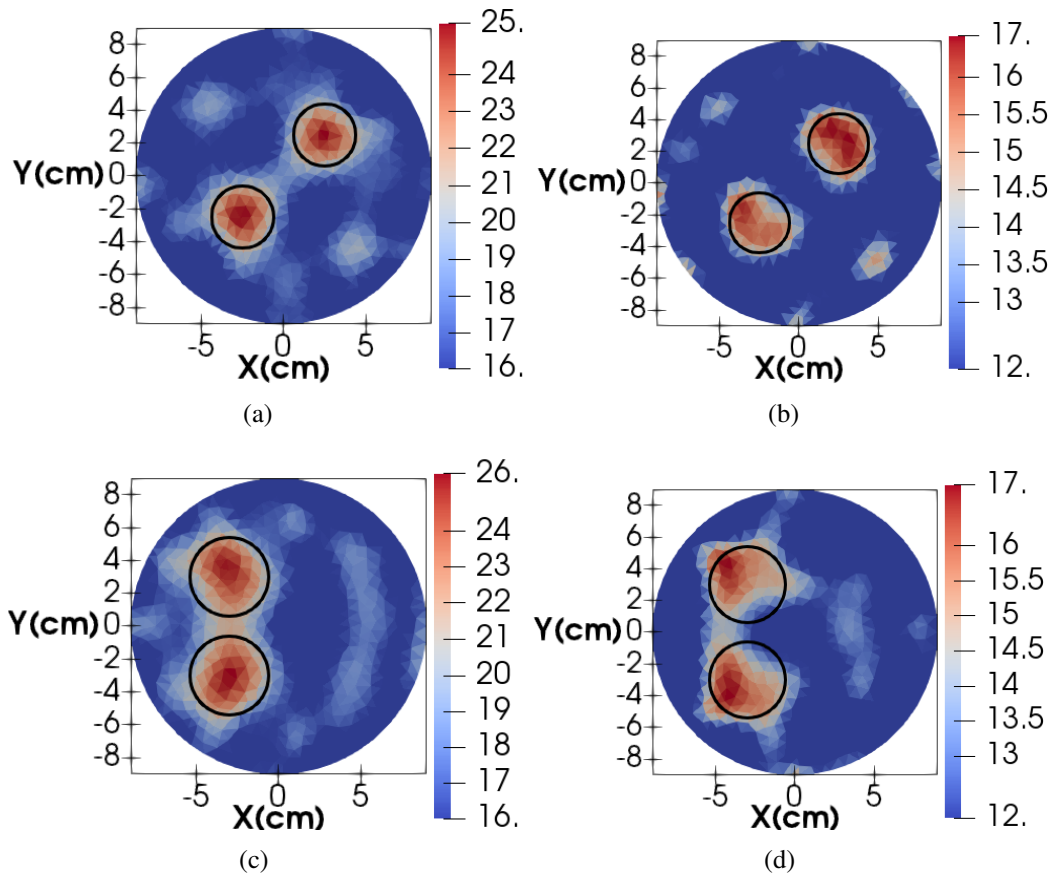


Figure 4.2: Two high-permittivity targets ($\epsilon_{tg} = 25 - 15.5j$) reconstruction with 15 DBIM iterations at 1.0 GHz. Position 1: (a) real part of ϵ_r , (b) imaginary part of ϵ_r (FEM Model 3.1). Position 2: (c) real part of ϵ_r , (d) imaginary part of ϵ_r (FEM Model 4.1).

The radius of the antenna array, the total domain, the imaging domain and the targets

are $\rho_{\text{ant}} = 10$ cm, $\rho_C = 20$ cm, $\rho_r = 9$ cm and $\rho = 2$ cm. The mesh is made up of 6237 triangular elements and 3212 d.o.f, of which 1263 triangular first-order elements are used for the reconstruction domain in Fig. 4.2. While there are stronger artefacts in these images due to the higher losses, the targets are still recovered with accuracy in terms of position and permittivity values.

Another reconstruction is performed with the same number of iterations for the same geometry but using second-order elements (6 d.o.f each), referred as Model 3.2, for which the mesh is the same as Model 3.1, but the number of d.o.f is increased up to 12660. The comparison in relative errors between these two models is shown in Table 4.2. RRE is lower for Model 3.2 than for Model 3.1, although this does not translate to a significant reduction of relative errors $e_{\varepsilon'}$ and $e_{\varepsilon''}$. To compare the proposed approach with the conventional approach in (3.20), another reconstruction has been performed for the same geometry with first-order and second-order elements, which is noted as Model 3.3 and Model 3.4, respectively. Reconstruction images of Model 3.2, 3.3 and 3.4 are not shown here, as the images of these methods are similar to the images of Model 3.1. The conventional approach of Model 3.3 achieves similar results to Model 3.1 in terms of relative errors, which is expected as the element order is the same and the mesh is fine enough.

However, the average running time for each DBIM iteration is 92.44 s and 259.82 s for Model 3.3 and Model 3.4, respectively, but only 1.99 s and 2.39 s for Model 3.1 and Model 3.2. This difference suggests significant computational savings for the proposed approach, especially for higher-order elements. It should be noted that the two methods are coded in the same language using the FEniCS software tool [125], and the only difference is how (3.19) is built, for which the linear combination of the field used in the traditional method is calculated by the code provided by the FEniCS tool. The reconstruction errors of the ill-posed ISPs are not only related to how the integration is built but also influenced by

the mesh fineness, inverse solver, *etc.*

To further compare the proposed method with the traditional method, reconstructions are performed using first-order elements for another model (FEM Model 4.1, and 4.2 for the new and conventional methods respectively), where two targets of radius $\rho = 2.5$ cm centred at $(-3 \text{ cm}, \pm 3 \text{ cm})$, named Position 2, are placed close to each other. The mesh in the reconstruction is same as before. Reconstructions of the proposed method are shown in Fig. 4.2(c) and Fig. 4.2(d), and the relative errors and average running time of reconstruction by both methods are given in Table 4.2, which again confirm the great computational savings of the proposed method.

4.3 Impact of the forward solver

In this section, comparison of the FEM-based and FDTD-based DBIM is performed to investigate the impact of the forward solver. Reconstructions are performed to evaluate the proposed algorithm with experimental data, including data obtained from the MWT system and Fresnel database.

Experimental data of cylindrical targets obtained from the previous MWT system using a two-port Keysight VNA system, with details shown in [134], is used to investigate the influence of forward solvers.

The relative permittivity of the glycerol-water mixture, used as background medium, is $\epsilon_b \approx 17 - 15j$ at 0.9 GHz. The radii of the antenna array, the reconstruction domain, and the total domain are $\rho_{\text{ant}} = 6.5$ cm, $\rho_r = 5.5$ cm, and $\rho_C = 12$ cm, respectively. The cylindrical targets inside glass tubes are filled with pure water with measured relative permittivity of $\epsilon_{\text{tg}} \approx 78 - 3j$ at 0.9 GHz. The first experiment considers one target case, where the target is placed at $(-2 \text{ cm}, 2 \text{ cm})$ with a radius of $\rho = 1.5$ cm. The second experiment includes two cylindrical targets, located at $(\mp 2 \text{ cm}, \pm 2 \text{ cm})$. The FEM mesh used in

4.3. IMPACT OF THE FORWARD SOLVER

both cases comprises 6327 triangles (first-order elements) and 3257 d.o.f, of which 1308 triangular elements are inside the reconstruction domain, while the FDTD uses 2 mm resolution with the same radius of reconstruction domain as the FEM. The reconstruction domain is slightly different as the square grid is used in FDTD. Before reconstruction, the background electric field of each forward solver is calculated. A ratio of the electric field for each TR pair (i, j) to evaluate the difference between the two methods is defined as,

$$R(i, j) = \frac{|E_{\text{FDTD}}(i, j)|}{|E_{\text{FEM}}(i, j)|}, \quad (4.1)$$

and the average value is defined as

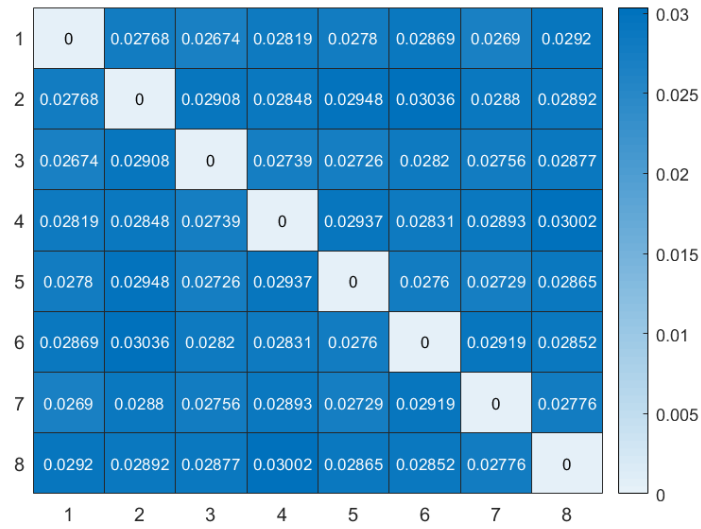
$$\bar{R} = \frac{\sum_{i \neq j} R(i, j)}{N_{\text{TR}}}, \quad (4.2)$$

where N_{TR} is the number of the TR pairs without the diagonal (monostatic data is discarded). The ratio $R(i, j)$ and normalised ratio $\frac{R(i, j)}{\bar{R}}$ are shown in Fig. 4.3 and Fig. 4.4. The standard deviation of the ratio without the diagonal is 9.07E-4, which shows good agreement.

Reconstruction results of the real and imaginary parts for the single target case after 15 DBIM iterations using the two forward solvers for DBIM at 0.9 GHz are shown in Fig. 4.5, where the targets are marked in black and only the reconstruction domain is shown. The reconstruction images show similar target position and shape, though the reconstruction values are different. The RRE values for the two solvers are not similar due to the calibration step, which are 0.0253 and 0.238 respectively. Reconstruction results of the two cylindrical target case by both methods are similar except the reconstruction values, as shown in Fig. 4.6, and the RRE values are 0.0294 and 0.185 respectively.

It is evident from these results that, although the experimental data include measure-

4.3. IMPACT OF THE FORWARD SOLVER



(a)

Figure 4.3: Ratio of the calculated electric field between FDTD and FEM for the TR pairs.



(a)

Figure 4.4: Normalised ratio of the calculated electric field between FDTD and FEM for the TR pairs.

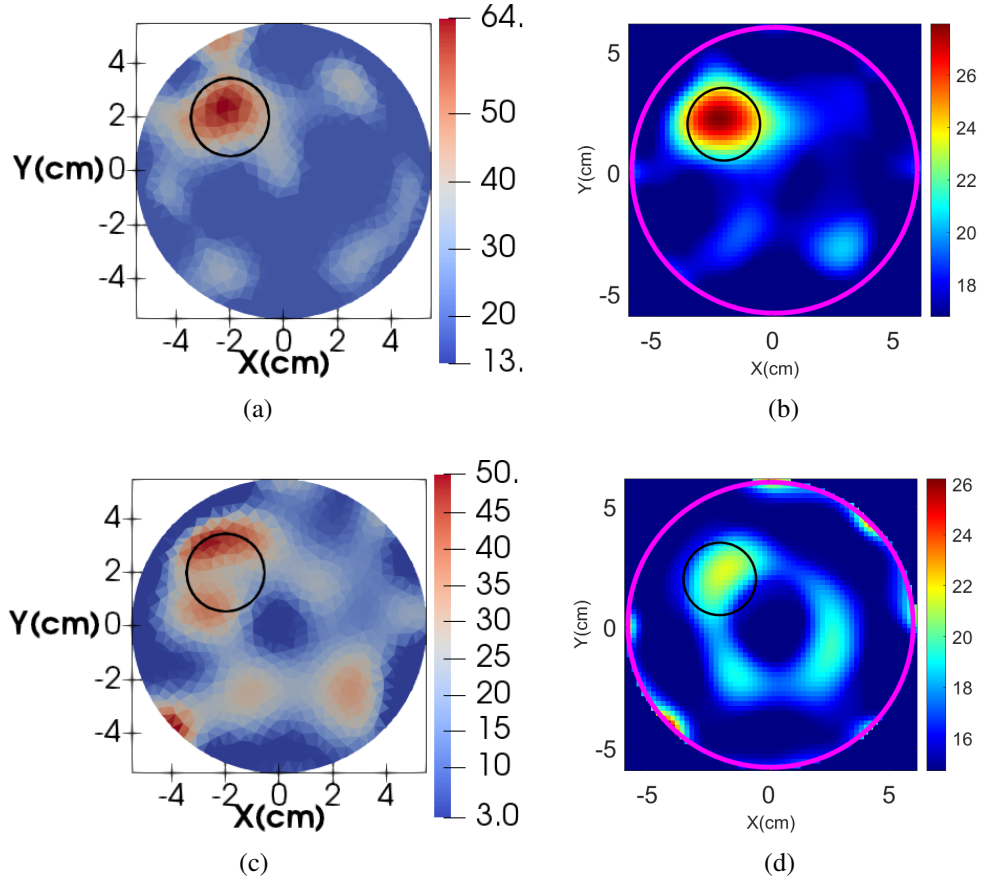


Figure 4.5: Experimental data reconstruction of single cylindrical target ($\epsilon_{tg} \approx 78 - 3j$) with 15 DBIM iterations at 0.9 GHz by FEM-based DBIM (a) real part, (c) imaginary part, and FDTD-based DBIM (b) real part (d) imaginary part.

ment errors and noise, which are absent from the numerical models, the targets are clearly detected by both methods. However, the value of the imaginary part is hard to be reached, due to the noise of the experimental environment and the lossy background materials. This results in higher errors appearing in the reconstructions of the imaginary part, as is usually the case for MWT [131]. When the ill-conditioned linear equation is solved and the real part of the target is not reached, the imaginary part of the reconstruction value will also increase to some extent. Noise in the reconstruction images can be reduced by using denoising inverse solvers, such as thresholding or compressed sensing based methods

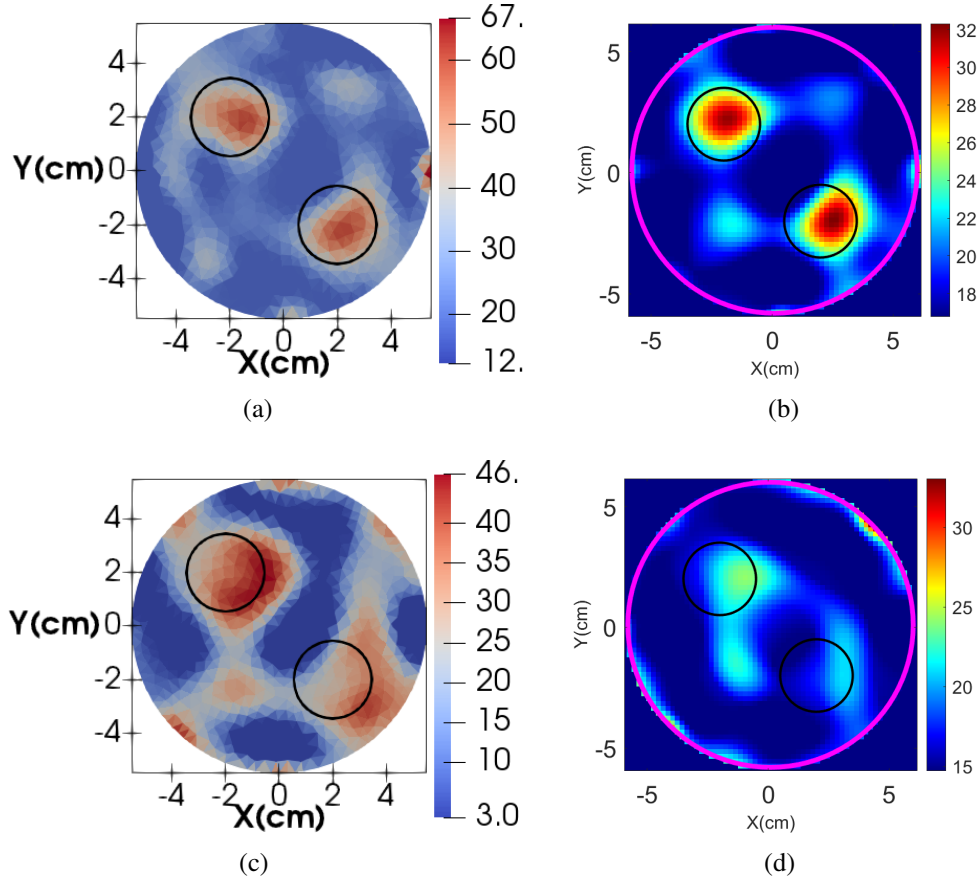


Figure 4.6: Experimental data reconstruction of two cylindrical targets ($\epsilon_{tg} \approx 78 - 3j$) with 15 DBIM iterations at 0.9 GHz by FEM-based DBIM (a) real part, (c) imaginary part, and FDTD-based DBIM (b) real part (d) imaginary part.

[67].

By comparison of the images reconstructed by the two methods, the impact of the forward solver is trivial, as both reconstruction approaches have shown similar performance. The FDTD-based DBIM can be a first choice used for reconstruction with respect to its easy implementation and mesh discretisation.

4.4 Impact of the inverse solver

4.4.1 Inverse solver for FEM-based DBIM

To investigate the impact of the inverse solver, as well as to further cross-check the capabilities of the proposed approach, experimental data from the Fresnel dataset [138] have also been tested, as the Fresnel dataset is a reliable experimental dataset for testing and validating inversion algorithms. The configuration of the setup can be found in [138], where far-field problems are considered. As the proposed approach is not designed for far-field reconstructions, the data obtained from the dataset with the smallest antenna array radius are used (as for large antenna radius, the computational memory and time increase significantly to simulate the entire domain between the antenna and the targets). The cases for cylindrical targets are considered, which suit the proposed 2-D approach as there is no big vertical variation for the materials. All targets have a radius of $\rho = 15$ mm, and their relative permittivity is $\epsilon_{\text{tg}} = 3$ (with a 10% of uncertainty). Reconstructions are performed for both the one-target case and the two-target case. The real part of the reconstructed permittivity at 1.0 GHz of the reconstruction domain is shown in Fig. 4.7, with the targets marked in a black circle. The reconstruction area is set to be $15 \text{ cm} \times 15 \text{ cm}$, with 1824 triangular first-order elements.

Part of TR pairs (108) from the dataset are selected, with 12 transmitters and 12 receivers (for each transmitter, only nine receivers are used due to the limitation of their system setup) to reduce computational time. The computational time is a limiting factor for the Fresnel dataset, which corresponds to cases of a large distance between scatterers and probes and allows a plane wave assumption and a near to far-field transformation to assist inversion. This is a very different imaging problem from the near-field simulation models considered in this thesis, which needs to include the probes inside the model,

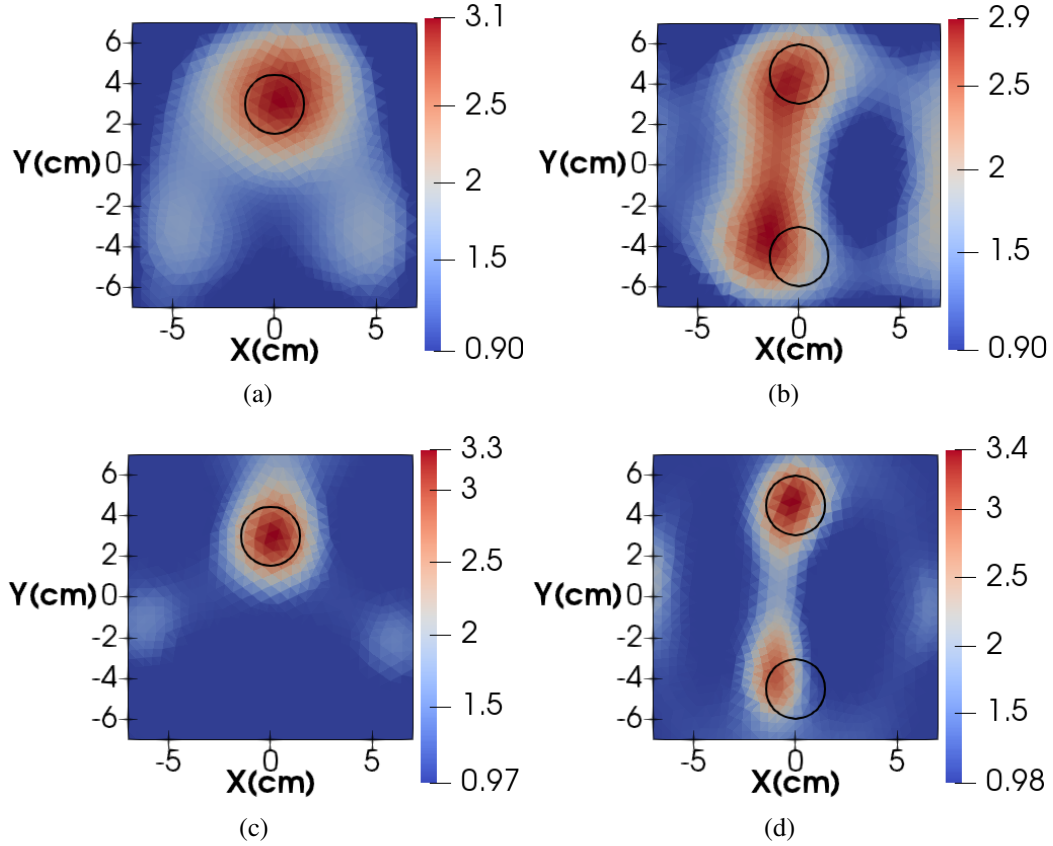


Figure 4.7: Reconstructed real part of ϵ_r of the Fresnel dataset with 15 DBIM iterations at 1.0 GHz of cylindrical targets ($\epsilon_{tg} \approx 3$). One-target case: (a) CGLS, (c) FISTA. Two-target case: (b) CGLS, (d) FISTA.

rendering the total simulation domain electrically large for high frequencies. This would result in a massive number of mesh elements and a consequent prohibitive computational burden for the forward problem. This is the reason why the frequency has been set to 1.0 GHz for this Fresnel dataset (where the receivers are placed at $\rho_{ant} = 76$ cm). In contrast, the targets are electrically small at this frequency, requiring advanced inverse solvers. Hence, reconstructions of both the CGLS algorithm and FISTA are performed and compared.

Reconstruction results of the two different inverse solvers are shown in Fig. 4.7. The proposed FEM algorithm can reconstruct the single target with both solvers, but

the two targets can only be clearly resolved with FISTA, confirming the super-resolution properties of this algorithm which discriminates the two targets despite their electrical distance being lower than the resolution limit. The RRE values of both cases are 0.0823 and 0.1135, respectively.

4.4.2 Inverse solver for FDTD-based DBIM

4.4.2.1 Comparison of CGLS and FISTA

A comparison at frequency 1.0 GHz between CGLS and FISTA is shown in Fig. 4.8 for a simple case that two small circular targets are located close to each other in a lossless homogeneous background. The background Debye parameters are $\epsilon_\infty = 1$, $\Delta\epsilon = 0$, $\sigma_s = 0$, while for the targets, the Debye parameters are $\epsilon_\infty = 1.6$, $\Delta\epsilon = 0$, $\sigma_s = 0$. The radius of the two targets is 45 mm, and the distance between the centres of the two targets is 120 mm. The number of iterations of CGLS and FISTA is set equal to evaluate the two algorithms fairly.

FISTA shows a much lower RRE than CGLS, and the residual error curve has a monotonic behaviour. The relative errors of the permittivity e_ϵ are similar, which are 0.01542 for FISTA and 0.0183 for CGLS. The reconstruction image of FISTA is also better, as it manages to resolve the two targets more clearly than CGLS.

4.4.2.2 Comparison of TwIST and FISTA

A 2-D breast model from the University of Wisconsin Cross-Disciplinary Electromagnetics Laboratory (UWCEM) numerical breast phantom repository (ID = 062204) [139] has been used to compare the performance of TwIST and FISTA. Sixteen antennas modelled as point sources are placed around the breast model. The breast model is immersed in a lossless background medium with $\epsilon_\infty = 2.6$, $\Delta\epsilon = 0$, $\sigma_s = 0$, and the skin of the breast

4.4. IMPACT OF THE INVERSE SOLVER

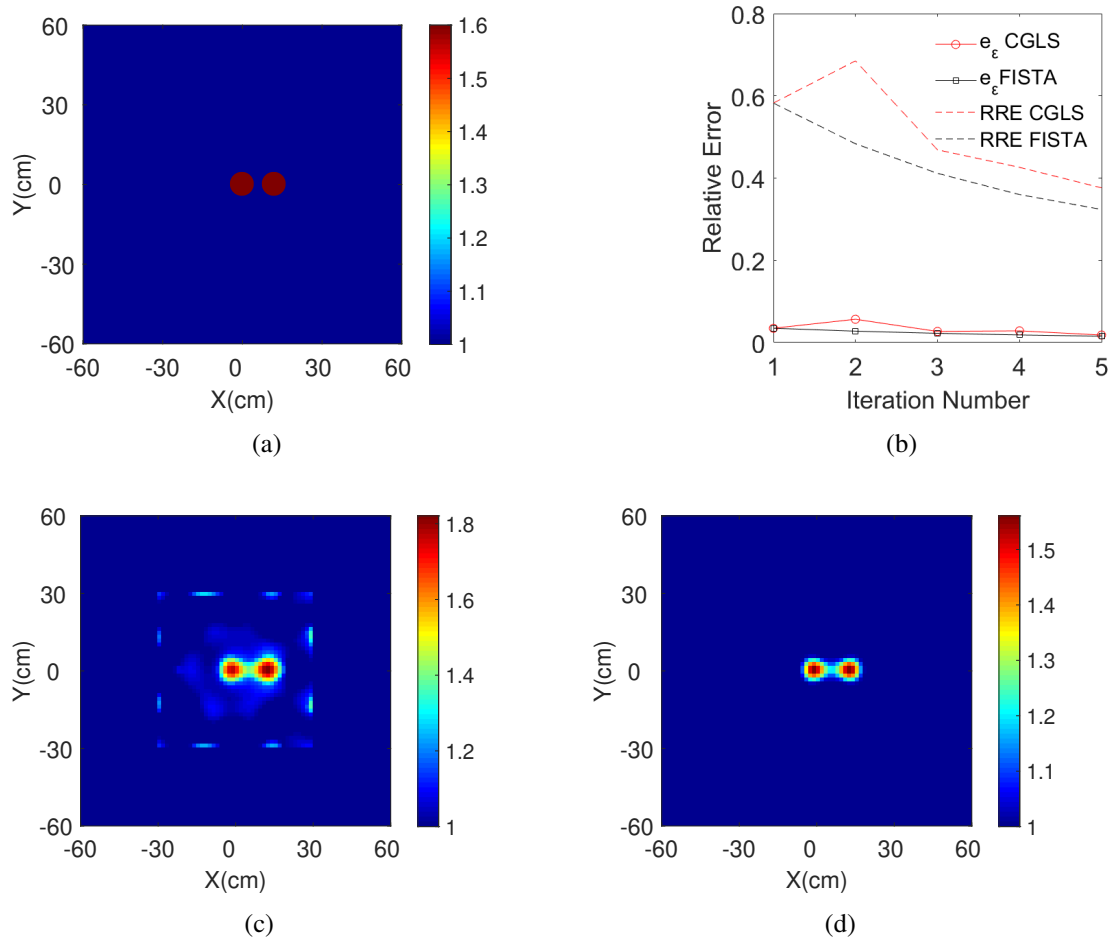


Figure 4.8: Reconstruction results of two weak scatterers using CGLS and FISTA after 5 DBIM iterations: (a) ϵ_∞ of the original image, (b) relative residual error RRE and relative error of permittivity e_ϵ of CGLS and FISTA, (c) reconstruction by CGLS, (d) reconstruction by FISTA.

model is assumed to be known exactly for reconstruction. An initial guess of the breast model is needed to ensure that the algorithms produce a reliable image. The initial guess is set as the values from [118], where $\epsilon_\infty = 11.27$, $\Delta\epsilon = 5.51$, $\sigma_s = 0.080$, shown in Fig. 4.9. To compare the performance of TwIST and FISTA, the number of iterations is fixed as 25, and λ for the soft thresholding function (2.71) is the same for both algorithms. The first single-frequency reconstructions are performed at 1.5 GHz and 2.0 GHz with 60 DBIM iterations. As shown in Fig. 4.10 and Fig. 4.11, the reconstruction images of

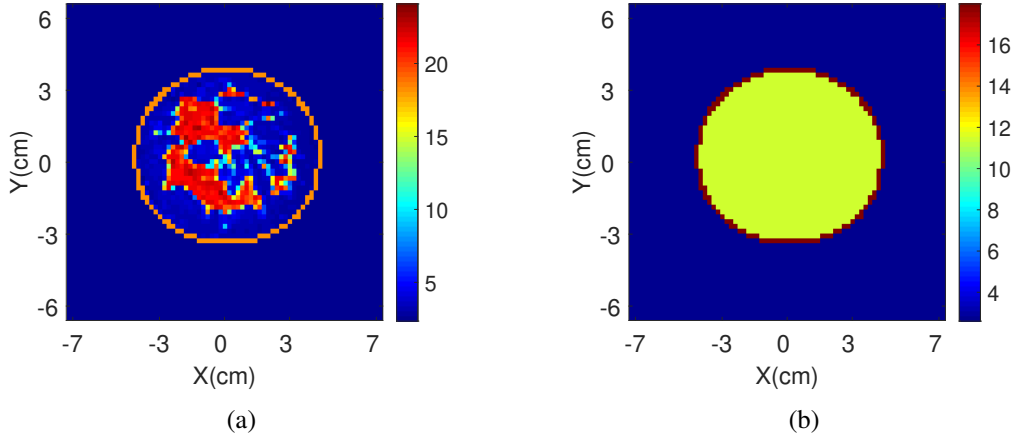


Figure 4.9: Ground truth and initial guess of the breast model.

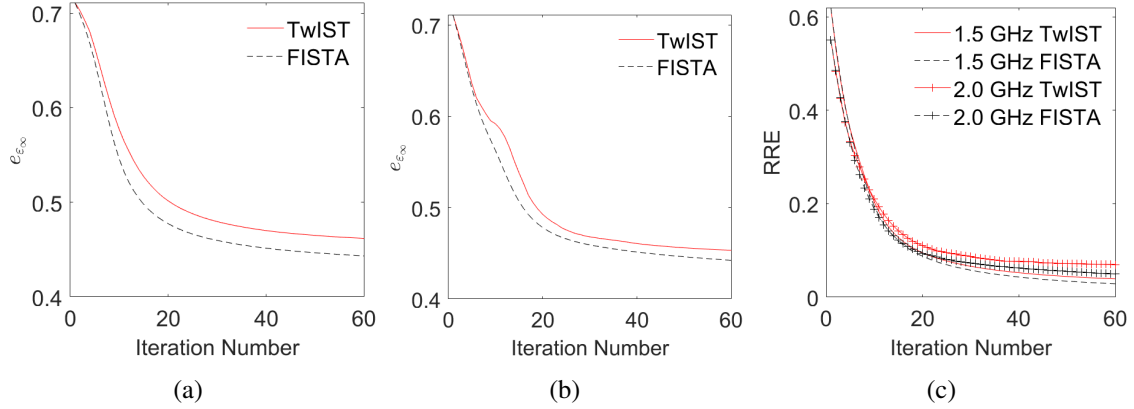


Figure 4.10: Relative error of epsilon infinity $e_{\epsilon_{\infty}}$: (a) 1.5 GHz, (b) 2.0 GHz, and relative residual error RRE: (c) by TwIST and FISTA, with single-frequency approach after 60 DBIM iterations.

FISTA and TwIST are very similar, but all relative errors of FISTA are smaller than those of TwIST in both cases, suggesting that FISTA has slightly better performance than the TwIST algorithm.

Using the frequency hopping technique, comparison between the reconstruction results of FISTA and TwIST is shown in Fig. 4.12 and Fig. 4.13. The frequencies are selected as 1.5 GHz – 2.0 GHz – 2.5 GHz – 3GHz, and 15 DBIM iterations are performed at each frequency with a total of 60 DBIM iterations. The number of iterations of

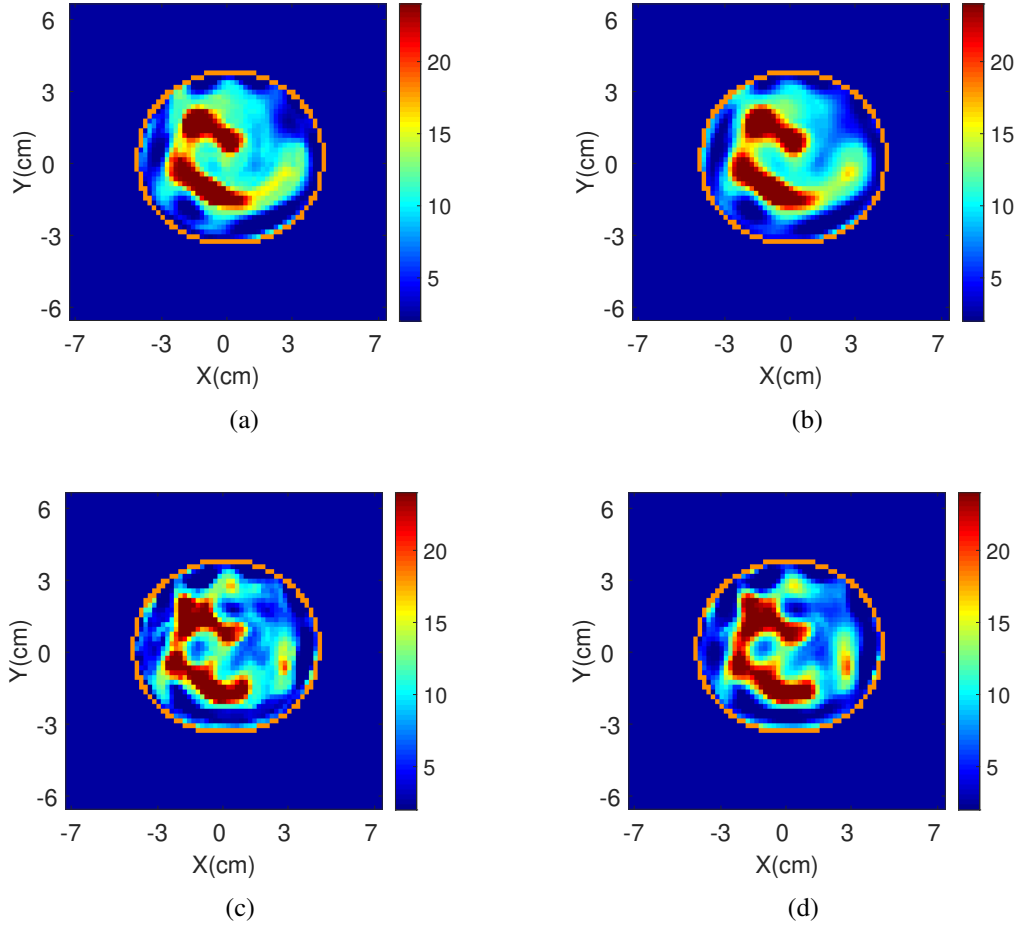


Figure 4.11: (a)(c) Reconstruction values of ϵ_∞ by TwIST at 1.5 and 2.0 GHz, respectively. (b)(d) Reconstruction values of ϵ_∞ by FISTA at 1.5 and 2.0 GHz, respectively.

FISTA/TwIST and the initial guess for the breast model are the same as before. Similarly, the results of TwIST and FISTA are nearly identical, but all the relative errors of FISTA are lower than those of TwIST. Furthermore, compared to the single frequency results, the frequency hopping approach improves resolution and reduces the relative error of epsilon infinity e_{ϵ_∞} .

4.4. IMPACT OF THE INVERSE SOLVER

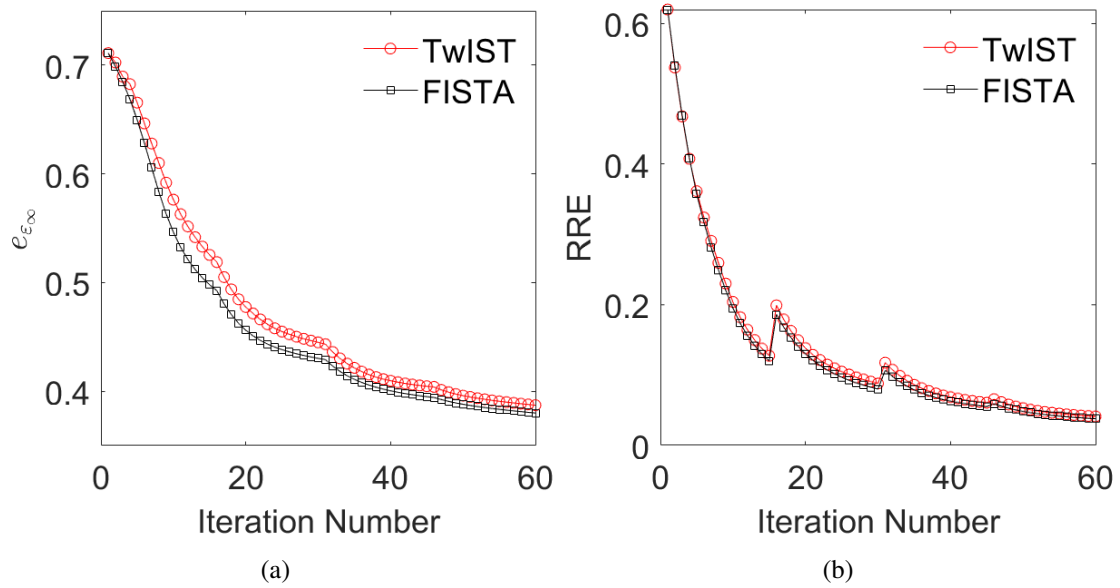


Figure 4.12: Relative errors of the breast model by TwIST and FISTA with frequency hopping approach after 60 DBIM iterations: (a) relative error of epsilon infinity $e_{\epsilon_{\infty}}$ of TwIST and FISTA, (b) relative residual error RRE.

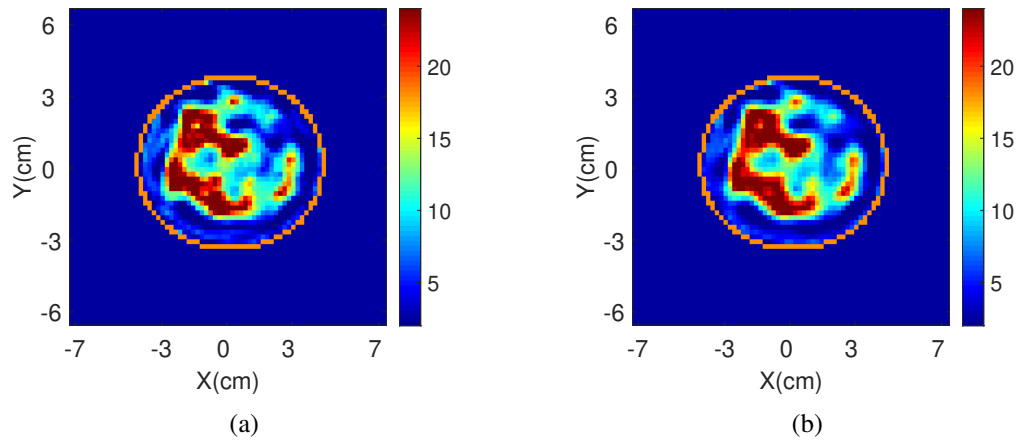


Figure 4.13: Reconstructions of the breast model by TwIST and FISTA after 60 DBIM iterations with frequency hopping approach: (a) reconstruction by FISTA, (b) reconstruction by TwIST.

4.5 Reconstruction with the 2D FDTD-DBIM-FISTA

Based on the above comparisons, an optimised choice is to use FDTD as the forward solver and FISTA as the inverse solver. In this section, the application of the 2-D DBIM-FISTA approach using FDTD is presented for the reconstructions of numerical and experimental models.

4.5.1 CST data reconstructions

4.5.1.1 Cylindrical models

The CST model of the experimental system [134] and the SAM model with a blood target inside the brain have been considered. Data obtained from these models have been tested for reconstruction. The 2D cross-sectional geometry along the antenna plane is used as the FDTD forward solver in MWI problems. Eight antennas placed in a circle are used for both cases.

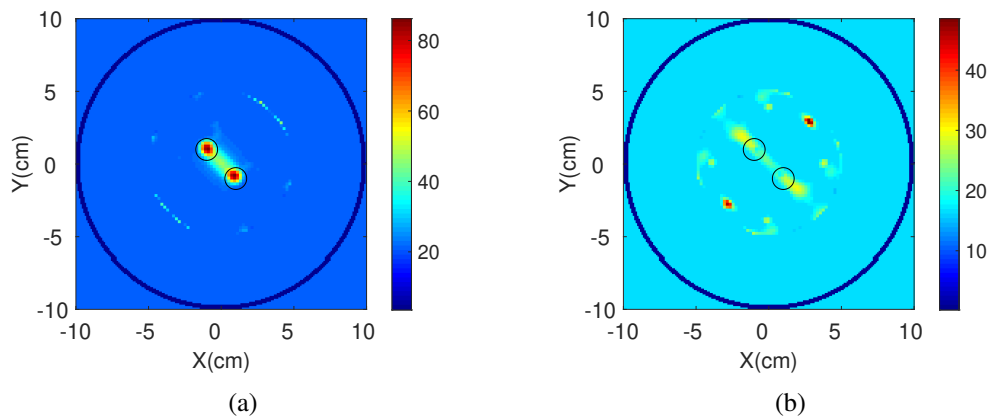


Figure 4.14: Reconstruction images of (a) real part of permittivity, (b) imaginary part of permittivity.

The first CST case is shown in Fig. 4.14. The background is a 90% glycerol-water

mixture, and two cylinders close to each other are filled with water. The diameters of the antenna array, the cylinders, the inner tank, and the outer tank are 66 mm, 15 mm, 50 mm and 100 mm, respectively. The relative permittivity of pure water is $\epsilon_r = 78 - 4.8j$ at 1.2 GHz. Reconstructions are performed using the frequency-hopping approach at frequencies 1.2 GHz - 1.4 GHz - 1.6 GHz with 20 DBIM iterations for each frequency. The tolerance is set as 1E-4 for FISTA. As shown in Fig. 4.14(a) and Fig. 4.14(b), the reconstruction images of FISTA clearly resolve the two targets, and the real part of the recovered permittivity values calculated at 1.2 GHz is close to the actual.

4.5.1.2 SAM model

The SAM model shown in Fig. 3.2 is imported into CST to obtain the measured data with eight antennas placed in a circle. The 2-D FDTD simulation approximates the cross-sectional plane of the 3-D model with a similar size, and the initial guess includes the head slice with bone and brain, placed in a homogeneous background with 90% glycerol-10% water mixture. The first reconstruction is performed at 0.8 GHz with 20 DBIM iterations, and the tolerance is set as 1E-3 for FISTA. Then reconstructions with frequency hopping have been performed at six frequencies (0.6 GHz - 0.8 GHz - 1 GHz - 1.2 GHz - 1.4 GHz - 1.6 GHz) with 20 DBIM iterations for each frequency. The number of iterations for FISTA is fixed at 150. The reconstruction images are shown in Fig. 4.15, both approaches detect the target, but the frequency-hopping approach shows better recovered values than the single-frequency approach.

4.5.2 Zubal model

In this subsection, reconstruction results of the Zubal model using the FDTD and CST measurement data are presented. For the measurement data obtained from 2-D FDTD

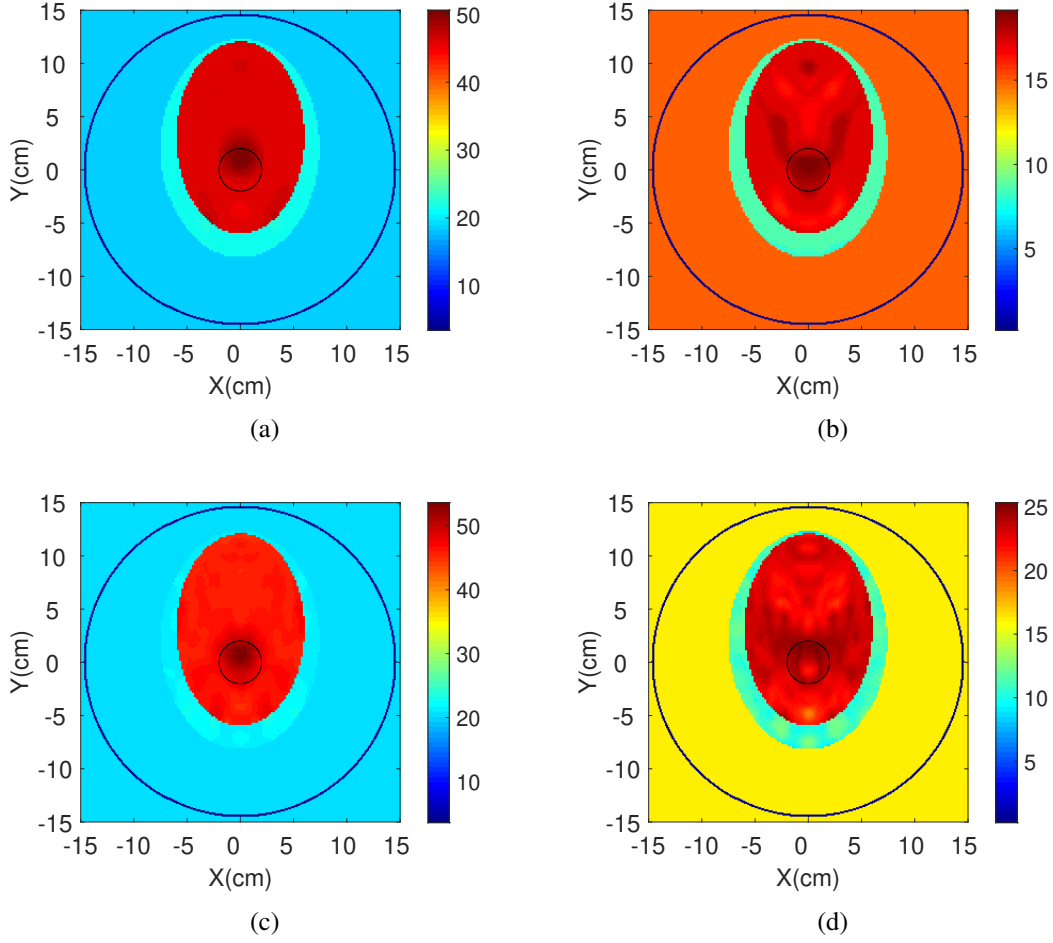


Figure 4.15: Reconstruction images of real part of permittivity (left) and imaginary part of permittivity (right) of the SAM head model: (a)(b) reconstruction at 0.8 GHz with the single frequency approach, (c)(d) reconstruction with the frequency hopping approach.

simulations, a simplified model is used as the antennas are modelled as point sources, and a TM wave is considered. However, CST simulations model the antenna structure and simulate a fully 3-D vectorial EM wave, similar to the experiment.

It is important to note that the complex structure of the head cannot be known a priori, resulting in a highly nonlinear and ill-posed EM ISP. Assuming that some prior information may be available, it is important to investigate performance under different imaging scenarios. To this end, the DBIM with FISTA [117] is applied to 2-D numerical brain

phantoms in different scenarios. Results show that it is possible to reconstruct the target inside a head phantom of known shape with several unknown tissue layers [140].

4.5.2.1 Reconstruction with FDTD data

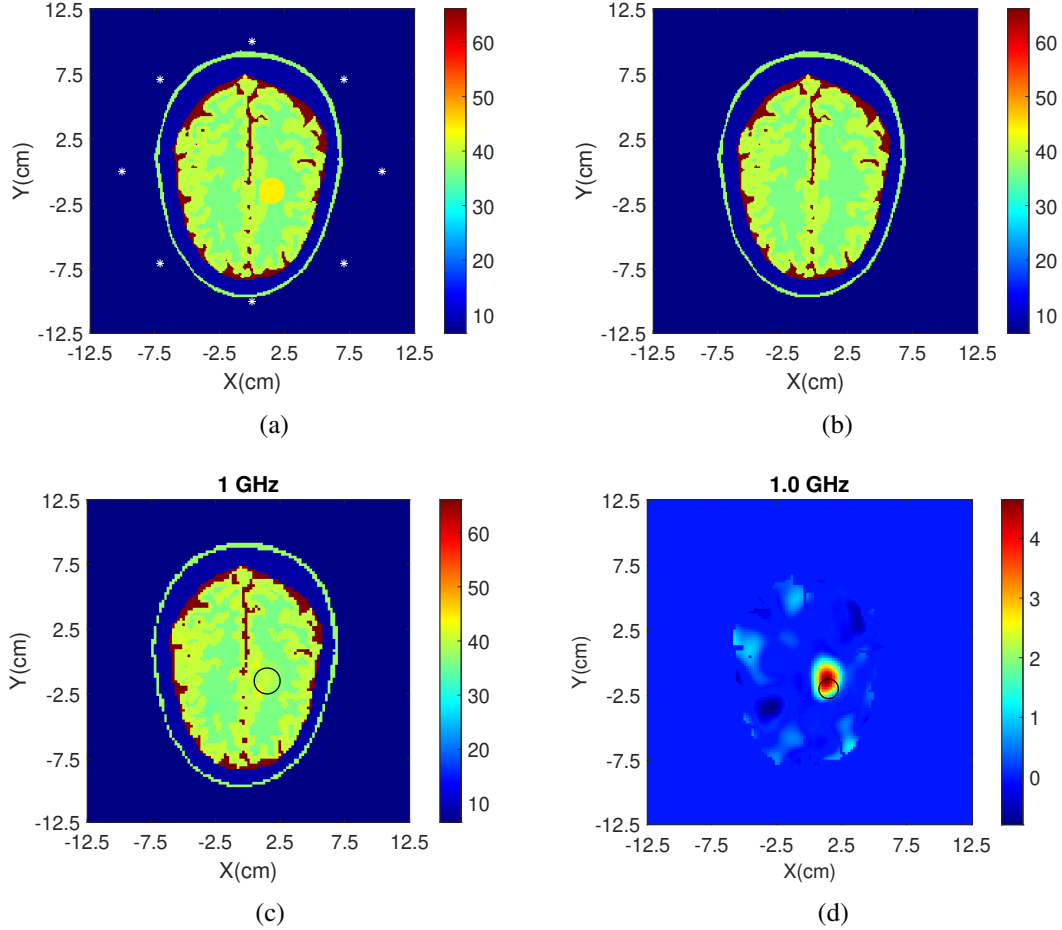


Figure 4.16: Reconstruction results of ϵ_∞ of the full head plus the blood target at 1.0 GHz: (a) ground truth, (b) initial guess, (c) reconstruction, (d) reconstruction contrast of ϵ_∞ .

The first model is the full head plus a blood target with radius 15 mm, shown in Fig. 4.16(a), where eight antennas are placed in a circle with radius $\rho_{\text{ant}} = 100$ mm, marked in white colour. Assuming that the full head is known except for the blood target in Fig. 4.16(b), the reconstruction results of ϵ_∞ at 1.0 GHz are shown in Fig. 4.16(c) and Fig.

4.16(d) where the contrast is presented to show the results better.

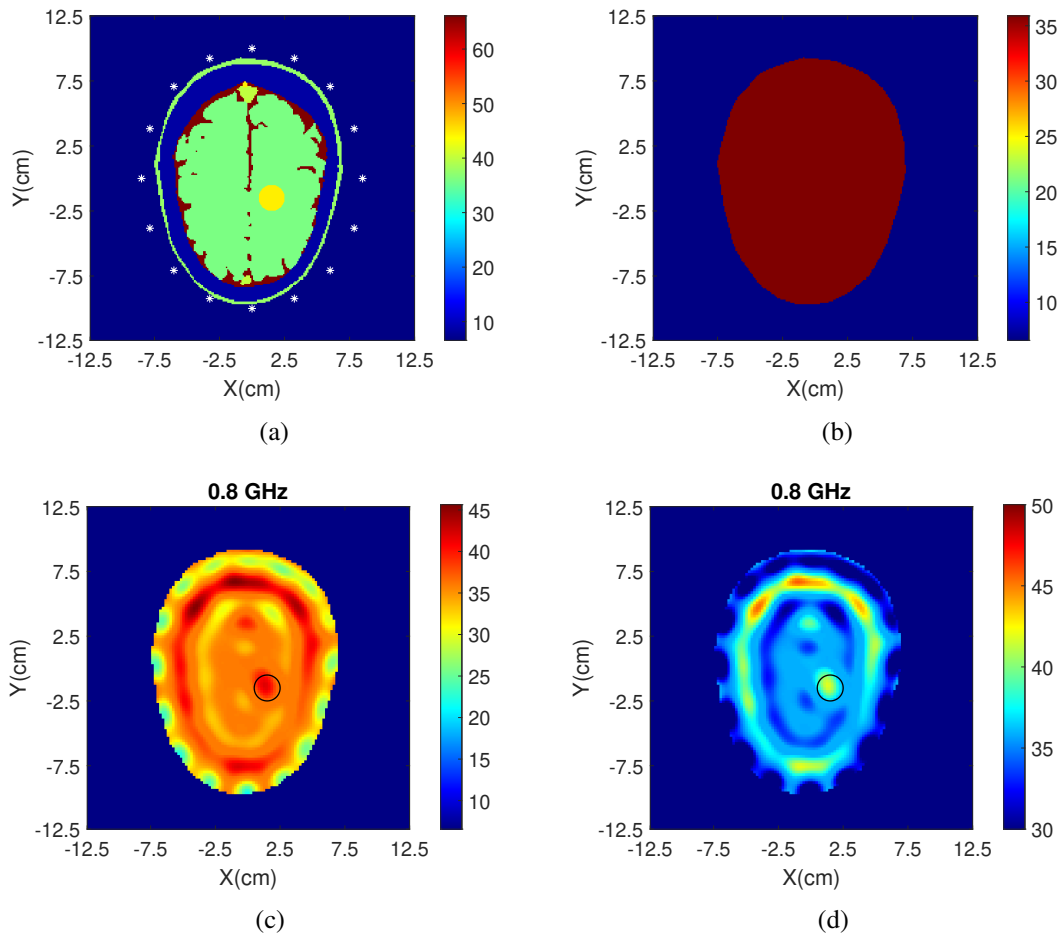


Figure 4.17: Reconstruction results of ϵ_∞ of the head without grey matter at 0.8 GHz: (a) ground truth, (b) initial guess, (c) reconstruction, (d) reconstruction with changed colour bar.

As the area of the grey matter is large, it is not easy to reconstruct the whole model with such a complicated configuration with zero knowledge. To this end, a simplified model is examined that changes grey matter to white matter, shown in Fig. 4.17(a). When only the boundary of the head is given as in Fig. 4.17(b), the initial start for the reconstruction corresponds to homogeneous white matter. To deal with the increased non-linearity, 16 antennas placed in an ellipse with a long axis of 100 mm and a short axis of 85 mm are

used to collect more information. As can be seen from the reconstruction results in Fig. 4.17(c) and Fig. 4.17(d) where the colour bar is changed to show the results better, both the blood target and the boundary of the brain are reconstructed.

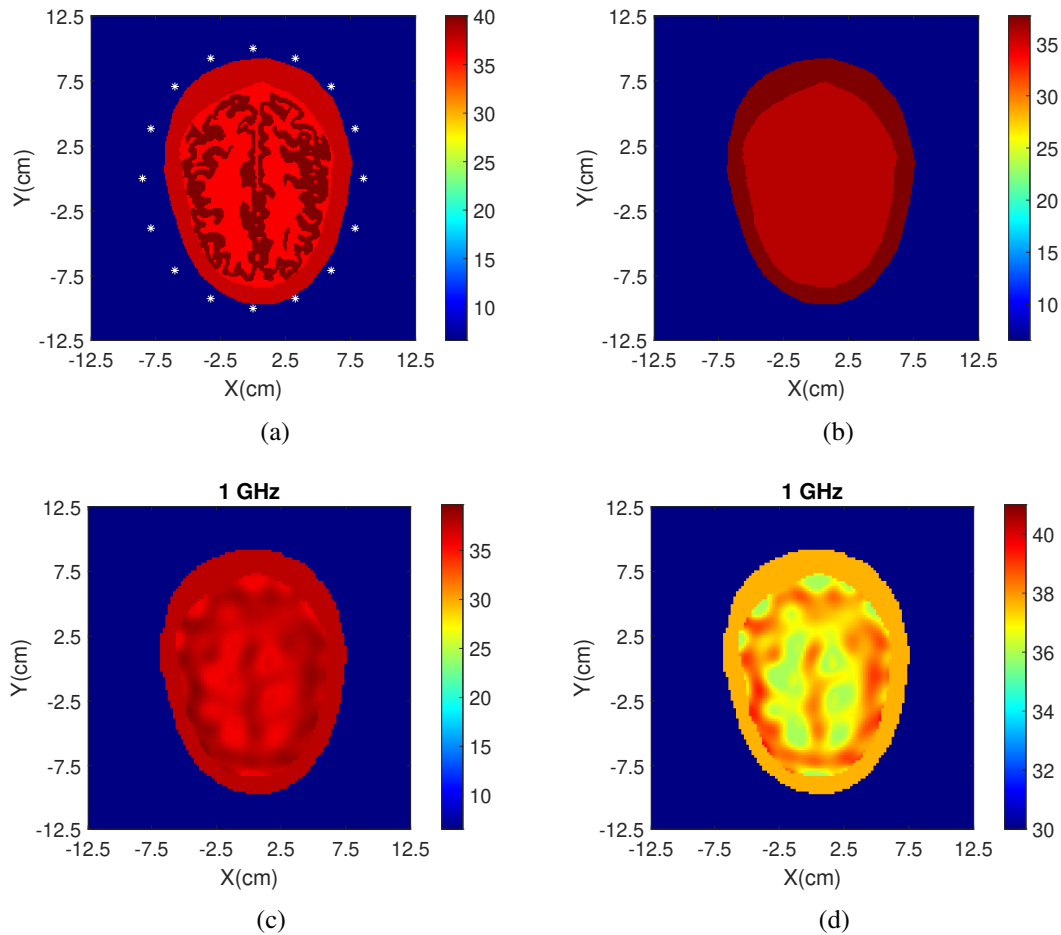


Figure 4.18: Reconstruction results of ϵ_∞ of the three-layer head at 1 GHz: (a) ground truth, (b) initial guess, (c) reconstruction, (d) reconstruction with changed colour bar.

As replacing grey matter with white matter is not realistic and only served as a benchmark test, another examination has been performed to investigate whether a simplified head model that includes both white and grey matter can be reconstructed. To this end, a three-layer phantom (skin, white matter, and grey matter) and two different models as the initial guess are used, shown in Fig. 4.18 and Fig. 4.19. For all the following reconstruc-

tions, 16 antennas placed in an ellipse are used, the same as before. The original ϵ_∞ of this model is shown in Fig. 4.18(a). The first reconstruction is performed when the skin layer is known and the inner brain is set as white matter, with the initial guess shown in Fig. 4.18(b). The grey matter is successfully reconstructed, as shown in Fig. 4.18(c) and Fig. 4.18(d).

Moreover, a second reconstruction of the same model in Fig. 4.18(a) has been performed, but with less prior information, the same as in Fig. 4.17(b) where only the boundary of the head is known. Reconstruction results are shown in Fig. 4.19. The grey matter is again reconstructed but with lower accuracy, which is anticipated due to the loss of prior information in the initial guess.

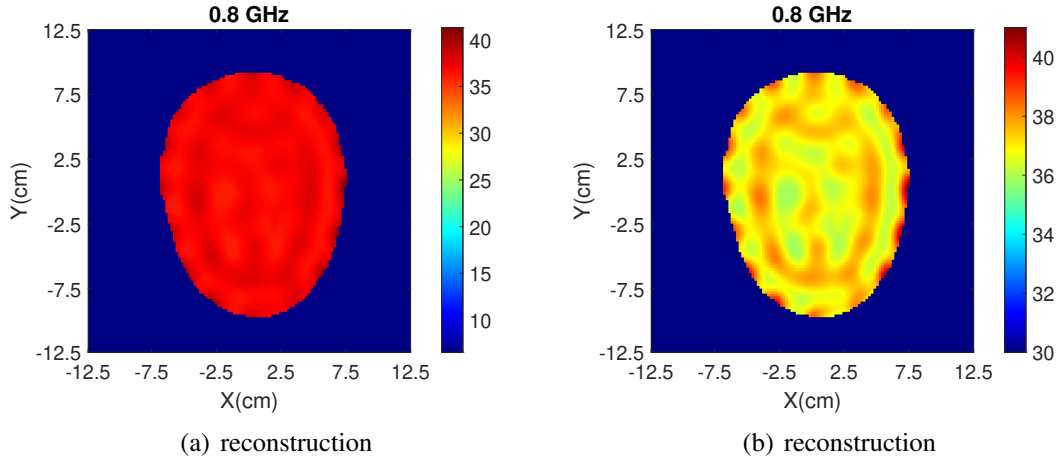


Figure 4.19: Reconstruction results of ϵ_∞ of the three-layer head at 0.8 GHz: (a) reconstruction, (b) reconstruction with changed colour bar.

In addition to these tests, reconstructions are performed at different frequencies, and the reconstruction results at adjacent frequencies also show similar images. In summary, when only the boundary of the head is known, the results are not convincing due to the non-linearity of the problem. A possible approach to improve reconstruction quality is to break down the reconstruction process into two steps, with the first aiming at recon-

structing a more accurate initial guess that can enable a more accurate reconstruction in the second step.

4.5.2.2 Reconstruction with CST data

Based on the results of the FDTD simulation, CST simulations are performed as well to investigate further the possibility of head imaging (comparisons of 2-D and 3-D reconstruction are presented later in Chapter 5). A reduced model of the Zubal head phantom 3.3 is used as WT without grey matter. Two cases in which the cerebrospinal fluid (CSF) layer is absent or present are considered to assess the influence of this high permittivity layer (NT for both cases is the same, where grey matter and CSF are removed).

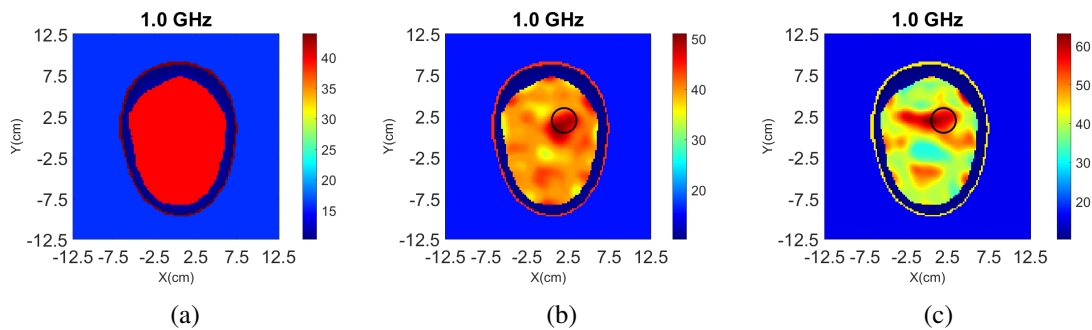


Figure 4.20: Reconstruction results of real part of permittivity of the Zubal head phantom at 1.0 GHz when the grey matter is removed: (a) initial guess, (b) reconstruction when CSF is not included in WT, (c) reconstruction when CSF is included in WT).

The initial guess and reconstructions of the two cases at 1.0 GHz are shown in Fig. 4.20. Compared to the reconstruction results of the FDTD simulation, the noise increases as the CST simulation more closely resembles real scenarios with the realistic antenna and model structure. The target is detected for both cases, however, the shape of the target in the second case is twisted due to the unknown CSF layer. This shows that the impact of the CSF layer is not that significant. Further investigations have also been compared with the 3-D version of the algorithm in Chapter 5.

4.5.3 Experimental data reconstructions

4.5.3.1 Cylindrical models

Reconstructions of the data obtained from the experimental system are performed using the multiple frequency approach (0.5 GHz – 0.8 GHz – 0.9 GHz – 1.0 GHz) with 20 DBIM iterations for the scenario where one or two cylindrical targets are placed at (∓ 2 cm, ± 2 cm) with radius $\rho = 1.5$ cm, shown in Fig. 4.21. The system configuration is the same as before, and the radius of the reconstruction domain is $\rho_r = 5$ cm. Both cases have detected the targets, and the reconstruction value is close to the true value of pure water, though the noise exists and there are artefacts near the boundary of the reconstruction area that are caused by reflections of the plastic tube.

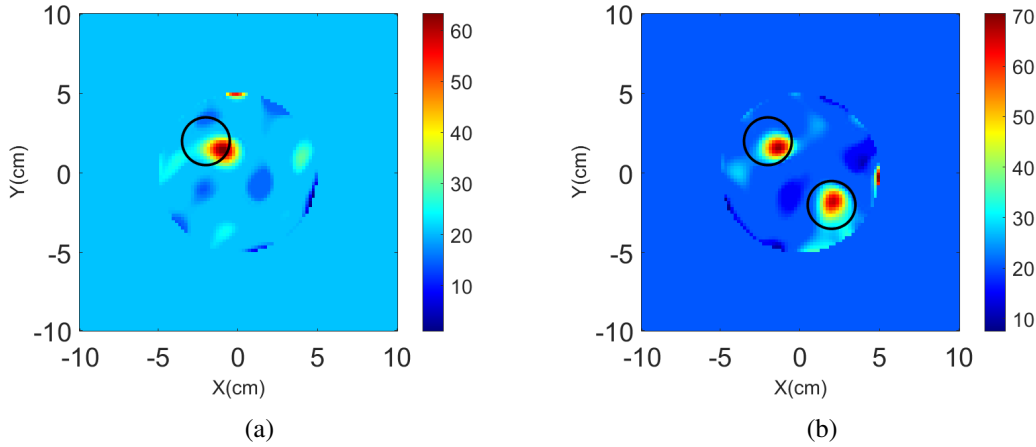


Figure 4.21: Reconstruction images of real part of ϵ_r of the cylindrical targets using multiple-frequency approach: (a) single target, (b) two targets.

Reconstructions are performed without using the Debye model, with the real and imaginary parts of the relative permittivity, shown in Fig. 4.22, where the same multiple-frequency approach is used. The reconstruction images have similar noise positions. The values are slightly different since the matrix size is smaller than the Debye model, which

is $2M \times 2N$.

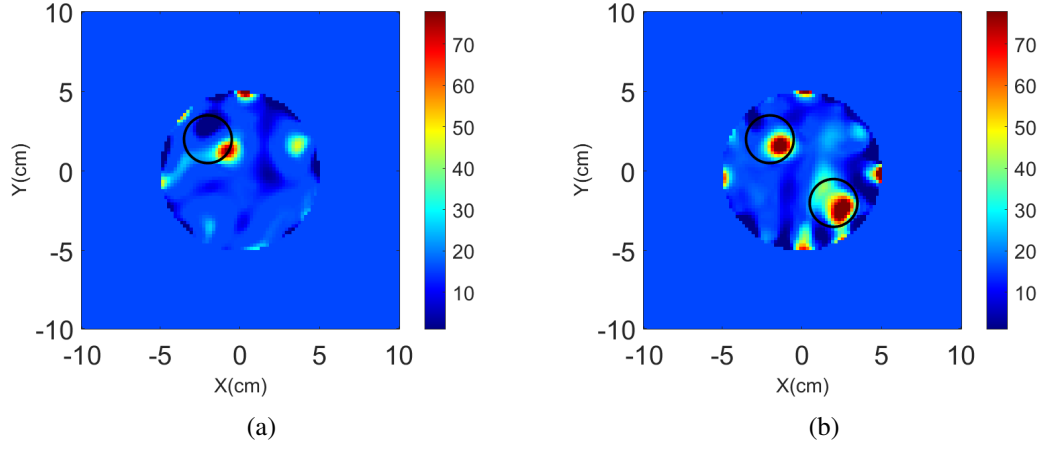


Figure 4.22: Reconstruction images of real part of ϵ_r of the cylindrical targets using multiple-frequency approach: (a) single target, (b) two targets.

4.5.3.2 Experimental brain phantom

Regarding the brain phantom used in the experimental system as shown in Fig. 3.4 and Fig. 3.5, experiments have been performed with the eight-antenna array placed at different heights (with the middle case shown in Fig. 4.23). The antenna ring is placed in an ellipse near the bottom, 4 cm higher near the middle (named EXP-b), and another 4 cm higher near the top. The axes of the antenna ring are 17 cm and 12.5 cm. Moreover, another case (EXP-bII) in the middle where the antenna is moved closer to the phantom has been performed, since the ellipsoid in the middle has smaller axes, which are 14.8 cm and 11.0 cm.

Reconstruction, when the antenna ring is placed near the bottom, is shown in Chapter 5, which is compared to the 3-D reconstruction. Reconstructions of EXP-b and EXP-bII when the antenna ring placed near the middle of the phantom is presented in Fig. 4.24 and the Debye parameters used are $\epsilon_\infty = 20$, $\Delta\epsilon = 20$ and $\sigma_s = 0.147$. EXP-bII has more

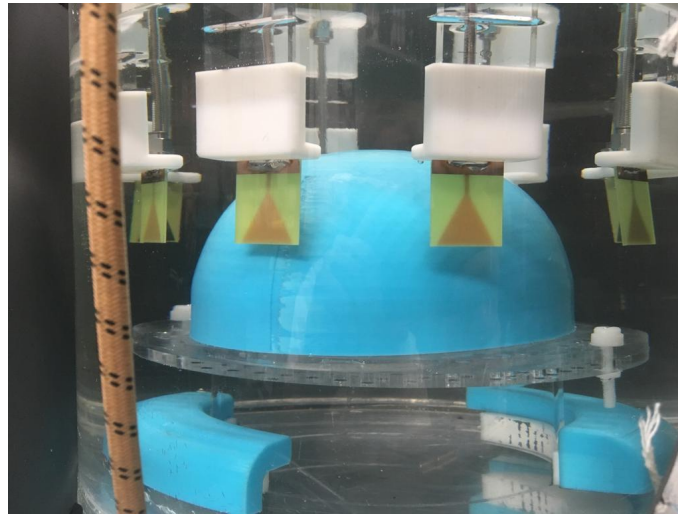


Figure 4.23: Brain phantom inside tank with antenna ring in the middle.

noise compared with EXP-b, and the target is hard to distinguish from the artefacts.

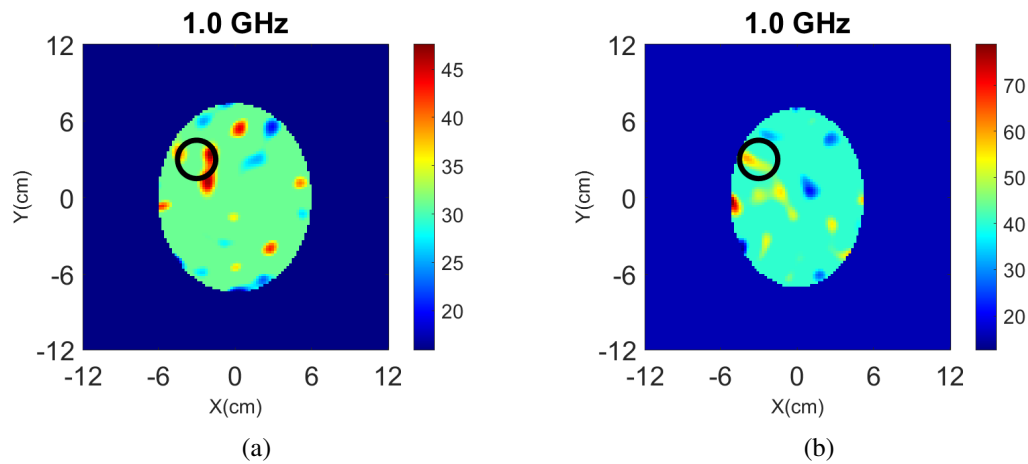


Figure 4.24: Reconstruction images of real part of ϵ_r of the experimental brain phantom: (a) EXP-b, (b) EXP-bII.

Reconstructions are also performed when the antenna ring is placed near the top of the brain phantom. However, the results fail to detect the target as a result of the fact that the curvature of the surface reflects signals into the air which are not captured by the antenna.

To investigate the influence of the initial guess used in reconstructions, the Debye

parameters of the brain are changed to $\epsilon_\infty = 35$, $\Delta\epsilon = 10$ and $\sigma_s = 0.147$. This depends on the fact that the Debye parameters are obtained by curve fitting, and discrepancies exist between the obtained and actual values. Also, since a fixed relaxation time τ is used for all materials, there should be further variation of the properties of the material. As shown in Fig. 4.25(a), the reconstructed target has a better shape, and the noise appears in similar positions.

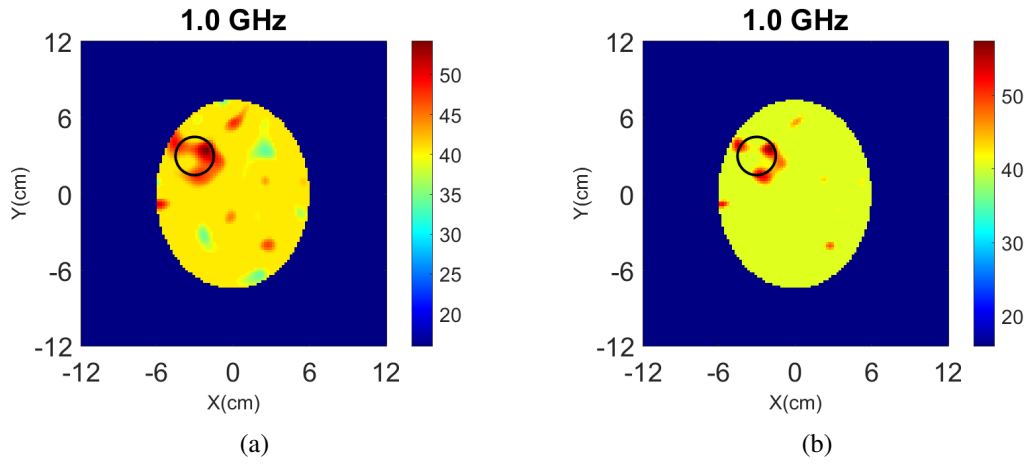


Figure 4.25: Reconstruction images of real part of ϵ_r of the experimental brain phantom with modified initial guess: (a) original, (b) with constraints.

Based on the results, hard constraints are imposed to limit the reconstructed values assuming that prior information is known that the materials inside the brain have higher values than the preset values, *i.e.* the reconstructed values hold conditions that $\epsilon_\infty \geq 35$, $\Delta\epsilon \geq 10$ and $\sigma_s \geq 0.147$. The reconstruction has been improved by the constraints, which shows less noise and higher reconstruction values, and can help to highlight the target.

However, it is hard to have an accurate estimate of the region to be investigated in practical scenarios, and only a coarse constraint with known knowledge can be used. If no prior information is known, only the physical constraint can be used, where $\epsilon_\infty \geq 1$, $\Delta\epsilon \geq 0$ and $\sigma_s \geq 0$.

4.6 Conclusion

In this chapter, the performance of the proposed FEM-based DBIM is evaluated and compared with the FDTD-based DBIM, which shows similar reconstruction positions of the target. The different inverse solvers are compared for both approaches, and FISTA shows the best performance. The FDTD-based DBIM with FISTA is chosen as the main approach, considering its easy implementation. Moreover, the influence of the initial guess of head imaging is studied in the Zubal head imaging scenario.

Chapter 5

Three-dimensional Microwave Head Imaging Analysis Using GPU Accelerated FDTD

5.1 Introduction of 3-D head imaging

This chapter focuses on the implementation of the 3-D GPU-based FDTD method used as the forward solver and application of the proposed 3-D DBIM method with FISTA as inverse solver to head imaging scenarios. Relative to the 2-D FDTD method used for TM wave simulation, the 3-D FDTD method simulates significantly increased size for the full-wave propagation, and it is computationally expensive and time-consuming. Moreover, iterative solvers such as the DBIM require to solve one 3-D direct scattering problem at each iteration, which can be computationally prohibitive. Therefore, an efficient implementation of the 3-D forward solver is in need to reduce time cost and improve efficiency.

Semi-analytical approaches [74], central processing unit (CPU) parallelization [61] or GPU implementation [121], [141] can be used to tackle this problem. CPU parallelization can also model 3-D MWI forward solvers efficiently with GD type inverse solvers as in [61], where FEM was combined with the CSI method to image an experimental breast phantom, and in [142], which uses FDTD as the forward solver for reconstructing a weak scatterer. The latter is implemented on a parallel Linux cluster with a 20-core CPU and a running time of 1 hour for each iteration is required.

For microwave head imaging, studies have analysed scattering from 3-D head models using FDTD [143] or FEM [144], and the fast Fourier transform (FFT) -based volume integral equation (VIE) method [145]. Most imaging algorithms are 2-D with only a few papers presenting 3-D reconstructions. For example, a 2-D GN-type method using S-parameters for inversion has been proposed and tested with an experimental SAM phantom [146]. A frequency-domain beamforming imaging algorithm with Bessel function has been applied to qualitative imaging of a realistic human head in 2-D [147]. This proposed method has been further applied to 3-D head imaging using a wearable EM cap with 16 planar antennas [148] and compared with 2-D results obtained by the polar sensitivity encoding method [149] that works on the principle of encoding S-parameters. A GN-type algorithm using the open-source FreeFEM++ solver has been implemented for imaging a numerical head phantom, which solves the inverse problem by considering five “sub-problems” of cross-sections in parallel across five rings of the antenna array [150]. Recently, an FEM-based and FDTD-based iterative algorithm have been implemented on a single GPU card with Tikhonov regularisation and a GD inverse solver [151]. This work has performed 2-D and 3-D reconstructions with a numerical and an anthropomorphic mannequin head phantom, using a matching medium with permittivity comparable to the brain material. 3-D imaging has also been proposed in [68], which combined FEM with TSVD for linear inversion.

Compared with 2-D head imaging presented in the previous chapter, 3-D imaging can use a more realistic simulation model with full geometries that resemble the real scenarios and provide views of the third dimension for the analysis of vertical materials distribution. However, the complexity of the 3-D structure of the head model increases significantly, leading to increased unknowns and nonlinearity.

In this chapter, reconstructions of MW head imaging are performed with the help of

a 3-D DBIM algorithm. This allows to test performance for more realistic scenarios, where weak target responses are captured by a limited number of antennas surrounding the head in a 3-D array. Therefore, an in-house GPU-based 3-D FDTD forward solver is implemented, which enables a computationally efficient 3-D implementation of the proposed DBIM-FISTA. By optimising the FDTD code specifically for this application, a more computationally efficient implementation is achieved than previous work [53], [113] which used a GPU-based platform Acceleware [152] to perform MWT reconstructions of numerical breast phantoms of varying tissue density. This 3-D FDTD implementation has also been given to another group from Politecnico di Torino, who have implemented it on the field-programmable gate array (FPGA) with increased efficiency using an efficient blocking method to reduce the data transfer time between external and local memories.

The proposed 3-D DBIM-FISTA algorithm in Chapter 3 is applied with the simplified scalar Green's function, which assumes a single electric field component transmission by the linearly polarised antenna. To test the validity of the scalar approximation, reconstruction results using this approximation are compared with reconstructions using the vectorial Green's function, which considers all three electric field components inside the reconstruction domain. Importantly, the results show that the scalar 3-D approximation leads to almost identical results with the vectorial implementation.

The algorithm is tested on different reconstruction scenarios with the MRI-based Zubal head phantom [133] and is validated with an experimental brain phantom. Beyond that, the benefits of imaging in 3-D is examined by comparison with 2-D implementations for challenging target locations and limited prior information of the head's structure. To this end, a cross-sectional axial slice from the 3-D brain model is used, and reconstructed images are compared for this slice using the 2-D and 3-D algorithms.

5.2 Implementation of the 3-D FDTD-DBIM-FISTA algorithm using GPU

5.2.1 3-D FDTD on GPU with CUDA

As a grid-based method, the fields of FDTD are updated at each time step, and the values at the current time step are only related to the values at the previous time and independent from the values at the same time step. Moreover, the update at each time step of E_x , E_y and E_z are independent from the others, which is same to H_x , H_y and H_z . Therefore, FDTD is suitable for parallel computing, and each voxel point of the FDTD discretisation can be viewed as a single thread.

The GPU is specialised hardware, which is more efficient than the CPU for highly parallel computations and contains large blocks of threads. The GPU has more transistors compared with the CPU, which helps process more data simultaneously and reduce access latency, as shown in Fig. 5.1 [153].

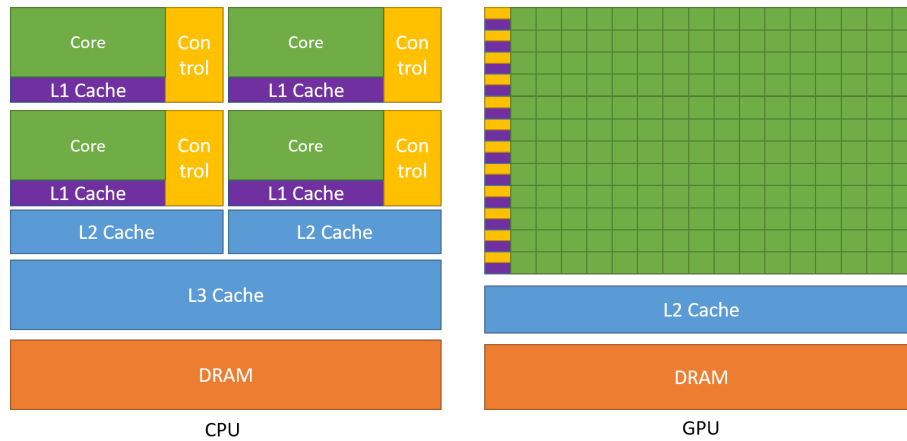


Figure 5.1: CPU and GPU structure. (source: <https://docs.nvidia.com/cuda/cuda-c-programming-guide/index.html>)

A general purpose parallel computing platform of GPU that leverages the parallel

computing cards of NVIDIA GPUs in a more efficient way was introduced by NVIDIA, named CUDA [153], which allows developers to use programming languages such as C/C++. Each NVIDIA GPU device has several streaming multiprocessors (SMs). A CUDA program could execute on multiprocessors and each multiprocessor can schedule blocks of threads as in Fig. 5.2. Depending on the specification of the used GPU device, blocks can be allocated on demand and better used for programs.

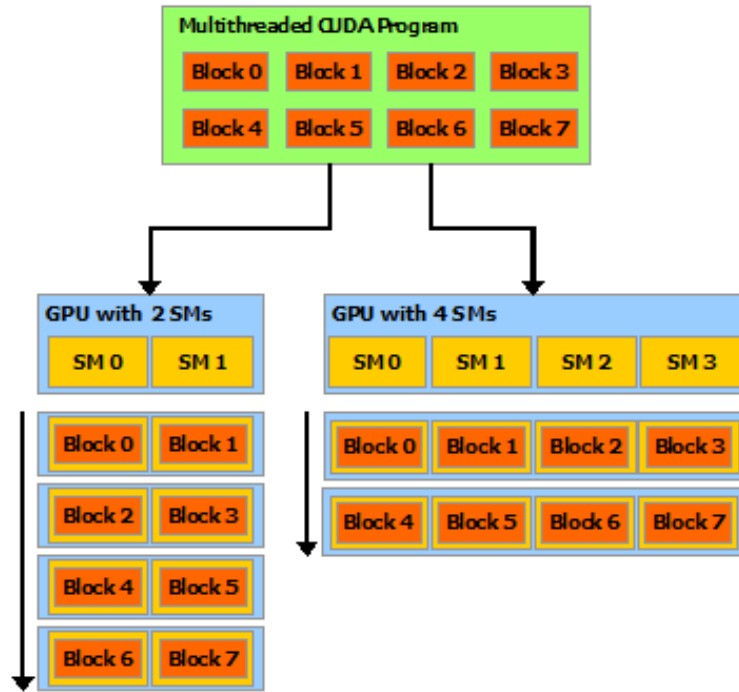


Figure 5.2: CUDA program configuration. (source: <https://docs.nvidia.com/cuda/cuda-c-programming-guide/index.html>)

The CUDA toolkit is used to accelerate the FDTD algorithm in GPU as a forward solver for ISP, with a similar implementation to [154], which focused on modelling radio frequency (RF) wave interactions in high-field MRI however. During the FDTD process for wave simulation, the electric fields and magnetic fields are required to be updated, of which each can be viewed as a kernel (function) on GPU. The kernel is executed as a grid of blocks of threads in GPU, whose number can be adjusted based on the used

GPU platform. By computing the blocks of threads simultaneously, the computational efficiency can be significantly improved.

For an NVIDIA device, the typical maximum number of threads for each block is 1024, which means each block can run 1024 threads simultaneously at most. The number of threads for each block should be set to a multiple of 32 as the working unit in the GPU is a warp, which is a set of 32 threads [153]. Otherwise, the program could waste cycles and lose efficiency. Thus, a 2-D block with size $32 \times 32 = 1024$ is set to make full use of each block. Similarly, a 2-D grid in GPU with size $\frac{I_{\max}}{32} \times \frac{J_{\max}}{32}$ is used for each kernel, E_i ($i = x, y$ or z) for example, and the loop inside each kernel for updating the fields is in the following structure in Algorithm 2,

Algorithm 2 Electric field update on GPU.

```

 $ti \leftarrow blockIdx.x * blockDim.x + threadIdx.x$ 
 $tj \leftarrow blockIdx.y * blockDim.y + threadIdx.y$ 
if  $ti < I_{\max}$  and  $tj < J_{\max}$  then
  for  $tk \leftarrow 1$  to  $K_{\max}$  do
     $E_i[ti + tj * I_{\max} + tk * (I_{\max} * J_{\max})] \leftarrow UpdateE_i$ 
  end for
end if

```

where I_{\max} , J_{\max} and K_{\max} represent number of voxels for the x , y , and z –dimension, respectively.

The flowchart of the 3-D FDTD algorithm is shown in Fig. 5.3. To reduce computational time and interaction time between GPU and CPU, most of the FDTD functions are run on GPU (kernels), including the source update. The environment of this implementation is CUDA 10.2 and Visual Studio 2015 with Intel® Xeon® CPU E5-2640 v3 @ 2.60GHz and GPU Tesla K20c with 5 GB memory. The GPU Tesla K20c has 13 SMs, and each has at most 2048 threads. In total, 13×2048 threads can be run simultaneously.

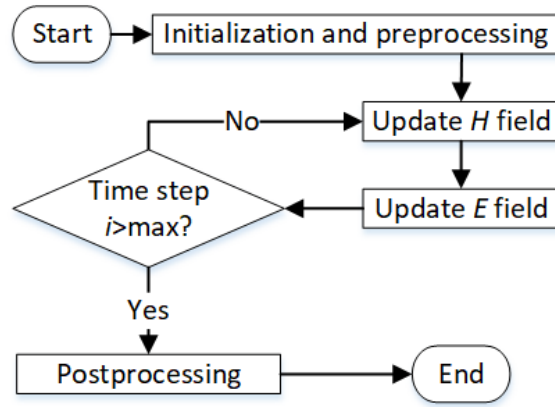


Figure 5.3: Flowchart of the FDTD process.

5.2.2 3-D DBIM-FISTA using GPU based on MATLAB

This algorithm is designed to use the high performance of GPU without changing the MATLAB-based DBIM code to take advantage of MATLAB's capability for matrix computing. To this end, the 3-D FDTD algorithm is implemented in C++ with CUDA and then incorporated it with MEX functions in MATLAB, which is also used to implement the FISTA inverse solver. MEX functions are powerful functions in MATLAB that can build programs using other languages rather than MATLAB, such as C++/C. The above-mentioned environment is used with MATLAB 2020 to connect the different language implementations.

At each DBIM iteration, MATLAB starts initialisation, and the FDTD variables are first allocated space on GPU after initialisation by MEX functions. Therefore, all FDTD-related variables are stored on GPU memory to reduce time cost. Next, the FDTD part on GPU starts to simulate the wave propagation for each transmitter antenna, and the calculated data to be used in DBIM is transferred back to MATLAB via MEX functions, which can be used directly by the MATLAB code. Finally, the ISP linear system is built and solved by the inverse solver FISTA to obtain the reconstructed values.

Recall that the discretisation size for FDTD is defined as $\Delta h = \frac{\lambda_f}{n_d}$, where λ_f is the wavelength and n_d is the discretisation step. To ensure accuracy and reduce numerical dispersion, $n_d > 10$ is required. While Δh is 30 mm in air, its value inside the brain is defined by a much smaller wavelength ($\lambda_f = \frac{300}{\sqrt{\epsilon_r}}$), requiring a greater n_d and a smaller Δh . Therefore, a cubic grid voxel size of 2 mm for each dimension is selected in all 2-D and 3-D FDTD simulations. This value can balance accuracy and computational burden. For example, using a 2 mm vs. a 1 mm cubic voxel side results in field values with a mean relative difference of 1E-3 but requires an eight times bigger grid. The time step Δt defined as $\Delta t = \frac{\Delta h}{2c}$, where c is the speed of EM wave, will also increase for a higher resolution model and lead to more iterations. In the considered simulations, the iteration number ranges between 1000-2000.

To compare computational burden vs. grid resolution, the running time is calculated for a two-antenna system using 2 mm, 1.5 mm, and 1 mm size cubic voxels. These are acceptable resolutions for a grid with a physical volume of about 300 mm \times 300 mm \times 200 mm, which is required for the inverse problem with the numerical head phantom. Resolutions of 0.5 mm or lower exceed the maximum memory of GPU, and they also increase errors and instabilities for the inverse model [118]. The size and running time corresponding to these different grids when 16 antennas are used as transmitters and receivers is shown in Table 5.1.

Table 5.1: Average running time for each antenna.

Resolution	Grid size	Time
2 mm	150 \times 150 \times 100	31 s
1.5 mm	225 \times 225 \times 150	59 s
1 mm	300 \times 300 \times 200	176 s

As this implementation is specific for the inverse problem at hand, it is more than 30% faster than the previously used codes implemented with the commercial software package

Acceleware, which is designed for general GPU-based FDTD simulations. Moreover, the mean absolute error of the fields received by each antenna calculated by Acceleware and this new code is less than $1e-8$, which shows this implementation is as accurate as Acceleware's. The running time for FISTA for the above-mentioned case with 2 mm resolution where the size of A is 240×449949 at each DBIM iteration is around 5–15 s depending on the number of FISTA iterations. This number typically ranges from 20–100, i.e. for each iteration, the average running time is around 0.2s.

As noted earlier, the 2-D DBIM-FISTA algorithm [117] with the TM mode of EM wave propagation is applied to compare performance with the 3-D implementation. The 2-D code is implemented in MATLAB without GPU acceleration for the FDTD forward model, which requires approximately 1 second for each of the eight transmitting antennas and a total of 10-20 seconds for each DBIM iteration.

5.3 Assessment of the 3-D reconstruction images

Similar to the assessment of 2-D reconstruction results, contrast and errors such as RMSE can be used to evaluate the quality of 3-D images. However, more artefacts may occur in the reconstruction for 3-D problems due to increased nonlinearity and modelling error between FDTD and CST/experiment. As 3-D images consists of dozens of x-y, y-z, z-x plane results, a simplified way to evaluate them is to focus on the planes located at the target centre position. The reconstruction can be considered as “good”, similar to 2-D reconstructions, when the contrast of the target domain shows much higher average value (more than twice) than that of the other area, except for the area near the reconstruction boundary where reflections from the boundary may cause huge artefacts. Also, the error RMSE can be used as an auxiliary criterion, which is calculated based on the images of xy-slice at the same position of the target centre.

5.4 CST data reconstruction with the Zubal head phantom

5.4.1 Scenarios and reconstructions with the FDTD-DBIM-FISTA

5.4.1.1 Case I where only target is unknown

“Case I” considers the numerical model in Fig. 3.3 immersed inside “infinite” 90%-10% glycerol-water mixture. A cylindrical blood target centred at (20 mm, 20 mm) with $\epsilon_r = 61.1 - 28.4j$, radius $\rho = 15$ mm and height $h = 30$ mm is inserted into the Zubal head phantom. Eight antennas are placed in an elliptical array configuration with semi-major and semi-minor axes equal to 100 mm and 85 mm, respectively. Two CST simulations are performed to obtain the scattered field data, with and without the target, referred as WT and NT, respectively.

The initial guess of the FDTD model for reconstruction is chosen to be similar to the NT case CST model. The reconstruction area inside the brain is a cubical volume with height along the z-axis between [10, 70] mm for the 3-D model. The true dielectric constant values $\Re(\epsilon_r)$ of the numerical and experimental phantoms are shown in Fig. 5.4.

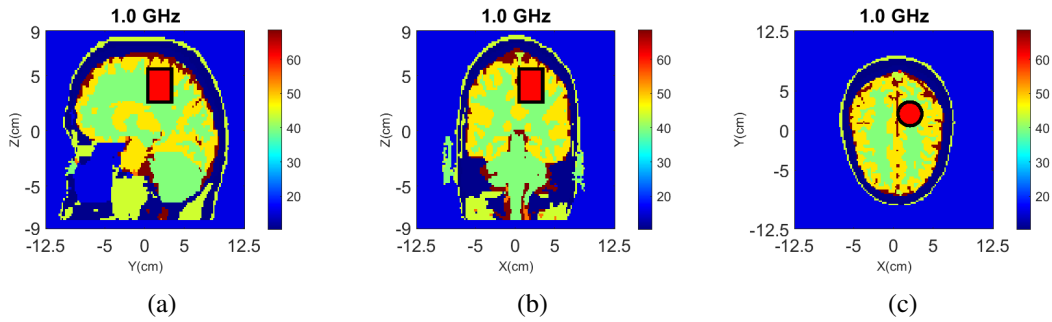


Figure 5.4: Dielectric constant distribution $\Re(\epsilon_r)$ for Case I. Top: (a) y–z slice, (b) x–z slice, and (c) x–y slice for the numerical head model. Bottom: (d) y–z slice, (e) x–z slice, and (f) x–y slice for the experimental phantom.

5.4. CST DATA RECONSTRUCTION WITH THE ZUBAL HEAD PHANTOM

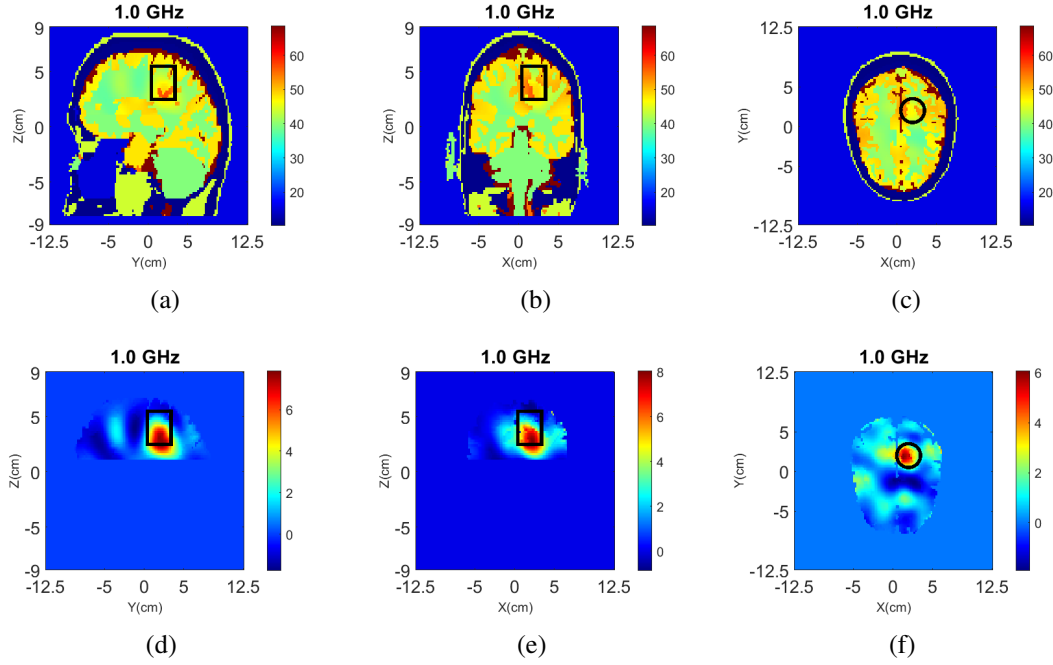


Figure 5.5: 3-D reconstructions with simplified Green's functions for Case I of Fig. 3.3 at 1.0 GHz: (a), (b), (c) relative permittivity $\Re(\epsilon_r)$, and (d), (e), (f) contrast for the y-z, x-z, and x-y slices, respectively. A cylindrical eight-antenna array centred at the target height is used to produce the data.

The 3-D reconstruction results using the simplified Green's function are shown in Fig. 5.5, where the top shows the reconstructed real part of relative permittivity, and the bottom shows the contrast due to the target.

Table 5.2: Reconstruction errors for Case I.

Simulation name	Iteration	RMSE	e_{\max}	RRE
Case I, 3-D	20	3.39	19.38	0.28
Case I, 2-D	20	4.11	20.46	0.72
Case I, 3-D	120	3.21	19.42	0.01
Case I, 2-D	200	3.71	19.03	0.07

Reconstructions are performed using the vectorial Green's function (3.17), and the reconstruction results of the contrast are shown in Fig. 5.6 with errors $\text{RMSE} = 3.65$, $e_{\max} = 20.42$, $\text{RRE} = 0.27$, which are close to the reconstructed values using the sim-

plified Green's function shown in the first row of Table 5.2. This comparison suggests

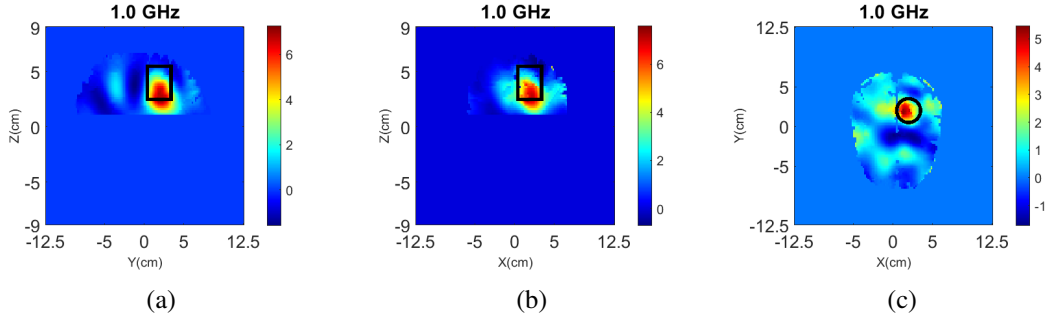


Figure 5.6: 3-D reconstructions, same as Fig. 5.5 but with vectorial Green's function in (3.17), for Case I of Fig. 3.3 at 1.0 GHz. (a), (b), (c) Relative permittivity $\Re(\epsilon_r)$ for the y-z, x-z, and x-y slices, respectively.

that the z-only approximation for the Green's function does not affect the accuracy of the results. Thus, this formulation is sufficient to achieve similar accuracy to the more complete vector formulation of (3.17). To re-enforce this argument, another comparison of the two formulations is performed for a more challenging imaging scenario of Case III.

The target is also detected in 2-D as shown in Fig. 5.7, but the reconstructed values are lower. Inaccuracies in these 2-D and 3-D results can be attributed to the complex

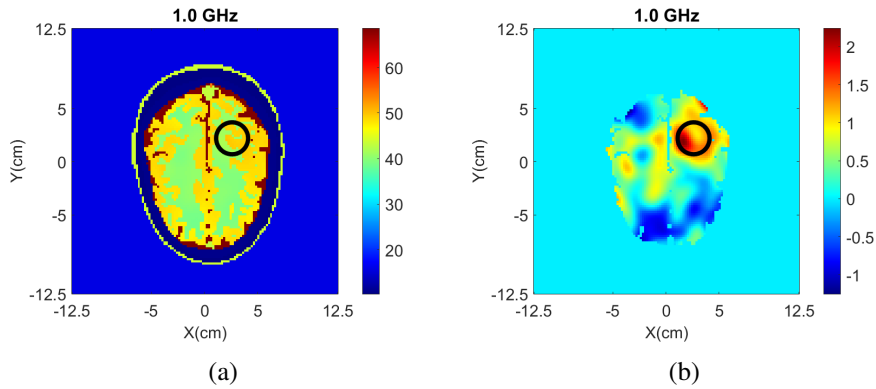


Figure 5.7: 2-D reconstructions of: (a) relative permittivity $\Re(\epsilon_r)$ and, (b) contrast for Case I of Fig. 3.3 at 1.0 GHz.

brain structure, which leads to a highly non-linear scattering problem, and the mismatch

5.4. CST DATA RECONSTRUCTION WITH THE ZUBAL HEAD PHANTOM

between the CST model producing the data and the FDTD forward model of the DBIM-FISTA algorithm. For example, the FDTD solver models the antennas as point sources to avoid the additional computational complexity and much finer resolution required for modelling the full antenna structure, which leads to a model mismatch from the full antenna CST model. Moreover, the models in FDTD and CST have discrepancies in the Debye material properties due to their different computational environments. This includes errors in the head boundary between the CST (or experimental model) and the FDTD solver due to discretisation errors and the coarser resolution used in FDTD.

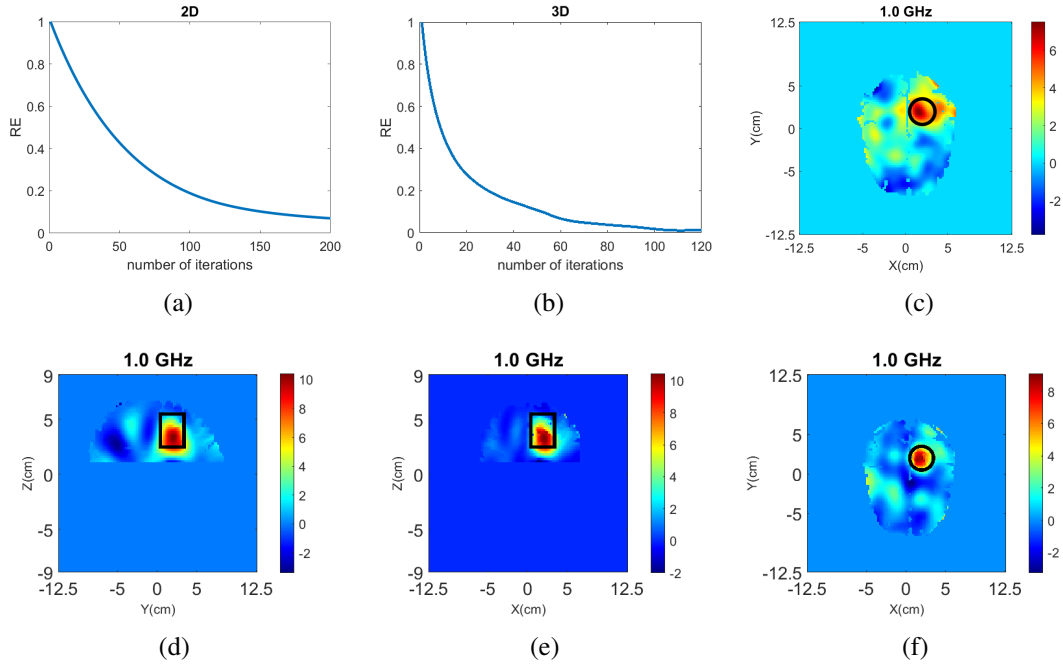


Figure 5.8: Reconstructions of Case I when RRE converges: 2-D with 200 iterations and 3-D with 120 iterations: (a), (b) residual error plot for 2-D and 3-D respectively, (c) contrast for 2-D reconstruction, (d), (e), (f) contrast for the y-z, x-z, and x-y slices of 3-D reconstruction respectively.

To assess whether a fixed number of 20 iterations for both 2-D and 3-D algorithms leads to a fair comparison, reconstruction of Case I is run with a large number of iterations which can ensure that the residual error RRE converges to almost a fixed value, as shown

5.4. CST DATA RECONSTRUCTION WITH THE ZUBAL HEAD PHANTOM

in Fig. 5.8. The numbers of iterations and errors for these cases are given in Table 5.2, and the resulting images are shown in Fig. 5.8.

Relative to the reconstruction results with 20 DBIM iterations, reconstructions after a much greater number of iterations (120 in 3-D, 200 in 2-D) lead to rather modest reductions in the errors in Table 5.2, despite a significant decrease of the data residual RRE. Importantly, the ratio between the 3-D and 2-D RMSE errors for the increased iterations is similar to the 20 iterations case, thereby allowing us to draw conclusions for 2-D vs. 3-D results using this limited fixed number. These observations and the results in Fig. 5.8 suggest that using a fixed number of 20 iterations is sufficient for comparison, although it does not represent complete convergence of the algorithms.

Finally, regarding the influence of a possible head movement which would result in a miss-alignment of antennas between the WT and NT scenario, this issue is examined by performing reconstructions where the antenna position has a 5 degrees difference along the z -plane between the NT case and WT case. The 3D reconstructed contrast of this model is shown in Fig. 5.9, and it suggests that the impact of such a difference does not change performance dramatically though the noise increases.

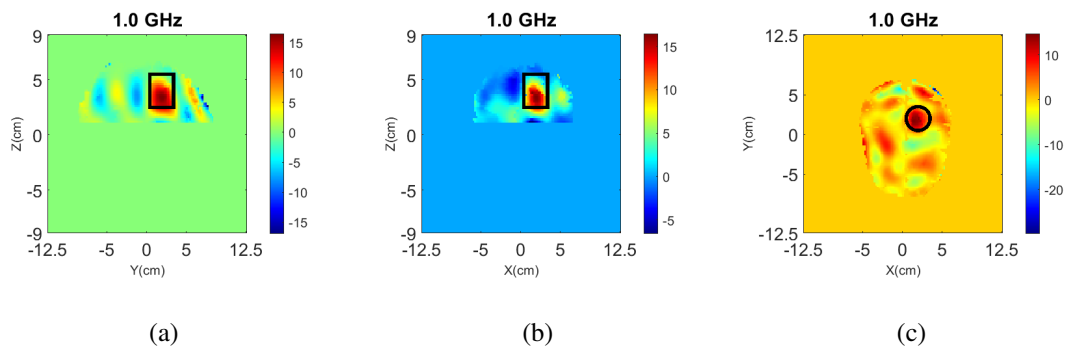


Figure 5.9: Reconstructions of Case I when the antenna position has a 5 degrees difference along the z -plane between the NT case and WT case. Contrast for the y - z , x - z , and x - y slices of 3-D reconstruction, respectively.

5.4.1.2 Case II where limited information is known

To investigate a scenario of limited prior information where only the boundary of the head is known, the model of Fig. 3.3 was filled with white matter only for the NT case. Moreover, taking into account that the dielectric properties of grey and white matter are not very different (see Table 3.1), grey matter is replaced with white matter in Fig. 3.3 to reduce the model complexity [140]. The resulting head model is then used in two WT cases (WT1 and WT2), “Case II.1” and “Case II.2”, which differ by the presence or absence of the CSF layer with $\epsilon_r \approx 68.4 - 44.9j$. Cross-sectional views of the 3-D models for these cases are shown in Fig. 5.10 while the true values of $\Re(\epsilon_r)$ is shown in Fig. 5.11.

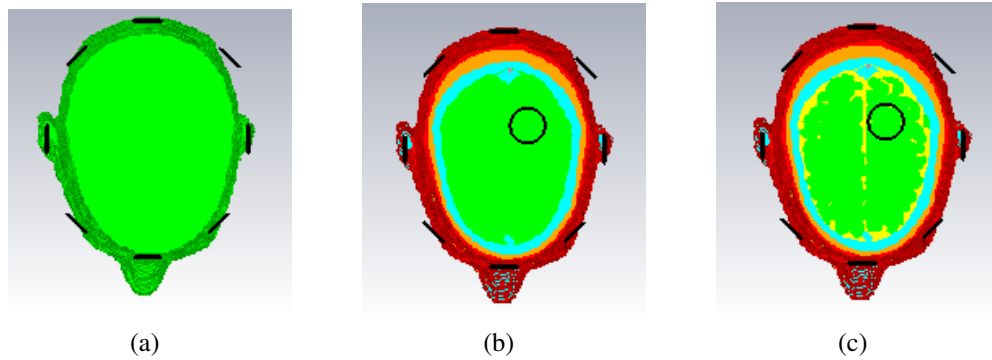


Figure 5.10: Cross-sectional view for Case II.1 and Case II.2: (a) NT model for both cases; (b) WT1 model for Case II.1 with grey matter and CSF replaced by white matter; (c) WT2 model for Case II.2 with only grey matter replaced by white matter.

3-D and 2-D reconstruction results are shown in Fig. 5.12 and Fig. 5.13, respectively, with errors shown in Table 5.3. The target is detected by both 2-D and 3-D algorithms, but there are significant image artefacts due to the skin, fat, and bone tissue regions which are not taken into account in the inverse model. These image artefacts are comparable in 2-D and 3-D, while the contrast in the estimated dielectric properties near the target is quite higher in the 3-D reconstructions. The RMSEs of both algorithms are similar,

5.4. CST DATA RECONSTRUCTION WITH THE ZUBAL HEAD PHANTOM

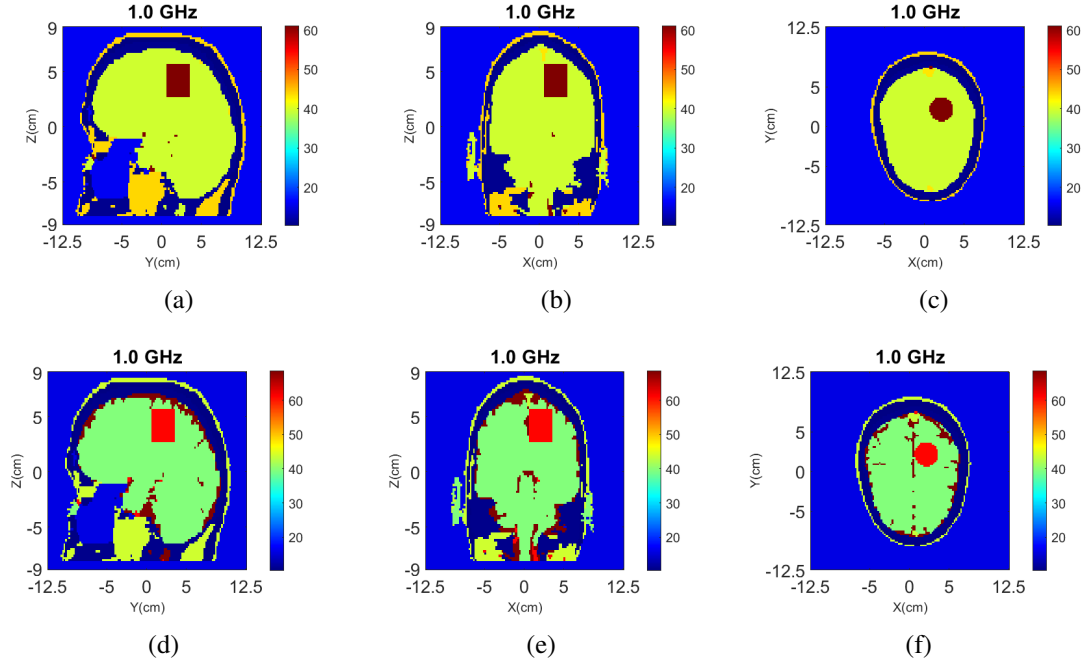


Figure 5.11: True values of $\Re(\epsilon_r)$ of Case II.1 and II. 2 at 1.0 GHz: (a) y–z slice, (b) x–z slice, (c) x–y slice of Case II. 1. (d) y–z slice, (e) x–z slice, (f) x–y slice of Case II. 2.

Table 5.3: Reconstruction errors for Case II.

Case No.	RMSE	e_{\max}	RRE
Case II. 1, 3-D	16.62	46.71	0.19
Case II. 2, 3-D	18.75	62.01	0.51
Case II. 1, 2-D	15.51	22.27	0.16
Case II. 2, 2-D	18.01	21.68	0.50

but the 3-D has much larger e_{\max} values, suggesting that the 3-D algorithm may be more sensitive to limited prior information. Comparing the results of Cases II.1 and II.2, it can be concluded that not including a thin layer with high contrast such as CSF in the inverse model’s initial guess does not have a significant impact on the reconstructions.

5.4. CST DATA RECONSTRUCTION WITH THE ZUBAL HEAD PHANTOM

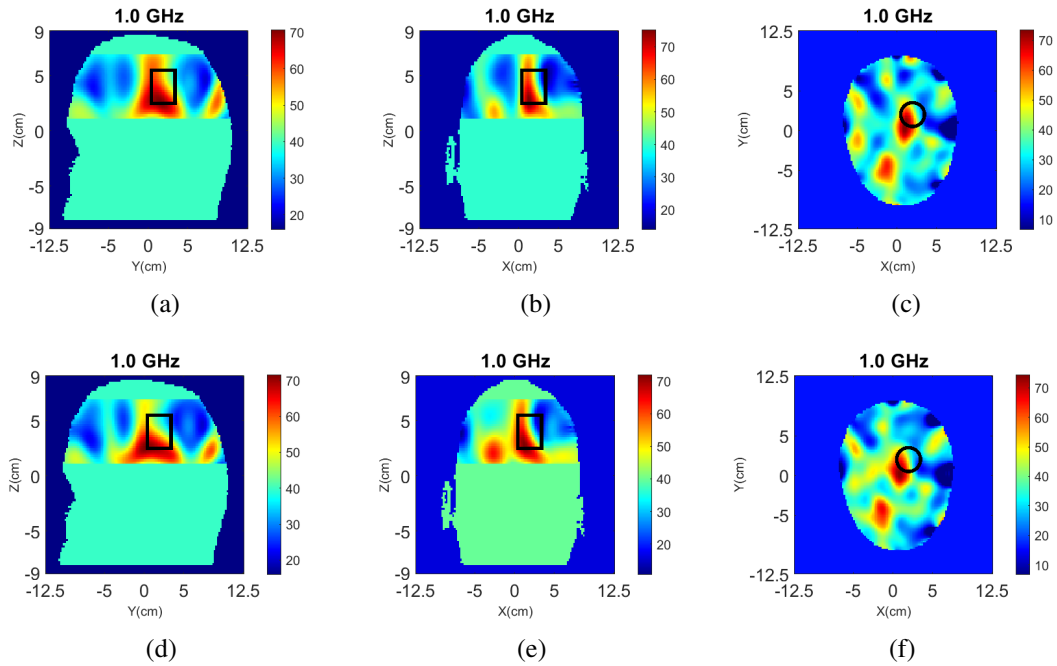


Figure 5.12: 3-D reconstructions of $\Re(\epsilon_r)$ at 1.0 GHz: (a) y-z slice, (b) x-z slice, and (c) x-y slice for Case II.1; (d) y-z slice, (e) x-z slice, and (f) x-y slice for Case II.2.

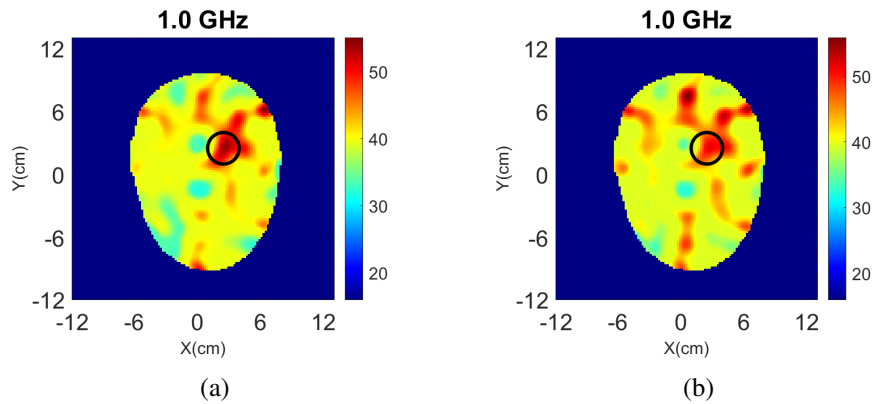


Figure 5.13: 2-D reconstructions of $\Re(\epsilon_r)$ at 1.0 GHz: (a) Case II.1, and (b) Case II.2. A cylindrical eight-antenna array centred at the target height is used to produce the data.

5.4.1.3 Case III where a headband is used with a small target placed at an offset height

Another scenario is considered where a small target is placed between a two-ring array surrounding the model of Fig. 3.3. The head phantom comprises white matter and includes a target at the same x-y position as previously, but with a smaller radius $\rho = 10$ mm and height $h = 20$ mm for the WT case. As the immersion liquid cannot extend infinitely in a practical scenario, a headband of finite dimensions, filled with the immersion liquid and surrounded by air, is considered. The setup is shown in Fig. 5.14. The two rings are placed with an offset in the x-y plane to obtain information from more angles and reduce coupling. The target covers an area between the x-y planes of the two rings only, as shown in Fig. 5.14(a). Different ways of applying the 2-D imaging algorithm to the data by the two-ring array are considered by using: 1) the bottom ring data, 2) the top ring data, and 3) combined data from both rings as if they were on the same plane, effectively creating a sixteen-antenna array for the slice reconstructed in 2-D, which was selected as the slice of the target centre. The head model for the cases considered in this

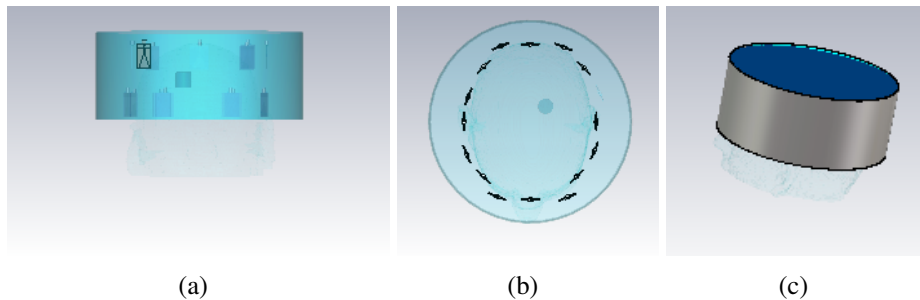


Figure 5.14: (a) Top and (b), (c) side views of the setup used in Section 3.2. A headband is placed at the top of the head phantom, and sixteen antennas are placed in a two ring array inside the headband, with 8 antennas for each ring.

subsection (Cases III.1, 2 and 3) is shown in Fig. 5.15, while the headband used in each case is different. It should be noted that the “homogeneous white-matter” head model of

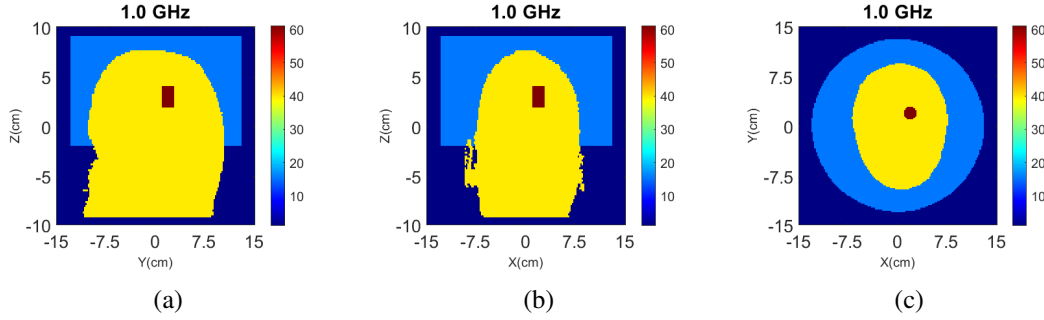


Figure 5.15: True values of $\Re(\epsilon_r)$ of Case III at 1.0 GHz: (a) y-z slice, (b) x-z slice, and (c) x-y slice.

Fig. 5.15 is unrealistic, but it was selected to focus on comparing 3-D with 2-D results of more realistic arrays and smaller targets. To compare the errors of the target domain more clearly, an RMSE in the selected target slice is defined as RMSE-T.

“Case III.1” considers a headband of $\rho = 130$ mm radius and $h = 110$ mm height filled with the glycerol-water mixture. The antennas are very close to the air-liquid interface in all directions (top/bottom/side) for this case, resulting in strong reflections from the interface. The reflections can be taken into account by the 3-D FDTD model along all dimensions, while the 2-D model can only model the x-y boundary. In both models, of course, the wave reflections from the boundary will be different for the realistic CST model relative to its simplified version in FDTD, firstly because realistic antennas have been replaced by simple point sources.

Results from 3-D and 2-D reconstructions are shown in Fig. 5.16. Despite including the interface in the 3-D model, the reconstructed images suffer from strong artefacts near the interface, which suggest that the mismatch between CST and FDTD models is significant. The target is reconstructed to some extent, but it is difficult to detect it with certainty. The 2-D reconstructions fail to detect the target completely regardless of whether data from the top, bottom, or both rings is used. This is not surprising, given that the target is not aligned with any of these rings and that the interface between air and the

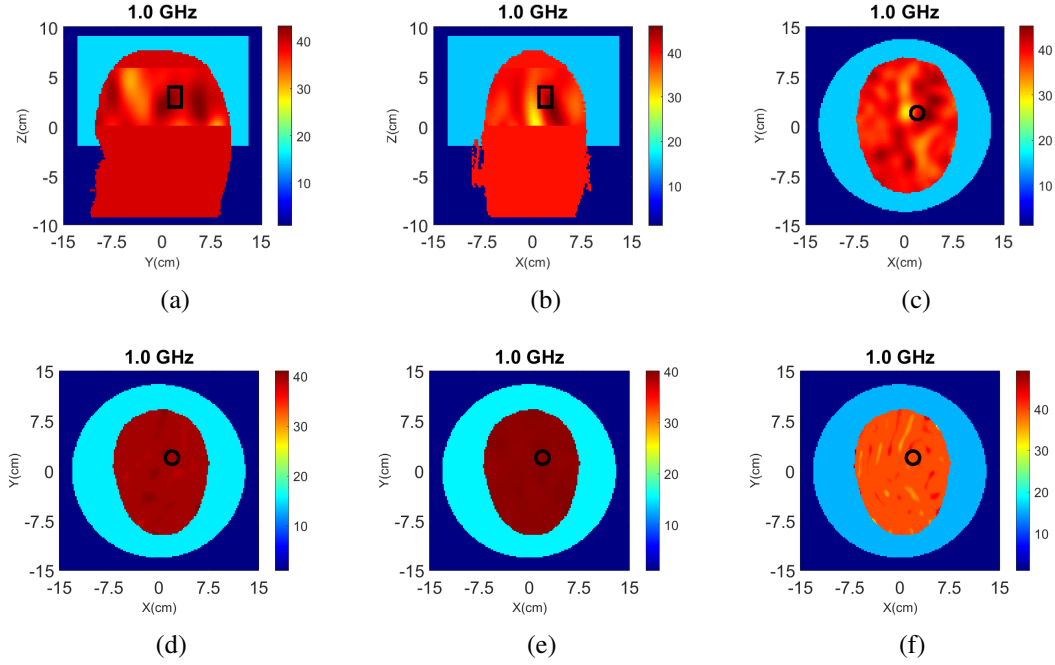


Figure 5.16: 3-D(a)(b)(c) and 2-D (d)(e)(f) reconstructions of Case III.1 at 1.0 GHz: (a) y-z slice, (b) x-z slice, and (c) x-y slice of 3-D reconstructions. 2-D slice reconstructions (d) bottom ring, (e) top ring, and (f) both rings. The headband of Fig. 5.14 is used to obtain the data.

glycerol-water immersion liquid cannot be fully modelled in 2-D.

To examine the impact of this interface and improve detection performance, “Case III.2” considers the same headband as Case III.1, which is now surrounded by an additional layer of absorbing material. The headband layers are as follows: glycerol-water mixture, plastic, absorbing material (ECCOSORB MCS), and a metallic shield. Finally, “Case III.3” uses a larger size ($\rho = 140$ mm and $h = 120$ mm) headband with the same materials as Case III.1. As with the absorbers in Case III.2, increasing the distance between the antennas and the interface with air can reduce the resulting reflections.

Results from 3-D and 2-D reconstructions at 1.0 GHz are shown in Fig. 5.17 and Fig. 5.18 for Case III.2. Note that the colour bar’s range of values in these images is limited to increase the contrast. The 3-D reconstructions show that the target’s location and size

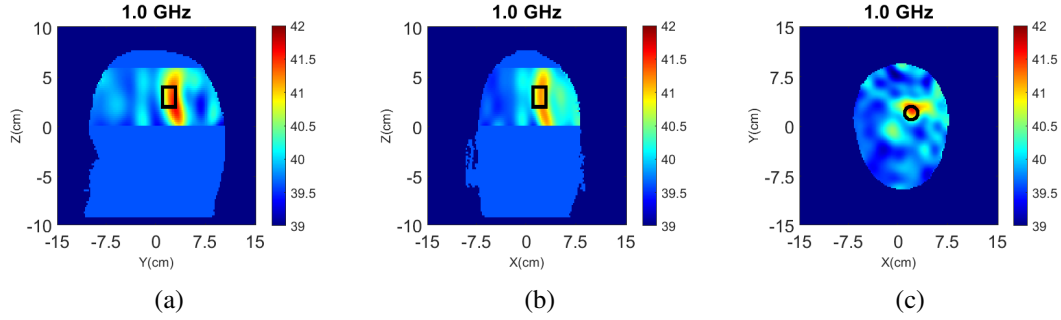


Figure 5.17: 3-D reconstructions of $\Re(\epsilon_r)$ for Case III.2 at 1.0 GHz: (a) y-z slice, (b) x-z slice, and (c) x-y slice. The headband of Fig. 5.14 (with the addition of absorbing material) is used to obtain the data.

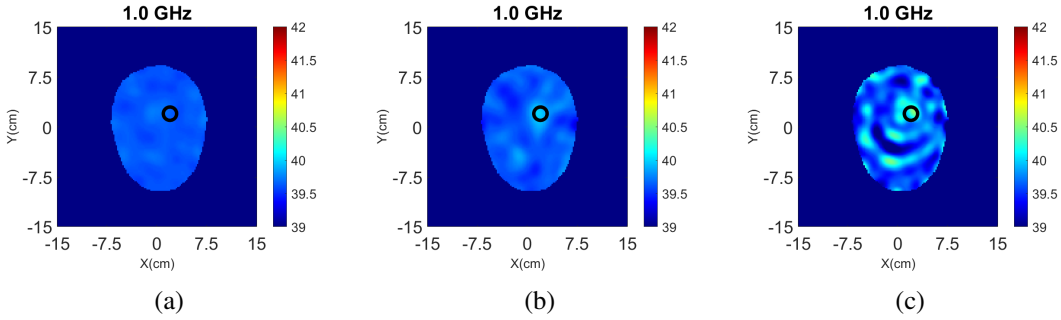


Figure 5.18: 2-D Reconstructions of $\Re(\epsilon_r)$ of Case III.2 for the x-y slice at 1.0 GHz using data from the: (a) bottom ring, (b) top ring, and (c) both rings. The headband of Fig. 5.14 (with the addition of absorbing material) is used to obtain the data.

are detected accurately with the use of the absorbers. The 2-D results, however, fail to distinguish the target from the noise.

Similarly, 3-D and 2-D reconstruction results for Case III.3 are presented in Fig. 5.19 and Fig. 5.20. Detection is improved from Case III.1, as the distance from the interface has been increased, but is less accurate than Case III.2, where the absorbing material was added. Similar to the other two cases, the 2-D imaging results in Fig. 5.20 suggest that the algorithm fails to detect the target in all cases.

The RMSE, RMSE-T, e_{\max} and RRE of Case III.1, 2 and 3 are shown in Table 5.4, where the 3-D reconstructions have a lower RMSE-T for all the three cases. Recon-

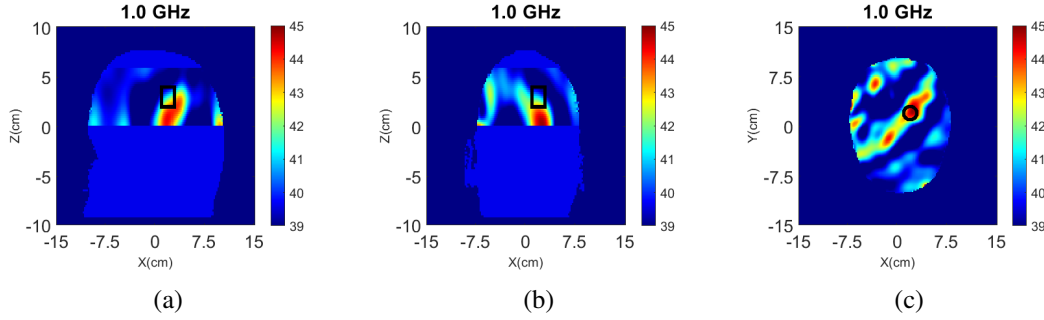


Figure 5.19: 3-D reconstructions of $\Re(\epsilon_r)$ for Case III.3 at 1.0 GHz: (a) y-z slice, (b) x-z slice, and (c) x-y slice. The headband of Fig. 5.14 (with an increased distance between the array and the interface with air) is used to obtain the data.

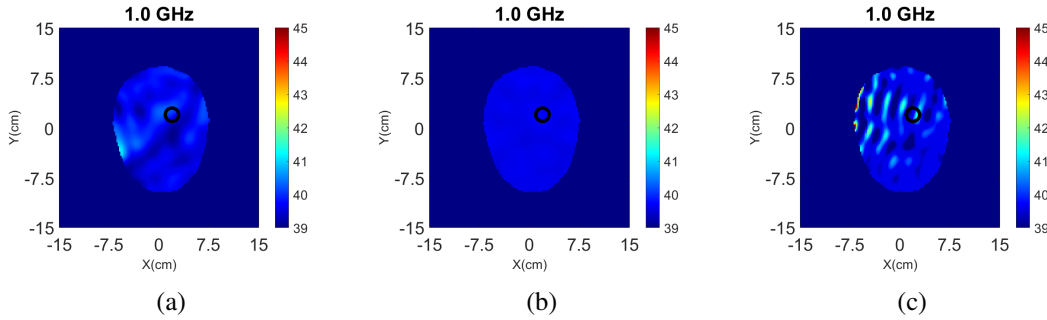


Figure 5.20: 2-D Reconstructions of $\Re(\epsilon_r)$ of Case III.3 for the x-y slice at 1.0 GHz using data from the: (a) bottom ring, (b) top ring, and (c) both rings. The headband of Fig. 5.14 (with an increased distance between the array and the interface with air) is used to obtain the data.

structions of other cases with the vectorial Green's function (3.17) have also been performed, and Case III.2 is shown in Fig. 5.21. The relative errors are $\text{RMSE} = 2.37$, $\text{RMSE-T} = 20.89$, $e_{\max} = 21.08$, $\text{RRE} = 0.62$, which again shows similar reconstruction quality with the simplified Green's function even when the antenna array is placed at an offset height. This comparison confirms that the simplified Green's function does not affect the 3-D reconstruction quality significantly, leading to equally accurate results for the scenarios considered.

Finally, reconstructions are also performed for additional scenarios related to Cases

Table 5.4: Reconstruction errors for Case III.

Case No.	RMSE	RMSE-T	e_{\max}	RRE
III. 1, 3-D	3.05	20.14	22.79	0.57
III. 1, 2-D bot	2.44	21.35	21.49	0.71
III. 1, 2-D top	2.43	21.27	21.40	0.69
III. 1, 2-D both	2.59	21.40	21.48	0.75
III. 2, 3-D	2.30	20.02	20.70	0.70
III. 2, 2-D bot	2.44	21.49	21.44	0.70
III. 2, 2-D top	2.41	21.23	21.15	0.70
III. 2, 2-D both	2.40	21.25	20.92	0.72
III. 3, 3-D	2.57	20.08	21.14	0.47
III. 3, 2-D bot	2.43	21.17	21.59	0.70
III. 3, 2-D top	2.43	21.36	21.40	0.70
III. 3, 2-D both	2.59	21.40	21.48	1.49

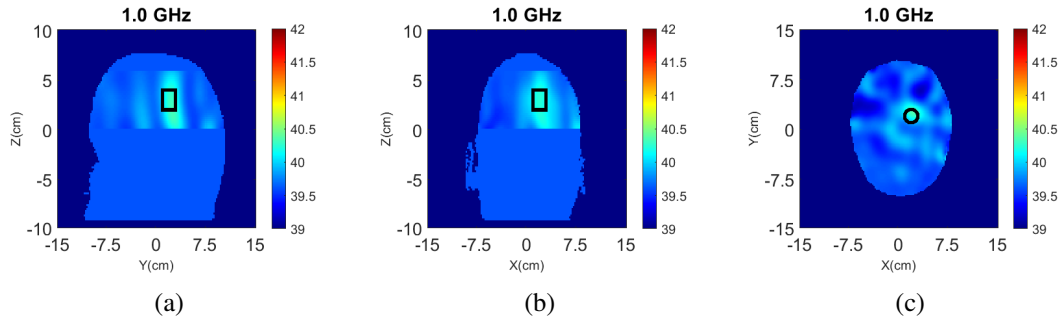


Figure 5.21: 3-D reconstructions of $\Re(\epsilon_r)$ for Case III.2 at 1.0 GHz: (a) y-z slice, (b) x-z slice, and (c) x-y slice, same as Fig.5.17 but with vectorial Green's functions in (3.17).

III.1 to 3, where headbands are with radii $\rho = 135$ and 140 mm, with and without the absorbing layers. As expected, when the interface distance increases, detection accuracy and reconstruction quality improves. Moreover, the absorbing materials improve reconstructions further. Importantly, 3-D imaging outperforms its 2-D counterpart in all these cases.

Table 5.5: Reconstruction errors for experimental case.

Simulation Name	Iteration	RMSE	e_{\max}	RRE
Exp, 3-D	20	9.73	48.87	0.17
Exp, 2-D	20	7.31	36.23	0.73

5.5 Experimental data reconstruction

3-D Reconstructions are also performed with the experimental phantom shown in Fig. 3.5. The true dielectric constant values $\Re(\epsilon_r)$ of the experimental phantoms are presented in Fig. 5.22 with errors shown in Table 5.5. An experiment is conducted with the antenna

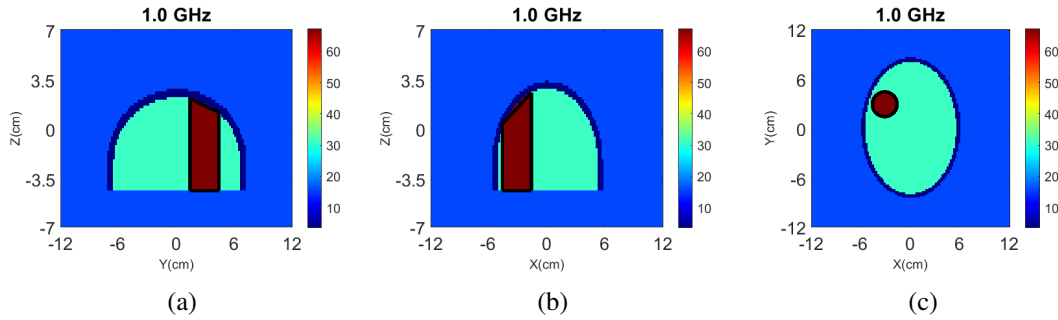


Figure 5.22: Dielectric constant distribution $\Re(\epsilon_r)$ for the validation models. (a) y–z slice, (b) x–z slice, and (c) x–y slice for the experimental phantom.

array surrounding the lower half of the phantom. A cylindrical blood target is inserted with radius $\rho = 15$ mm and permittivity $\epsilon_r \approx 67.3 - 9.3j$ at 1.0 GHz into the phantom, centred at $(-30$ mm, 30 mm) along the horizontal axes. Reconstructions in 3-D and for the 2-D slice defined by the antenna centres are shown in Fig. 5.23, where the Debye parameters of the brain material $\epsilon_\infty = 20$, $\Delta\epsilon = 20$ and $\sigma_s = 0.147$ are used.

The 2-D reconstruction has fewer artefacts than the 3-D image along with the same x-y slice, as it solves an inverse problem with fewer unknowns. The y-z and x-z slices from the 3-D reconstructions show that the bottom part of the cylindrical target is detected more clearly than the upper half, as the eight-antenna ring is placed in the lower half. These

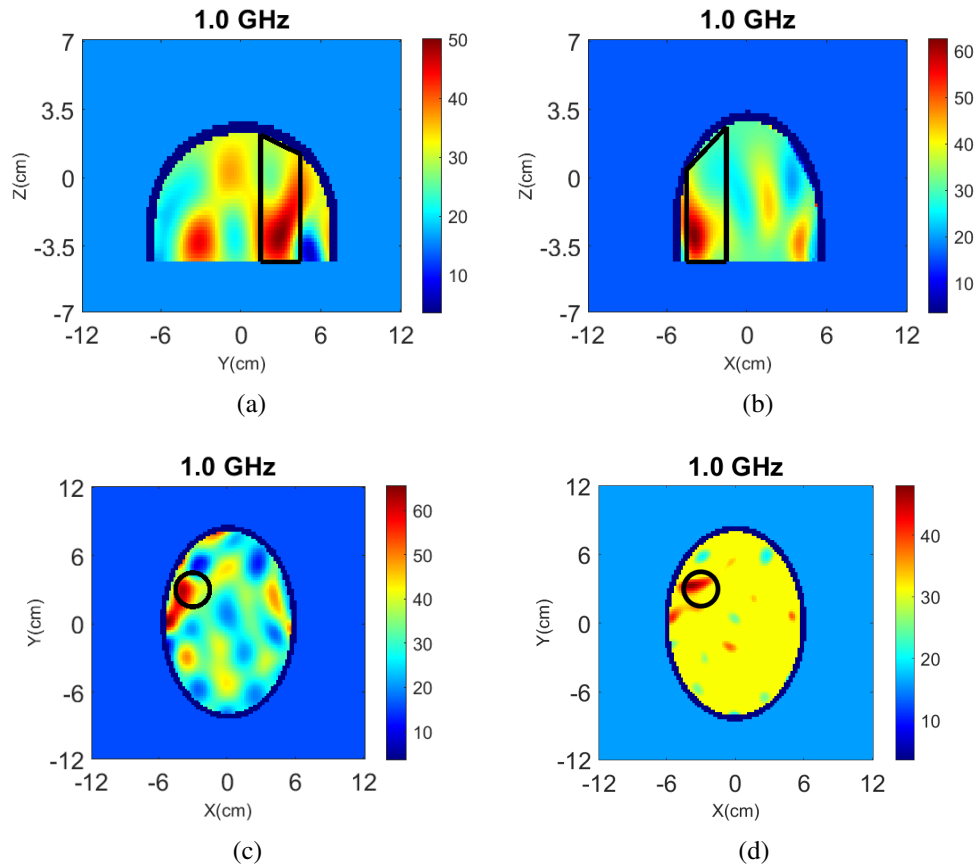


Figure 5.23: Reconstructions of $\Re(\epsilon_r)$ for the experimental data at 1.0 GHz in 3-D: (a) y-z slice, (b) x-z slice, and (c) x-y slice, and in 2-D (d).

images also suggest that reflections from the plastic container have created artefacts in the 3-D reconstruction images. Overall, 2-D and 3-D algorithms have detected the target in the right position, albeit with artefacts that are more pronounced in 3-D for the axial slice.

Reconstructions are performed when the antenna ring is placed at different heights, and the results become worse or even fail to detect the target when the antenna ring is near the upper part of the head phantom due to that the curvature of the surface reflects signals into the air which are not captured by the antenna ring.

5.6 Conclusion

This chapter introduces the 3-D DBIM implementation with an in-house 3-D FDTD forward solver implemented on the GPU, which is equally accurate but runs considerably faster than previous implementations with the commercial software Acceleware. Reconstructions are performed with the Zubal head phantom and an experimental brain phantom, where 2-D and 3-D reconstructions are compared. The results show similar quality for the cases where the data processed by the 2-D imaging algorithm are of sufficient quality. Comparisons of 3-D and 2-D reconstructions for the cases where the target is not centred at the same transverse plane as the antenna ring showcase the advantages of 3-D imaging. Moreover, these cases also demonstrate that terminating the imaging headband with absorbing material can drastically improve the 3-D array's imaging performance.

Chapter 6

Tools to Improve the DBIM Approach

In this chapter, two tools are introduced which can be used to improve the reconstruction results.

The first tool is a signal processing technique that uses time gating to denoise experimental signals. This technique is applied to improve the measured data for the cylindrical target cases. However, it is risky to process the experimental data as MWI algorithms are sensitive to the changes in data. Therefore, it has not been applied to complex cases of head phantoms and will be tested in future work. The second tool uses machine learning (ML) algorithms with the LSM and DBIM to classify the reconstruction results into different classes, which helps to distinguish the target. As a linear method, the LSM is only valid for simple cases where only the target is unknown. Advanced versions of the LSM are required for complicated cases, which will be investigated in future work.

6.1 Time gating for experimental data

Time domain analysis is helpful for evaluating the device-under-test, which provides a more intuitive and direct look at the signal characteristics. In addition, it gives more meaningful information about the system by showing the signal response in time.

For data obtained from experimental systems, *i.e.*, frequency-domain S-parameters from the VNA system, reflections from the connectors, cables and other components of the VNA system affect the signal quality, resulting in noise in the S-parameters. Signal

processing techniques can be employed to denoise the experimental data, such as time gating [155], [156], which could remove reflections and unwanted signals.

Time gating is a useful technique for selectively removing or including responses in the time domain. With time gating, the remaining time-domain responses can be transformed back to the frequency domain with the unwanted responses removed. This could improve the quality of the signal and resemble more the signal if there were no extra reflections. However, in the real world, time gating is not a “brick-wall” function, which could cause ringing in the frequency domain. Therefore, gating is performed solely in the frequency domain with the original response to avoid that.

To process the frequency-domain data by time gating, the data are first converted to the time domain by inverse Fourier transform (IFT). The time-domain impulse response can be gated with a selected gate function, such as the Hamming window [157],

$$w(n) = 0.54 - 0.46\cos(2\pi nN), 0 \leq n \leq N, \quad (6.1)$$

or the Kaiser window [158],

$$w(n) = \frac{I_0\left(\beta\sqrt{1 - \left(\frac{n-N/2}{N/2}\right)^2}\right)}{I_0(\beta)}, \quad 0 \leq n \leq N, \quad (6.2)$$

where β is a selected positive number, I_0 is the zeroth-order modified Bessel function of the first kind with $I_0(x) = \sum_{m=0}^{\infty} \frac{1}{m!\Gamma(m+1)} \left(\frac{x}{2}\right)^{2m}$, and $\Gamma(m) = \int_0^{\infty} e^{-t} t^{m-1} dt$. The point with the peak value is set to be the centre point of the gate function, and a time span covering a selected length is chosen, which builds the gating function in the time domain. This gate width also determines the equivalent frequency gating function. Therefore, the function is converted back to the frequency domain by FT. Finally, the frequency-domain

window function is convolved with the original data to obtain the gated data.

In Fig. 6.1(a) and Fig. 6.1, an example where only the homogeneous background medium is present by using the above time-gating technique to process the S-parameter, where the time span is set to 30 ns. The time-domain data are plotted with the use of a Hamming window function. As shown in Fig. 6.1(a), most of the reflections after the peak value are removed by the window function. For the frequency-domain data, the plotting curve of the gated data is much more stable than the original data, which is smoothed by the window function.

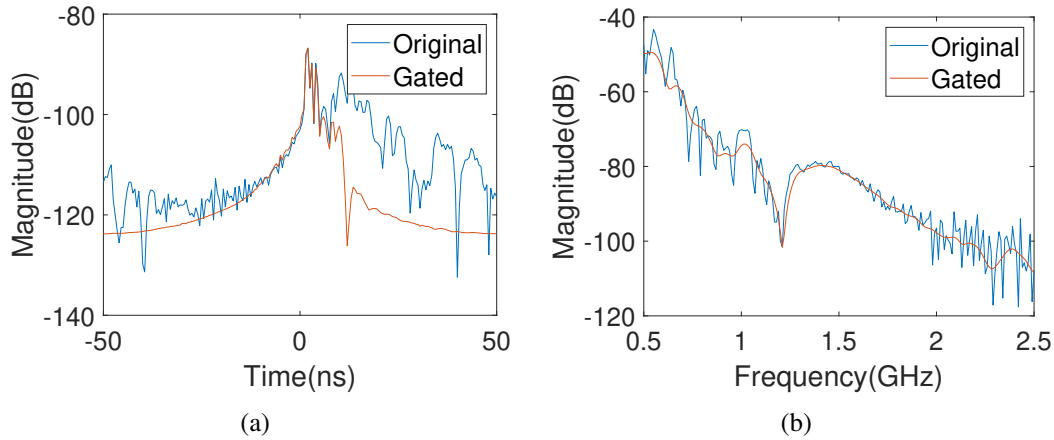


Figure 6.1: Magnitude in dB of the S-parameter in (a) time domain and (b) frequency domain.

Reconstructions are performed with the experimental data of the cylindrical target scenario without and with the time gating techniques. The real part of the permittivity of the reconstruction results is shown in Fig. 6.2 and Fig. 6.3, where the reconstruction domain and the exact target size are marked in a magenta circle and a black circle, respectively. For each one, 20 DBIM iterations are performed, and the same number of iterations inside the inverse solver is used, which is set to be 75. The figures in the first row and the third row are the reconstruction results with original data by FISTA, and the second row and the fourth row are the reconstructions with processed data by FISTA. By

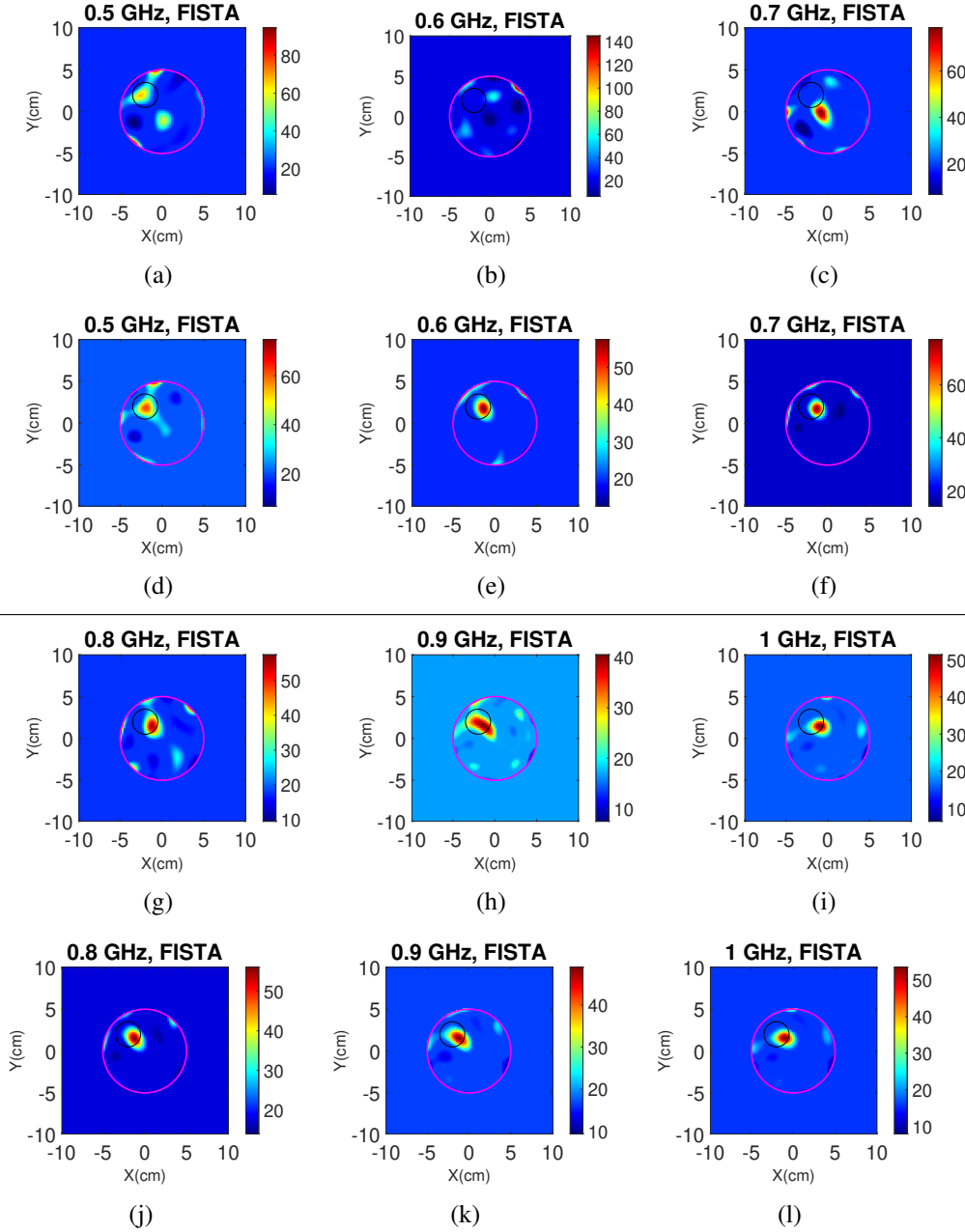


Figure 6.2: Reconstructions of real permittivity of one target by 20 DBIM iterations. First and third rows (a) – (c) and (g) – (i): reconstructed by FISTA with original data. Second and fourth rows (d) – (f) and (j) – (l): reconstructed by FISTA with processed data.

comparison of reconstructions, the results with processed data have been improved significantly, especially at 0.6 GHz and 0.7 GHz, where the targets are not detected with the

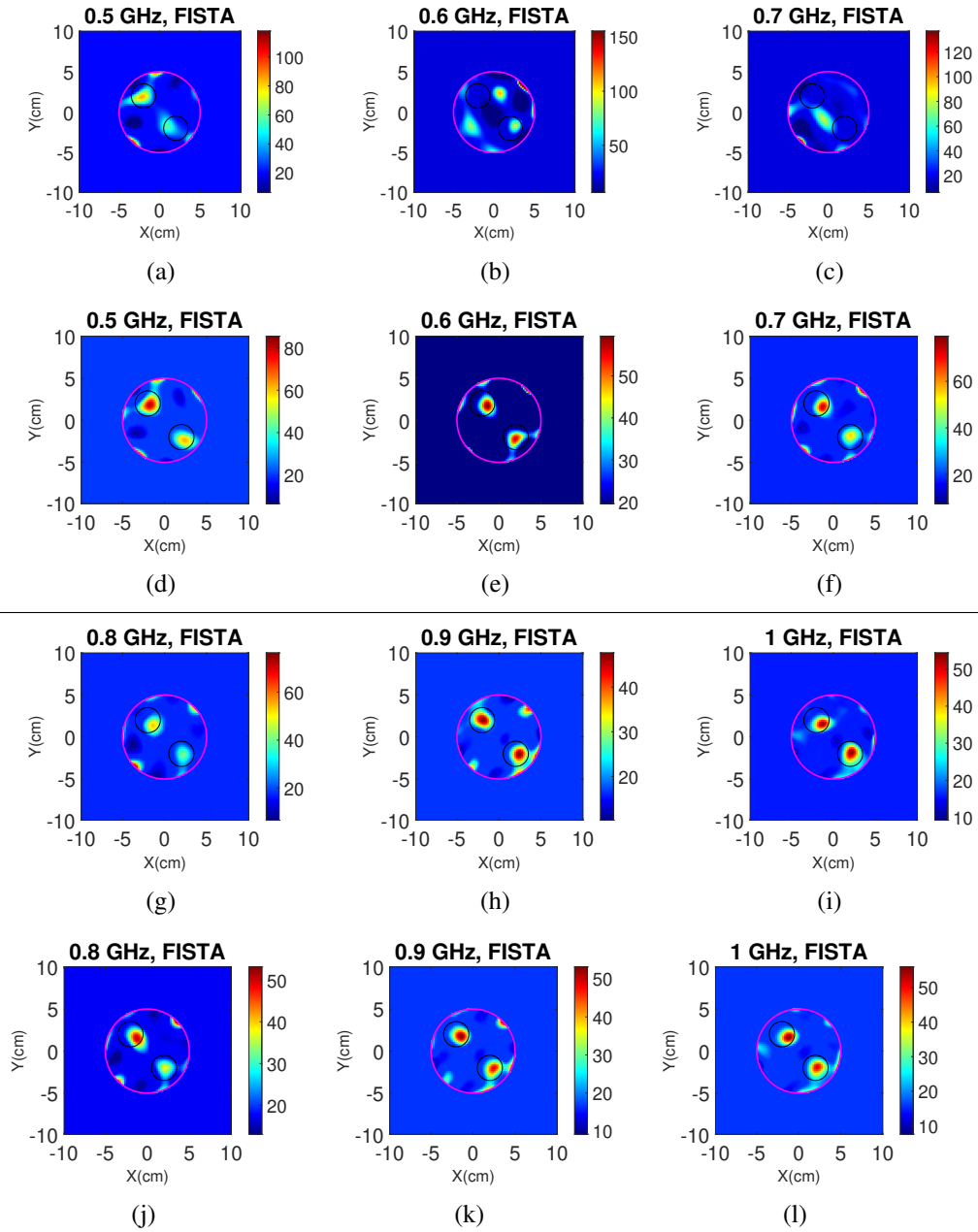


Figure 6.3: Reconstructions of real permittivity of two targets by 20 DBIM iterations. First and third rows (a) – (c) and (g) – (i): reconstructed by FISTA with original data. Second and fourth rows (d) – (f) and (j) – (l): reconstructed by FISTA with processed data.

original data.

With improved measurement data, the reconstructed target can be cross-checked.

However, we should note that the original signal processed by time gating should be suitable enough for reconstruction. If the original signals contain huge noise, time gating is not applicable to recover the signal from none, *e.g.*, in the time domain if there are consecutive peak values.

6.2 Target classification with MWI algorithms

After reconstruction, values can be obtained by quantitative or qualitative imaging methods, helping to better distinguish the target from surrounding materials. For qualitative imaging algorithms, an indicator which estimates the shape of the reconstruction domain is obtained, while for quantitative imaging algorithms, reconstructed values of dielectric properties (or Debye parameters by FDTD) can be obtained. These values can be used as input for clustering, and a binary (or ternary, *etc.*) classification map can be produced.

The most commonly used clustering method is k-means [159] which aims to partition the n observations into $k \leq n$ sets. The object function of k-means is

$$J = \sum_i^k \sum_{\mathbf{x} \in S_i} \|\mathbf{x} - \mu_i\|^2, \quad (6.3)$$

where J is the cost function to be minimised, μ_i is the mean of i -th cluster. The general procedure of k-means is by alternating two steps as follows,

1. Assign each observation \mathbf{x} to the nearest mean with a predefined distance.
2. Recalculate the mean of each cluster.

After several iterations, usually when the mean is fixed (or some other stop criteria), the dataset is classified with k labels, where each of the observations has a label. With k-means after the reconstruction procedure, the obtained values can be clustered.

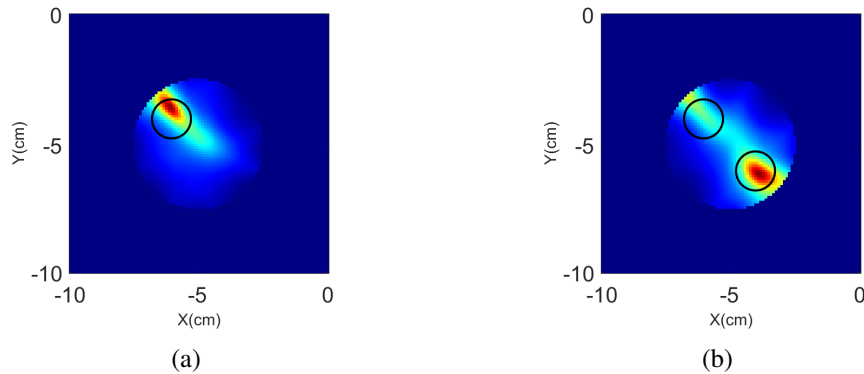


Figure 6.4: LSM results of cylindrical target cases. (a) Single target. (b) Two targets.

Taking into account the experimental cylindrical cases, the reconstruction map that indicates the dielectric distribution by LSM of the one and two target cases is shown in Fig. 6.4. Defining the values of the reconstructed region as a set S and each point as $S(i)$ and assuming there are two groups to be classified (the area outside the reconstruction region is set to 0), the classification image is illustrated by k-means as Fig. 6.5. The yellow, green, and blue colours mean the classification as target $S(i) = 2$, background $S(i) = 1$, and outside region $S(i) = 0$, respectively. The classification covers the area that includes the target, which helps to better locate the target position. It can only provide a rough estimate of the reconstruction. However, this classification result can be used with other results or imaging techniques as a priori information.

Based on the results obtained by DBIM, clustering can also be performed by k-means, and the obtained classification is shown in Fig. 6.6. Some noise in the reconstruction image is classified as targets. The classification is already apparent, as it is a simple cylindrical target case, and can be slightly improved by combining the LSM results. We

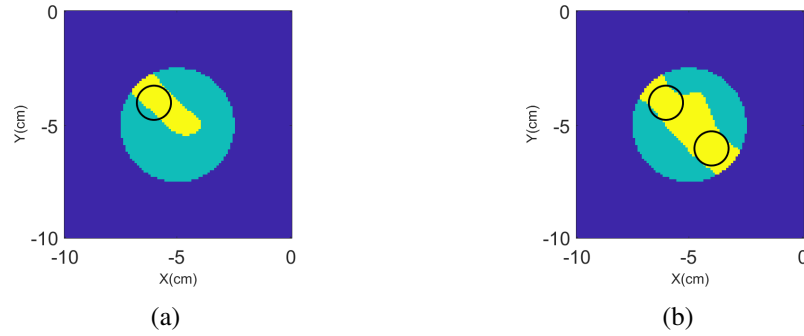


Figure 6.5: Classification of cylindrical target cases by LSM, (a) single target, and (b) two targets.

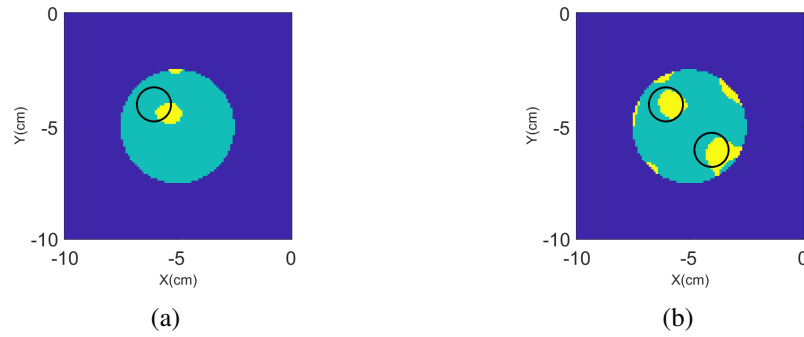


Figure 6.6: Classification of cylindrical target cases by DBIM, (a) single target, and (b) two targets.

can define an intersection of the classification results of LSM and DBIM as,

$$S(i) = \begin{cases} 2 & \text{if } S(i) = 2 \text{ for both LSM and DBIM} \\ 1 & \text{if } S(i) = 1 \text{ for LSM or DBIM} \\ 0 & \text{otherwise} \end{cases} . \quad (6.4)$$

The new classification is shown in Fig. 6.7, which is close to the truth.

Taking into account a more complex case where the Zubal phantom in Fig. 4.20 is used with the data obtained from CST, the classification results by LSM and DBIM are shown in Fig. 6.8. As a linear method, the LSM is hard to obtain the exact target position for this

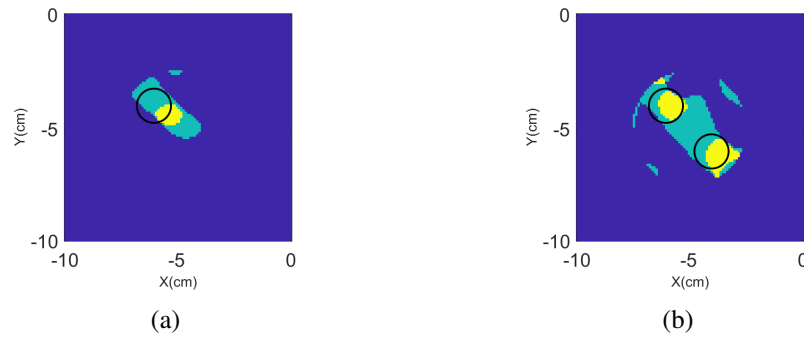


Figure 6.7: Classification of cylindrical target cases after intersection, (a) single target, and (b) two targets.

case with a strong scatterer. The DBIM reconstructs the target, though the classification wrongly classifies the noise as targets. After the intersection, the classification area is nearly the actual position of the target.

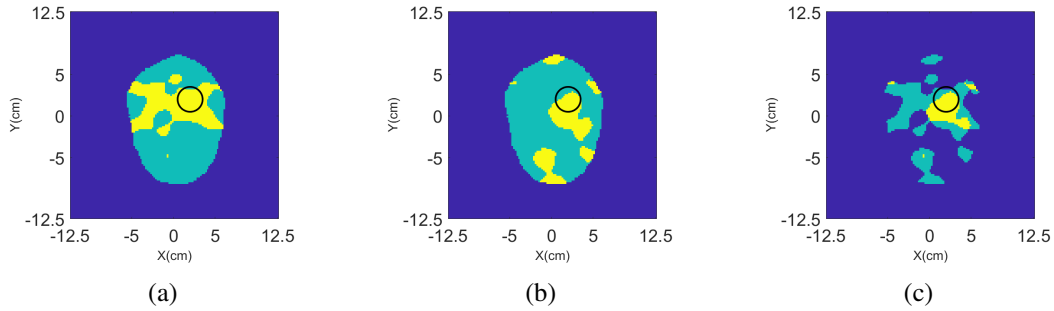


Figure 6.8: Classification of the CST Zubal phantom case. (a) LSM. (b) DBIM. (c) After intersection.

The possible application of this result can be used to distinguish the target area or can be used as an initial step for DBIM reconstruction, which first uses the intersection classification result of LSM and DBIM to reduce the reconstruction domain and then perform another DBIM reconstruction.

6.3 Conclusion

In this chapter, we present two efficient tools for MWI algorithms, where the first can help improve reconstruction performance by denoising the signal, and the second can be used as a postprocessing tool to help distinguish the target.

Chapter 7

Conclusions and Future Work

7.1 Conclusions

This thesis aims to develop novel MWI algorithms for medical applications, tested mainly for head imaging scenarios. The conclusions of the research work and the list of contributions are listed as the following two parts.

A. Conclusions of the research work

- An efficient FEM-based DBIM approach, which uses the basis functions of FEM to build the inverse matrix of DBIM, is proposed and validated with numerical and experimental data. It is also compared with the 2-D FDTD-based DBIM approach, which shows good agreement for the forward simulation results as well as the reconstruction results.
- An in-house 3-D FDTD is implemented on the GPU hardware with the help of CUDA toolkit, and it is used as the forward solver for the 3-D DBIM approach, which is validated with different data including CST simulated data and experimental data.
- A robust and efficient inverse solver called FISTA is first used in MWT and shows good capacity for solving the ill-posed linear system, which is incorporated with the DBIM approach in the 2-D and 3-D implementations.
- A simplified 3-D inverse algorithm that considers a scalar Green's function for lin-

early polarised antennas such as the printed monopoles used in the experimental system is proposed and compared with the scalar Green's function in head imaging scenarios.

- Numerical and experimental models are used to evaluate the performance of the proposed 2-D and 3-D DBIM approaches, including basic models such as cylindrical models, and complicated head phantoms. An anatomically complex head phantom called the Zubal head phantom is used to investigate the reconstruction possibility with limited information and when targets are placed off-centre.
- The 3-D implementation is compared with the 2-D implementation in head imaging scenarios, which shows that the 2-D algorithm can obtain similar results when the data are of sufficient quality for 2-D problems. However, the 3-D algorithm shows advantages for the cases where the target is not centred at the same transverse plane as the antenna ring and reflections from the interface of a headband with air are significant.
- Two processing tools are proposed and used for MWI problems, including the time gating technique and the clustering technique by k-means. The time gating is applied to experimental cases, and the k-means algorithm is used to help partition the reconstruction results into different classes.

B. List of contributions

- Unlike the traditional FEM-based DBIM approach that builds the inverse matrix by calculating the electric field using the interpolation procedure, the proposed FEM-based DBIM approach utilises the entries of the inverse matrix readily calculated from already pre-computed matrices in the FEM procedure, which provides excel-

lent efficiency and allows a straightforward and accurate computation of the integrals in DBIM.

- The inverse solver FISTA uses a shrinkage operator to reduce the noise of the solution and an accelerated momentum to increase the convergence rate, which is more robust and faster than the commonly used GD-type inverse solvers and requires fewer parameters than the TwIST algorithm. FISTA shows much better performance than CGLS and slightly lower relative errors than the TwIST algorithm.
- The GPU-accelerated FDTD implementation reduces time cost and significantly improves efficiency compared to traditional CPU implementation. This implementation is also equally accurate but runs considerably faster than the previous used commercial software Acceleware.
- Reconstructions using the scalar Green's function and vectorial Green's function are compared for the first time. Results show that this scalar approximation does not lead to worse performance than a vectorial Green's function implementation for the considered head imaging scenarios.
- Reconstructions of the realistic Zubal head phantom in different scenarios with data obtained from full-wave CST simulations are investigated for the first time, which can help to provide a better understanding of the challenges and performance in real head imaging scenarios, especially for 3-D imaging problems.
- The time gating can denoise the signals obtained from the experimental system by the gating functions, which achieves smooth frequency domain S-parameters and improves reconstruction results. The classification technique can be used as an additional tool to distinguish the target after reconstruction and has the potential to be used to provide initial information before reconstruction.

7.2 Future work

A. Realistic modelling and calculation

The antenna is modelled as a point source for the proposed 2-D and 3-D algorithms in this thesis. The antenna used in the experimental system is a monopole patch antenna, and the produced wave has a different form from the wave produced by the point source. The newly designed antenna uses meta-materials with a substrate to enhance performance, which should also be taken into account. Besides, coupling between antennas also exists and influences the received signal. Modelling the complex structure of the antenna in the simulation lattice can make the simulation more realistic and reduce the discrepancy between simulation and experiment. The format of the data obtained from the experiment and CST is S-parameter. However, the data from FDTD simulations are the electric field and should be converted to S-parameters using voltage computation. Modelling the antenna structure and transforming the FDTD electric field to S-parameters can also help reduce the discrepancy between simulation and measurement.

The single-pole Debye model is used to model frequency-dependent materials by curve fitting, resulting in an accuracy loss of the permittivity values due to the nonlinearity of the material properties. Multi-pole Debye model can be applied to enhance the performance of curve fitting and reduce the modelling error. Besides, the relaxation time of the Debye model is fixed in this thesis, which can be set to different values for different materials.

B. Algorithm acceleration and optimisation

The 3-D FDTD algorithm with CPML as ABCs is implemented on GPU as described in Chapter 5 to simulate EM wave propagation. The electric field and magnetic field are updated on the basis of the GPU 2-D block with a *for* loop. This implementation can be

further optimised to fully utilise the concurrency of the algorithm. The *for* loop for the third dimension of the FDTD lattice in the GPU kernel can be eliminated by mapping the 3-D indices to 2-D indices as all calculations of each point are independent.

This implementation is on a single GPU, and only one simulation of each transmitter antenna is run simultaneously. The maximum number of threads on a single GPU may not satisfy the number of grid points of the simulation, and the simulation of each transmitter antenna is also independent. Thus, the implementation can be extended to multiple GPUs to achieve full parallelisation. With multiple GPUs, increased cores can better satisfy the number of required threads, and multiple simulations of transmitter antennas can be performed simultaneously. In this thesis, the observation data are required to be extracted from the GPU and stored in the CPU due to the large memory requirement of matrix size. Moreover, the matrix computation of the DBIM algorithm is also performed on the CPU. This inverse part can be implemented fully on the GPU with increased memory provided by multiple GPUs, which can significantly reduce the interaction time between devices.

The selection of parameters is an important and challenging task, including FISTA parameters. Instead of fixed values, an adaptive method can be developed to set the parameters based on the solution to provide more flexibility and optimise the FISTA performance.

The two techniques described in Chapter 6 can be used to enhance the reconstruction performance and have been applied to simple cases where only the targets are unknown. Future work can focus on more challenging cases, such as the head model scenarios. Target classification using more advanced algorithms using neural networks can also be applied to MWI scenarios in the future.

C. Prior knowledge

In this thesis, a preliminary study of reconstructions of head phantoms with limited prior

information is presented. In addition to the experimental case presented in this thesis, further research can be performed on more realistic experimental models based on the simulation results. Although reconstructions are investigated when limited information is given, acquiring prior information of the investigated human tissues, even a coarse estimate, is still arduous in real scenarios. For example, the head is extremely complicated with dozens of tissues, of which the dielectric properties are not possible to obtain. Investigations should be performed for experimental phantoms with more complicated structures and less prior information.

D. Towards clinical applications

This thesis has studied the proposed method for numerical and experimental models with an initial experimental system. However, scenarios can be more complicated in clinical applications and the requirement for the MWI device is strict. The experimental system used in this work has a VNA system connected to a computer. However, the MWI device should be designed as a portable device. Though it is possible to realise a device with portability with modern MWI hardware techniques, the processing algorithm is impossible to be embedded in the device as it requires considerable computational power. An alternative approach is sending the signals collected by the device to a server that processes the data remotely.

Experimental reconstructions are planned to be performed with a helmet/headband that can be used to cover the human head. In clinical application, this helmet/headband should be suitably designed with flexibility due to the varying head shapes of different patients. Furthermore, the issue of patient movement should also be investigated, as head position may differ in different sets of measurements. Thus, a robust MWI algorithm should be developed that takes into account these issues.

Bibliography

- [1] D. P. Frush, “Review of radiation issues for computed tomography,” *Seminars in Ultrasound, CT and MRI*, vol. 25, no. 1, pp. 17–24, 2004.
- [2] S. P. Power, F. Moloney, M. Twomey, K. James, O. J. O’Connor, and M. M. Maher, “Computed tomography and patient risk: Facts, perceptions and uncertainties,” *World Journal of Radiology*, vol. 8, no. 12, p. 902, 2016.
- [3] T. R. DeGrado, T. G. Turkington, J. J. Williams, C. W. Stearns, J. M. Hoffman, and R. E. Coleman, “Performance characteristics of a whole-body PET scanner,” *Journal of Nuclear Medicine*, vol. 35, no. 8, pp. 1398–1406, 1994.
- [4] P. Lind, I. Igerc, T. Beyer, P. Reinprecht, and K. Hausegger, “Advantages and limitations of FDG PET in the follow-up of breast cancer,” *European Journal of Nuclear Medicine and Molecular Imaging*, vol. 31, no. 1, S125–S134, 2004.
- [5] G. Katti, S. A. Ara, and A. Shireen, “Magnetic resonance imaging (MRI)—a review,” *International Journal of Dental Clinics*, vol. 3, no. 1, pp. 65–70, 2011.
- [6] M. Sarracanie, C. D. LaPierre, N. Salameh, D. E. Waddington, T. Witzel, and M. S. Rosen, “Low-cost high-performance MRI,” *Scientific Reports*, vol. 5, no. 1, pp. 1–9, 2015.
- [7] P. Kosmas and L. Crocco., “Introduction to special issue on “Electromagnetic technologies for medical diagnostics: Fundamental issues, clinical applications and perspectives,” *Diagnostics*, vol. 9, no. 1, p. 19, 2019.

- [8] S. Semenov, “Microwave tomography: Review of the progress towards clinical applications,” *Philosophical Transactions. Series A, Mathematical, Physical, and Engineering Sciences*, vol. 367, pp. 3021–42, Sep. 2009.
- [9] M. A. Aldhaeabi, K. Alzoubi, T. S. Almoneef, S. M. Bamatraf, H. Attia, and O. M. Ramahi, “Review of microwaves techniques for breast cancer detection,” *Sensors*, vol. 20, no. 8, p. 2390, 2020.
- [10] S. Hosseinzadegan, A. Fhager, M. Persson, and P. Meaney, “A discrete dipole approximation solver based on the COCG-FFT algorithm and its application to microwave breast imaging,” *International Journal of Antennas and Propagation*, vol. 2019, 2019.
- [11] J. M. Felicio, J. M. Bioucas-Dias, J. R. Costa, and C. A. Fernandes, “Microwave breast imaging using a dry setup,” *IEEE Transactions on Computational Imaging*, vol. 6, pp. 167–180, 2019.
- [12] D. O’Loughlin, M. O’Halloran, B. M. Moloney, M. Glavin, E. Jones, and M. A. Elahi, “Microwave breast imaging: Clinical advances and remaining challenges,” *IEEE Transactions on Biomedical Engineering*, vol. 65, no. 11, pp. 2580–2590, 2018.
- [13] B. Sohani, B. Khalesi, N. Ghavami, *et al.*, “Detection of haemorrhagic stroke in simulation and realistic 3-D human head phantom using microwave imaging,” *Biomedical Signal Processing and Control*, vol. 61, p. 102 001, 2020.
- [14] P. Lu and P. Kosmas, “Three-dimensional microwave head imaging with GPU-based FDTD and the DBIM method,” *Sensors*, vol. 22, no. 7, p. 2691, 2022.
- [15] S. Hosseinzadegan, A. Fhager, M. Persson, S. D. Geimer, and P. M. Meaney, “Discrete dipole approximation-based microwave tomography for fast breast can-

- cer imaging,” *IEEE Transactions on Microwave Theory and Techniques*, vol. 69, no. 5, pp. 2741–2752, 2021.
- [16] M. Tivnan, C. Rappaport, J. A. Martinez-Lorenzo, and A. Morgenthaler, “FDFD microwave modeling of realistic, inhomogeneous breast tissue based on digital breast tomosynthesis priors for cancer detection,” in *2014 40th Annual Northeast Bioengineering Conference (NEBEC)*, Apr. 2014, pp. 1–2.
- [17] A. Modiri, S. Goudreau, A. Rahimi, and K. Kiasaleh, “Review of breast screening: Toward clinical realization of microwave imaging,” *Medical Physics*, vol. 44, no. 12, e446–e458, 2017.
- [18] M. Adachi, T. Nakagawa, T. Fujioka, *et al.*, “Feasibility of portable microwave imaging device for breast cancer detection,” *Diagnostics*, vol. 12, no. 1, p. 27, 2021.
- [19] M. Islam, M. Mahmud, M. T. Islam, S. Kibria, and M. Samsuzzaman, “A low cost and portable microwave imaging system for breast tumor detection using UWB directional antenna array,” *Scientific Reports*, vol. 9, no. 1, pp. 1–13, 2019.
- [20] A. T. Mobashsher, A. Mahmoud, and A. Abbosh, “Portable wideband microwave imaging system for intracranial hemorrhage detection using improved back-projection algorithm with model of effective head permittivity,” *Scientific Reports*, vol. 6, no. 1, pp. 1–16, 2016.
- [21] S. Y. Semenov and D. R. Corfield, “Microwave tomography for brain imaging: Feasibility assessment for stroke detection,” *International Journal of Antennas and Propagation*, vol. 2008, 2008.

- [22] R. Chandra, H. Zhou, I. Balasingham, and R. M. Narayanan, “On the opportunities and challenges in microwave medical sensing and imaging,” *IEEE Transactions on Biomedical Engineering*, vol. 62, no. 7, pp. 1667–1682, 2015.
- [23] S. Kumar and S. Shukla, *Concepts and applications of microwave engineering*. PHI Learning, 2014.
- [24] M. Pastorino and A. Randazzo, *Microwave imaging methods and applications*. Artech House, 2018.
- [25] J. L. Schepps and K. R. Foster, “The UHF and microwave dielectric properties of normal and tumour tissues: Variation in dielectric properties with tissue water content,” *Physics in Medicine & Biology*, vol. 25, no. 6, p. 1149, 1980.
- [26] K. R. Foster, H. P. Schwan, *et al.*, “Dielectric properties of tissues,” *CRC Handbook of Biological Effects of Electromagnetic Fields*, pp. 27–96, 1986.
- [27] C. Gabriel, S. Gabriel, and Y. E. Corthout, “The dielectric properties of biological tissues: I. Literature survey,” *Physics in Medicine & Biology*, vol. 41, no. 11, p. 2231, 1996.
- [28] S. Gabriel, R. Lau, and C. Gabriel, “The dielectric properties of biological tissues: II. Measurements in the frequency range 10 Hz to 20 GHz,” *Physics in Medicine & Biology*, vol. 41, no. 11, p. 2251, 1996.
- [29] ———, “The dielectric properties of biological tissues: III. Parametric models for the dielectric spectrum of tissues,” *Physics in Medicine & Biology*, vol. 41, no. 11, p. 2271, 1996.
- [30] M. Lazebnik, L. McCartney, D. Popovic, *et al.*, “A large-scale study of the ultra-wideband microwave dielectric properties of normal breast tissue obtained from

- reduction surgeries,” *Physics in Medicine & Biology*, vol. 52, no. 10, p. 2637, 2007.
- [31] A. J. Surowiec, S. S. Stuchly, J. R. Barr, and A. Swarup, “Dielectric properties of breast carcinoma and the surrounding tissues,” *IEEE Transactions on Biomedical Engineering*, vol. 35, no. 4, pp. 257–263, 1988.
- [32] Y. Cheng and M. Fu, “Dielectric properties for non-invasive detection of normal, benign, and malignant breast tissues using microwave theories,” *Thoracic Cancer*, vol. 9, no. 4, pp. 459–465, 2018.
- [33] A. Peyman, S. Holden, S. Watts, R. Perrott, and C. Gabriel, “Dielectric properties of porcine cerebrospinal tissues at microwave frequencies: In vivo, in vitro and systematic variation with age,” *Physics in Medicine & Biology*, vol. 52, no. 8, p. 2229, 2007.
- [34] G. Schmid, G. Neubauer, and P. R. Mazal, “Dielectric properties of human brain tissue measured less than 10 h postmortem at frequencies from 800 to 2450 MHz,” *Bioelectromagnetics*, vol. 24, no. 6, pp. 423–430, 2003.
- [35] S. Semenov, T. Huynh, T. Williams, B. Nicholson, and A. Vasilenko, “Dielectric properties of brain tissue at 1 GHz in acute ischemic stroke: Experimental study on swine,” *Bioelectromagnetics*, vol. 38, no. 2, pp. 158–163, 2016.
- [36] D. Andreuccetti. “An internet resource for the calculation of the dielectric properties of body tissues in the frequency range 10 Hz-100 GHz.” (2012), [Online]. Available: <http://niremf.ifac.cnr.it/tissprop/>.
- [37] P. Hasgall, F. Di Gennaro, C. Baumgartner, *et al.* “IT’IS database for thermal and electromagnetic parameters of biological tissues.” (May 2018), [Online]. Avail-

- able: <https://itis.swiss/virtual-population/tissue-properties/database/dielectric-properties/>.
- [38] M. Mahmud, M. T. Islam, N. Misran, A. F. Almutairi, M. Cho, *et al.*, “Ultra-wideband (UWB) antenna sensor based microwave breast imaging: A review,” *Sensors*, vol. 18, no. 9, p. 2951, 2018.
 - [39] N. Alam, A. Ahmed, M. A. I. Oni, T. A. Meem, and M. A. Rahman, “UWB microwave imaging for non-invasive anomaly detection in human lung and possible application in COVID-19 diagnosis: A review,” in *2021 2nd International Conference on Robotics, Electrical and Signal Processing Techniques (ICREST)*, 2021, pp. 772–776.
 - [40] R. K. Amineh, M. Ravan, A. Trehan, and N. K. Nikolova, “Near-field microwave imaging based on aperture raster scanning with TEM horn antennas,” *IEEE Transactions on Antennas and Propagation*, vol. 59, no. 3, pp. 928–940, 2010.
 - [41] S. C. Hagness, E. C. Fear, and A. Massa, “Guest editorial: Special cluster on microwave medical imaging,” *IEEE Antennas and Wireless Propagation Letters*, vol. 11, pp. 1592–1597, 2012.
 - [42] W. Shao and T. McCollough, “Advances in microwave near-field imaging: Prototypes, systems, and applications,” *IEEE Microwave Magazine*, vol. 21, no. 5, pp. 94–119, 2020.
 - [43] P. M. Meaney, F. Shubitidze, M. W. Fanning, M. Kmiec, N. R. Epstein, and K. D. Paulsen, “Surface wave multipath signals in near-field microwave imaging,” *International Journal of Biomedical Imaging*, vol. 2012, 2012.

- [44] A. Schiessl, A. Genghammer, S. S. Ahmed, and L.-P. Schmidt, "Phase error sensitivity in multistatic microwave imaging systems," in *2013 European Microwave Conference*, 2013, pp. 1631–1634.
- [45] P. Meaney, K. Paulsen, and J. Chang, "Near-field microwave imaging of biologically-based materials using a monopole transceiver system," *IEEE Transactions on Microwave Theory and Techniques*, vol. 46, no. 1, pp. 31–45, 1998.
- [46] X. Li and S. Hagness, "A confocal microwave imaging algorithm for breast cancer detection," *IEEE Microwave and Wireless Components Letters*, vol. 11, no. 3, pp. 130–132, 2001.
- [47] L. Guo and A. M. Abbosh, "Optimization-based confocal microwave imaging in medical applications," *IEEE Transactions on Antennas and Propagation*, vol. 63, no. 8, pp. 3531–3539, 2015.
- [48] E. J. Bond, X. Li, S. C. Hagness, and B. D. Van Veen, "Microwave imaging via space-time beamforming for early detection of breast cancer," *IEEE Transactions on Antennas and Propagation*, vol. 51, no. 8, pp. 1690–1705, 2003.
- [49] X. Li, E. J. Bond, B. D. Van Veen, and S. C. Hagness, "An overview of ultra-wideband microwave imaging via space-time beamforming for early-stage breast-cancer detection," *IEEE Antennas and Propagation Magazine*, vol. 47, no. 1, pp. 19–34, 2005.
- [50] P. Kosmas and C. M. Rappaport, "Time reversal with the FDTD method for microwave breast cancer detection," *IEEE Transactions on Microwave Theory and Techniques*, vol. 53, no. 7, pp. 2317–2323, 2005.

- [51] J. M. Sill and E. C. Fear, "Tissue sensing adaptive radar for breast cancer detection—Experimental investigation of simple tumor models," *IEEE Transactions on Microwave theory and Techniques*, vol. 53, no. 11, pp. 3312–3319, 2005.
- [52] N. Ghavami, G. Tiberi, D. J. Edwards, and A. Monorchio, "UWB microwave imaging of objects with canonical shape," *IEEE Transactions on Antennas and Propagation*, vol. 60, no. 1, pp. 231–239, 2011.
- [53] D. W. Winters, J. D. Shea, P. Kosmas, B. D. Van Veen, and S. C. Hagness, "Three-dimensional microwave breast imaging: Dispersive dielectric properties estimation using patient-specific basis functions," *IEEE Transactions on Medical Imaging*, vol. 28, no. 7, pp. 969–981, Jul. 2009.
- [54] M. Slaney, A. Kak, and L. Larsen, "Limitations of imaging with first-order diffraction tomography," *IEEE Transactions on Microwave Theory and Techniques*, vol. 32, no. 8, pp. 860–874, 1984.
- [55] Y. Wang and W. C. Chew, "An iterative solution of the two-dimensional electromagnetic inverse scattering problem," *International Journal of Imaging Systems and Technology*, vol. 1, no. 1, pp. 100–108, 1989.
- [56] W. C. Chew and Y. M. Wang, "Reconstruction of two-dimensional permittivity distribution using the distorted Born iterative method," *IEEE Transactions on Medical Imaging*, vol. 9, no. 2, pp. 218–225, Jun. 1990.
- [57] T. M. Habashy, M. L. Oristaglio, and A. T. de Hoop, "Simultaneous nonlinear reconstruction of two-dimensional permittivity and conductivity," *Radio Science*, vol. 29, no. 4, pp. 1101–1118, 1994.
- [58] P. M. Van Den Berg and R. E. Kleinman, "A contrast source inversion method," *Inverse Problems*, vol. 13, no. 6, p. 1607, 1997.

- [59] P. M. Meaney, M. W. Fanning, D. Li, S. P. Poplack, and K. D. Paulsen, “A clinical prototype for active microwave imaging of the breast,” *IEEE Transactions on Microwave Theory and Techniques*, vol. 48, no. 11, pp. 1841–1853, 2000.
- [60] P. Meaney, A. Hartov, T. Raynolds, *et al.*, “Low cost, high performance, 16-channel microwave measurement system for tomographic applications,” *Sensors*, vol. 20, no. 18, 2020.
- [61] M. Asefi, A. Baran, and J. LoVetri, “An experimental phantom study for air-based quasi-resonant microwave breast imaging,” *IEEE Transactions on Microwave Theory and Techniques*, vol. 67, no. 9, pp. 3946–3954, 2019.
- [62] D. Kurrant, M. Omer, N. Abdollahi, P. Mojabi, E. Fear, and J. LoVetri, “Evaluating performance of microwave image reconstruction algorithms: Extracting tissue types with segmentation using machine learning,” *Journal of Imaging*, vol. 7, no. 1, p. 5, 2021.
- [63] O. Karadima, M. Rahman, I. Sotiriou, *et al.*, “Experimental validation of microwave tomography with the DBIM-TwIST algorithm for brain stroke detection and classification,” *Sensors*, vol. 20, no. 3, p. 840, 2020.
- [64] N. Ghavami, E. Razzicchia, O. Karadima, *et al.*, “The use of metasurfaces to enhance microwave imaging: Experimental validation for tomographic and radar-based algorithms,” English, *IEEE Open Journal of Antennas and Propagation*, vol. 3, pp. 89–100, 2022.
- [65] E. Razzicchia, N. Ghavami, D. O. Rodriguez-Duarte, J. A. Tobon Vasquez, F. Vipiana, and P. Kosmas, “Benefits of employing metasurfaces on the design of a microwave brain imaging scanner,” in *2021 International Conference on Electromagnetics in Advanced Applications (ICEAA)*, 2021, pp. 141–141.

- [66] E. Razzicchia, P. Lu, W. Guo, *et al.*, “Metasurface-enhanced antennas for microwave brain imaging,” *Diagnostics*, vol. 11, no. 3, p. 424, 2021.
- [67] R. Palmeri, M. T. Bevacqua, L. Crocco, T. Isernia, and L. Di Donato, “Microwave imaging via distorted iterated virtual experiments,” *IEEE Transactions on Antennas and Propagation*, vol. 65, no. 2, pp. 829–838, 2016.
- [68] J. A. Tobon Vasquez, R. Scapaticci, G. Turvani, *et al.*, “A prototype microwave system for 3D brain stroke imaging,” *Sensors*, vol. 20, no. 9, p. 2607, 2020.
- [69] Z. Wei and X. Chen, “Deep-learning schemes for full-wave nonlinear inverse scattering problems,” *IEEE Transactions on Geoscience and Remote Sensing*, vol. 57, no. 4, pp. 1849–1860, 2019.
- [70] Y. Zhou, Y. Zhong, Z. Wei, T. Yin, and X. Chen, “An improved deep learning scheme for solving 2-D and 3-D inverse scattering problems,” *IEEE Transactions on Antennas and Propagation*, vol. 69, no. 5, pp. 2853–2863, 2020.
- [71] L. Zhang, K. Xu, R. Song, X. Ye, G. Wang, and X. Chen, “Learning-based quantitative microwave imaging with a hybrid input scheme,” *IEEE Sensors Journal*, vol. 20, no. 24, pp. 15 007–15 013, 2020.
- [72] K. Xu, L. Wu, X. Ye, and X. Chen, “Deep learning-based inversion methods for solving inverse scattering problems with phaseless data,” *IEEE Transactions on Antennas and Propagation*, vol. 68, no. 11, pp. 7457–7470, 2020.
- [73] M. A. Yurkin and A. G. Hoekstra, “The discrete dipole approximation: An overview and recent developments,” *Journal of Quantitative Spectroscopy and Radiative Transfer*, vol. 106, no. 1-3, pp. 558–589, 2007.

- [74] T. M. Grzegorzczak, P. M. Meaney, P. A. Kaufman, K. D. Paulsen, *et al.*, “Fast 3-D tomographic microwave imaging for breast cancer detection,” *IEEE Transactions on Medical Imaging*, vol. 31, no. 8, pp. 1584–1592, 2012.
- [75] R. F. Harrington, *Field computation by moment methods*. Wiley-IEEE Press, 1993.
- [76] R. Lavarello and M. Oelze, “A study on the reconstruction of moderate contrast targets using the distorted born iterative method,” *IEEE Transactions on Ultrasonics, Ferroelectrics, and Frequency Control*, vol. 55, no. 1, pp. 112–124, 2008.
- [77] T. Weiland, “A discretization method for the solution of Maxwell’s equations for six component fields,” *Electronics and Communications AEÜ*, 1977.
- [78] K. Yee, “Numerical solution of initial boundary value problems involving Maxwell’s equations in isotropic media,” *IEEE Transactions on Antennas and Propagation*, vol. 14, no. 3, pp. 302–307, 1966.
- [79] J.-M. Jin, *The finite element method in electromagnetics*. John Wiley & Sons, 2015.
- [80] C. Estatico, A. Fedeli, M. Pastorino, and A. Randazzo, “Microwave imaging by means of lebesgue-space inversion: An overview,” *Electronics*, vol. 8, no. 9, p. 945, 2019.
- [81] A. H. Golnabi, P. M. Meaney, S. D. Geimer, and K. D. Paulsen, “3-D microwave tomography using the soft prior regularization technique: Evaluation in anatomically realistic mri-derived numerical breast phantoms,” *IEEE Transactions on Biomedical Engineering*, vol. 66, no. 9, pp. 2566–2575, 2019.
- [82] I. Bisio, C. Estatico, A. Fedeli, *et al.*, “Variable-exponent Lebesgue-space inversion for brain stroke microwave imaging,” *IEEE Transactions on Microwave Theory and Techniques*, vol. 68, no. 5, pp. 1882–1895, 2020.

- [83] ———, “Brain stroke microwave imaging by means of a Newton-conjugate-gradient method in L^p Banach spaces,” *IEEE Transactions on Microwave Theory and Techniques*, vol. 66, no. 8, pp. 3668–3682, 2018.
- [84] M. Slaney, A. Kak, and L. Larsen, “Limitations of imaging with first-order diffraction tomography,” *IEEE Transactions on Microwave Theory and Techniques*, vol. 32, no. 8, pp. 860–874, 1984.
- [85] A. Roger, “Newton-Kantorovitch algorithm applied to an electromagnetic inverse problem,” *IEEE Transactions on Antennas and Propagation*, vol. 29, no. 2, pp. 232–238, 1981.
- [86] R. F. Remis and P. M. van den Berg, “On the equivalence of the Newton-Kantorovich and distorted Born methods,” *Inverse Problems*, vol. 16, no. 1, pp. L1–L4, Jan. 2000.
- [87] T. Rubæk, P. M. Meaney, P. Meincke, and K. D. Paulsen, “Nonlinear microwave imaging for breast-cancer screening using Gauss–Newton’s method and the CGLS inversion algorithm,” *IEEE Transactions on Antennas and Propagation*, vol. 55, no. 8, pp. 2320–2331, Aug. 2007.
- [88] P. Mojabi and J. LoVetri, “Overview and classification of some regularization techniques for the Gauss-Newton inversion method applied to inverse scattering problems,” *IEEE Transactions on Antennas and Propagation*, vol. 57, no. 9, pp. 2658–2665, 2009.
- [89] M. Ambrosanio, P. Kosmas, and V. Pascazio, “A multithreshold iterative DBIM-based algorithm for the imaging of heterogeneous breast tissues,” *IEEE Transactions on Biomedical Engineering*, vol. 66, no. 2, pp. 509–520, 2019.

- [90] C. W. Manry, S. L. Broschat, and J. B. Schneider, "Higher-order FDTD methods for large problems," *Applied Computational Electromagnetics Society Journal*, vol. 10, no. 2, pp. 17–29, 1995.
- [91] K. Lan, Y. Liu, and W. Lin, "A higher order (2,4) scheme for reducing dispersion in FDTD algorithm," *IEEE Transactions on Electromagnetic Compatibility*, vol. 41, no. 2, pp. 160–165, 1999.
- [92] A. Taflove, S. C. Hagness, and M. Picket-May, "Computational electromagnetics: The finite-difference time-domain method," *The Electrical Engineering Handbook*, vol. 3, 2005.
- [93] O. Ramahi, "Stability of absorbing boundary conditions," *IEEE Transactions on Antennas and Propagation*, vol. 47, no. 4, pp. 593–599, 1999.
- [94] A. Bayliss and E. Turkel, "Radiation boundary conditions for wave-like equations," *Communications on Pure and Applied Mathematics*, vol. 33, no. 6, pp. 707–725, 1980.
- [95] J.-P. Berenger, "A perfectly matched layer for the absorption of electromagnetic waves," *Journal of Computational Physics*, vol. 114, no. 2, pp. 185–200, 1994.
- [96] J.-P. Berenger, "Improved PML for the FDTD solution of wave-structure interaction problems," *IEEE transactions on Antennas and Propagation*, vol. 45, no. 3, pp. 466–473, 1997.
- [97] J. C. Veihl and R. Mittra, "An efficient implementation of Berenger's perfectly matched layer (PML) for finite-difference time-domain mesh truncation," *IEEE Microwave and Guided Wave Letters*, vol. 6, no. 2, p. 94, 1996.

- [98] J. Fang and Z. Wu, “Generalized perfectly matched layer-an extension of Berenger’s perfectly matched layer boundary condition,” *IEEE Microwave and Guided Wave Letters*, vol. 5, no. 12, pp. 451–453, 1995.
- [99] J. A. Roden and S. D. Gedney, “Convolution PML (CPML): An efficient FDTD implementation of the CFS–PML for arbitrary media,” *Microwave and Optical Technology Letters*, vol. 27, no. 5, pp. 334–339, 2000.
- [100] S. D. Gedney, “An anisotropic PML absorbing media for the FDTD simulation of fields in lossy and dispersive media,” *Electromagnetics*, vol. 16, no. 4, pp. 399–415, 1996.
- [101] S. Gedney, “An anisotropic perfectly matched layer-absorbing medium for the truncation of FDTD lattices,” *IEEE Transactions on Antennas and Propagation*, vol. 44, no. 12, pp. 1630–1639, 1996.
- [102] B. D. Gvozdic and D. Z. Djurdjevic, “Performance advantages of CPML over UPML absorbing boundary conditions in FDTD algorithm,” *Journal of Electrical Engineering*, vol. 68, no. 1, p. 47, 2017.
- [103] H. Choi, J.-W. Baek, and K.-Y. Jung, “Comprehensive study on numerical aspects of modified Lorentz model-based dispersive FDTD formulations,” *IEEE Transactions on Antennas and Propagation*, vol. 67, no. 12, pp. 7643–7648, 2019.
- [104] P. Kosmas, C. Rappaport, and E. Bishop, “Modeling with the FDTD method for microwave breast cancer detection,” *IEEE Transactions on Microwave Theory and Techniques*, vol. 52, no. 8, pp. 1890–1897, 2004.
- [105] O. Ramadan, “Stability-improved ADE-FDTD implementation of Drude dispersive models,” *IEEE Antennas and Wireless Propagation Letters*, vol. 17, no. 5, pp. 877–880, 2018.

- [106] F. Costen, J.-P. Berenger, and A. K. Brown, "Comparison of FDTD hard source with FDTD soft source and accuracy assessment in Debye media," *IEEE Transactions on Antennas and Propagation*, vol. 57, no. 7, pp. 2014–2022, 2009.
- [107] G. Pelosi, R. Coccioli, and S. Selleri, *Quick finite elements for electromagnetic waves*. Artech House, 2009.
- [108] K. J. Binns, C. Trowbridge, and P. Lawrenson, *The analytical and numerical solution of electric and magnetic fields*. Wiley, 1992.
- [109] W. C. Chew, *Waves and fields in inhomogenous media*. Wiley-IEEE Press, 1995.
- [110] D. Colton, H. Haddar, and M. Piana, "The linear sampling method in inverse electromagnetic scattering theory," *Inverse problems*, vol. 19, no. 6, S105, 2003.
- [111] I. Catapano, L. Crocco, and T. Isernia, "Linear sampling method: Physical interpretation and guidelines for a successful application," *PIERS Online*, vol. 4, no. 2, pp. 291–295, 2008.
- [112] R. Scapaticci, O. Bucci, I. Catapano, and L. Crocco, "Differential microwave imaging for brain stroke followup," *International Journal of Antennas and Propagation*, vol. 2014, 2014.
- [113] J. D. Shea, P. Kosmas, S. C. Hagness, and B. D. Van Veen, "Three-dimensional microwave imaging of realistic numerical breast phantoms via a multiple-frequency inverse scattering technique," *Medical Physics*, vol. 37, pp. 4210–26, Aug. 2010.
- [114] M. Ambrosanio, P. Kosmasy, and V. Pascazio, "An adaptive multi-threshold iterative shrinkage algorithm for microwave imaging applications," in *2016 10th European Conference on Antennas and Propagation (EuCAP)*, 2016, pp. 1–3.

- [115] M. Ambrosanio and V. Pascazio, “A compressive-sensing-based approach for the detection and characterization of buried objects,” *IEEE Journal of Selected Topics in Applied Earth Observations and Remote Sensing*, vol. 8, no. 7, pp. 3386–3395, 2015.
- [116] Z. Miao, S. Ahsan, P. Kosmas, *et al.*, “Application of the DBIM-TwIST algorithm to experimental microwave imaging data,” in *2017 11th European Conference on Antennas and Propagation (EUCAP)*, IEEE, 2017, pp. 1611–1614.
- [117] P. Lu, J. Córcoles, and P. Kosmas, “Non-linear microwave imaging using fast iterative shrinkage thresholding,” in *2019 Photonics & Electromagnetics Research Symposium-Spring (PIERS-Spring)*, IEEE, 2019, pp. 1949–1956.
- [118] Z. Miao and P. Kosmas, “Multiple-frequency DBIM-TwIST algorithm for microwave breast imaging,” *IEEE Transactions on Antennas and Propagation*, vol. 65, no. 5, pp. 2507–2516, 2017.
- [119] J. M. Bioucas-Dias and M. A. T. Figueiredo, “A new TwIST: Two-step iterative shrinkage/thresholding algorithms for image restoration,” *IEEE Transactions on Image Processing*, vol. 16, no. 12, pp. 2992–3004, Dec. 2007.
- [120] Z. Miao and P. Kosmas, “Microwave breast imaging based on an optimized two-step iterative shrinkage/thresholding method,” in *2015 9th European Conference on Antennas and Propagation (EuCAP)*, Apr. 2015, pp. 1–4.
- [121] J. Shea, P. Kosmas, B. D. Van Veen, and S. Hagness, “Contrast-enhanced microwave imaging of breast tumors: A computational study using 3D realistic numerical phantoms,” *Inverse Problems*, vol. 26, no. 7, p. 074009, 2010.

- [122] A. E. Bulyshev, A. E. Souvorov, S. Y. Semenov, *et al.*, “Three-dimensional microwave tomography. Theory and computer experiments in scalar approximation,” *Inverse Problems*, vol. 16, no. 3, p. 863, 2000.
- [123] Q. Fang, P. M. Meaney, S. D. Geimer, A. V. Streltsov, and K. D. Paulsen, “Microwave image reconstruction from 3-D fields coupled to 2-D parameter estimation,” *IEEE Transactions on Medical Imaging*, vol. 23, no. 4, pp. 475–484, 2004.
- [124] P. Lu, J. Córcoles, and P. Kosmas, “Enhanced FEM-based DBIM approach for two-dimensional microwave imaging,” *IEEE Transactions on Antennas and Propagation*, vol. 69, no. 8, pp. 5187–5192, 2021.
- [125] M. S. Alnæs, J. Blechta, *et al.*, “The FEniCS project version 1.5,” *Archive of Numerical Software*, vol. 3, 2015.
- [126] A. Beck and M. Teboulle, “A fast iterative shrinkage-thresholding algorithm for linear inverse problems,” *SIAM Journal on Imaging Sciences*, vol. 2, no. 1, pp. 183–202, 2009.
- [127] Y. E. Nesterov, “A method for solving the convex programming problem with convergence rate $O(1/k^2)$,” *Doklady Akademii Nauk SSSR*, vol. 269, pp. 543–547, 1983.
- [128] M. Ambrosanio and V. Pascazio, “Compressive sensing for breast microwave imaging,” in *2018 40th Annual International Conference of the IEEE Engineering in Medicine and Biology Society (EMBC)*, IEEE, 2018, pp. 5109–5112.
- [129] W. Chew and J. Lin, “A frequency-hopping approach for microwave imaging of large inhomogeneous bodies,” *IEEE Microwave and Guided Wave Letters*, vol. 5, no. 12, pp. 439–441, 1995.

- [130] R. Scapaticci, P. Kosmas, and L. Crocco, “Wavelet-based regularization for robust microwave imaging in medical applications,” *IEEE Transactions on Biomedical Engineering*, vol. 62, no. 4, pp. 1195–1202, 2014.
- [131] A. H. Golnabi, P. M. Meaney, *et al.*, “Comparison of no-prior and soft-prior regularization in biomedical microwave imaging,” *Journal of Medical Physics*, vol. 36, 2011.
- [132] IEEE Std 1528-2003, “IEEE recommended practice for determining the peak spatial-average specific absorption rate (SAR) in the human head from wireless communications devices: Measurement techniques,” *IEEE Std 1528-2013 (Revision of IEEE Std 1528-2003)*, pp. 1–246, 2013.
- [133] I. G. Zubal, C. R. Harrell, E. O. Smith, Z. Rattner, G. Gindi, and P. B. Hoffer, “Computerized three-dimensional segmented human anatomy,” *Medical Physics*, vol. 21, no. 2, pp. 299–302, 1994.
- [134] S. Ahsan, Z. Guo, *et al.*, “Design and experimental validation of a multiple-frequency microwave tomography system employing the DBIM-TwIST algorithm,” *Sensors*, vol. 18, 2018.
- [135] O. Bucci and T. Isernia, “Electromagnetic inverse scattering: Retrievable information and measurement strategies,” *Radio Science*, vol. 32, 1997.
- [136] W. Guo, S. Ahsan, M. He, M. Koutsoupidou, and P. Kosmas, “Printed monopole antenna designs for a microwave head scanner,” in *2018 18th Mediterranean Microwave Symposium (MMS)*, 2018, pp. 384–386.
- [137] Z. Miao, “Implementation and optimisation of microwave medical imaging based on the multiple-frequency dbim-twist algorithm,” Ph.D. dissertation, King’s College London, 2018.

- [138] K. Belkebir and M. Saillard, “Testing inversion algorithms against experimental data,” *Inverse Problems*, vol. 17, 2001.
- [139] M. J. Burfeindt, T. J. Colgan, R. O. Mays, *et al.*, “MRI-derived 3-D-printed breast phantom for microwave breast imaging validation,” *IEEE Antennas and Wireless Propagation Letters*, vol. 11, pp. 1610–1613, 2012.
- [140] P. Lu, S. Ahsan, and P. Kosmas, “Preliminary study on the feasibility of reconstructing anatomically complex numerical brain phantoms with limited prior information,” in *2020 XXXIIIrd General Assembly and Scientific Symposium of the International Union of Radio Science*, 2020, pp. 1–4.
- [141] I. I. Giannakopoulos, M. S. Litsarev, and A. G. Polimeridis, “Memory footprint reduction for the FFT-based volume integral equation method via tensor decompositions,” *IEEE Transactions on Antennas and Propagation*, vol. 67, no. 12, pp. 7476–7486, 2019.
- [142] A. Fhager, S. K. Padhi, and J. Howard, “3D image reconstruction in microwave tomography using an efficient FDTD model,” *IEEE Antennas and Wireless Propagation Letters*, vol. 8, pp. 1353–1356, 2009.
- [143] D. Ireland and A. Abbosh, “Modeling human head at microwave frequencies using optimized Debye models and FDTD method,” *IEEE Transactions on Antennas and Propagation*, vol. 61, no. 4, pp. 2352–2355, 2013.
- [144] A. Munawar Qureshi, Z. Mustansar, and A. Maqsood, “Analysis of microwave scattering from a realistic human head model for brain stroke detection using electromagnetic impedance tomography,” *Progress In Electromagnetics Research*, vol. 52, pp. 45–56, 2016.

- [145] I. I. Giannakopoulos, M. S. Litsarev, and A. G. Polimeridis, “Memory footprint reduction for the FFT-based volume integral equation method via tensor decompositions,” *IEEE Transactions on Antennas and Propagation*, vol. 67, no. 12, pp. 7476–7486, 2019.
- [146] A. Fedeli, V. Schenone, A. Randazzo, M. Pastorino, T. Henriksson, and S. Semenov, “Nonlinear S-parameters inversion for stroke imaging,” *IEEE Transactions on Microwave Theory and Techniques*, vol. 69, no. 3, pp. 1760–1771, 2020.
- [147] A. Zamani, A. M. Abbosh, and A. T. Mobashsher, “Fast frequency-based multi-static microwave imaging algorithm with application to brain injury detection,” *IEEE Trans. Microw. Theory Tech.*, vol. 64, no. 2, pp. 653–662, 2016.
- [148] A. S. M. Alqadami, A. Zamani, A. Trakic, and A. Abbosh, “Flexible electromagnetic cap for three-dimensional electromagnetic head imaging,” *IEEE Transactions on Biomedical Engineering*, vol. 68, no. 9, pp. 2880–2891, 2021.
- [149] A. Trakic, A. Brankovic, A. Zamani, *et al.*, “Expedited stroke imaging with electromagnetic polar sensitivity encoding,” *IEEE Transactions on Antennas and Propagation*, vol. 68, no. 12, pp. 8072–8081, 2020.
- [150] P.-H. Tournier, M. Bonazzoli, V. Dolean, *et al.*, “Numerical modeling and high-speed parallel computing: New perspectives on tomographic microwave imaging for brain stroke detection and monitoring,” *IEEE Antennas and Propagation Magazine*, vol. 59, no. 5, pp. 98–110, 2017.
- [151] M. Hopfer, R. Planas, A. Hamidipour, T. Henriksson, and S. Semenov, “Electromagnetic tomography for detection, differentiation, and monitoring of brain stroke: A virtual data and human head phantom study,” *IEEE Antennas and Propagation Magazine*, vol. 59, no. 5, pp. 86–97, 2017.

- [152] Acceleware Ltd. “Acceleware FDTD solver.” (2022), [Online]. Available: <https://www.acceleware.com/fdtd-solvers> (visited on 07/14/2022).
- [153] NVIDIA. “CUDA programming guide.” (2021), [Online]. Available: <https://docs.nvidia.com/cuda/cuda-c-programming-guide/index.html> (visited on 07/14/2022).
- [154] J. Chi, F. Liu, E. Weber, Y. Li, and S. Crozier, “GPU-accelerated FDTD modeling of radio-frequency field–tissue interactions in high-field MRI,” *IEEE Transactions on Biomedical Engineering*, vol. 58, no. 6, pp. 1789–1796, 2011.
- [155] B. Archambeault, S. Connor, and J. C. Diepenbrock, “Time domain gating of frequency domain S-parameter data to remove connector end effects for PCB and cable applications,” in *2006 IEEE International Symposium on Electromagnetic Compatibility, 2006. EMC 2006.*, vol. 1, Aug. 2006, pp. 199–202.
- [156] J. A. Tobon Vasquez, R. Scapaticci, G. Turvani, *et al.*, “Design and experimental assessment of a 2D microwave imaging system for brain stroke monitoring,” *International Journal of Antennas and Propagation*, vol. 2019, 2019.
- [157] A. V. Oppenheim, J. R. Buck, and R. W. Schafer, *Discrete-time signal processing*. Vol. 2. Upper Saddle River, NJ: Prentice Hall, 2001.
- [158] J. F. Kaiser, “Nonrecursive digital filter design using the L_0 -sinh window function,” in *Proc. 1974 IEEE International Symposium on Circuits & Systems, San Francisco CA, April, 1974*, pp. 20–23.
- [159] A. K. Jain, M. N. Murty, and P. J. Flynn, “Data clustering: A review,” *ACM Computing Surveys (CSUR)*, vol. 31, no. 3, pp. 264–323, 1999.